博士学位論文

On the study of a reaction-diffusion particle model for clustering of self-propelled oil droplets on a surfactant solution

(界面活性溶液上の自走油滴の集団運動に対する反応拡散-粒子モデルの研究)

キム　ミンス

北海道大学大学院理学院

数学専攻

令和３年９月

On the study of a reaction-diffusion particle model for clustering of self-propelled oil droplets on a surfactant solution

(界面活性溶液上の自走油滴の集団運動に対する反応拡散-粒子モデルの研究)

Minsoo Kim

A thesis presented for the degree of
Doctor of Mathematics

September 2021

Department of Mathematics

Graduate School of Science

Hokkaido University

Acknowledgements

This research was conducted with the help of many people. The supervisor, professor Masaharu Nagayama, has given a great deal of guidance, including policies and evaluation of the research results. We have also been able to advance our research in a great environment with a good supply of equipment. Professor Yasuaki Kobayashi proposed various advice for formal analysis, writing review, and editing through discussion and responded to consultations online and offline. Professor Yikan Liu was a great help in revising for English and presentation online and offline. Our secretaries, Makiko Dewa and Yukari Tomizawa, were given daily student support and helped with events in graduate school activities. Both professor Satoshi Nakata and professor Shinpei Tanaka of Hiroshima University, who are collaborators, provided the experimental data and studied various knowledge with respect to the research theme. Also, Dr. Mamoru Okamoto, Dr. Yusuke Yasugahira, and other laboratory members have discussed the mathematical model and worked on numerical calculations to research the theme. Lastly, I would like to appreciate all those who related research and helped.

On the study of a reaction-diffusion particle model for clustering of self-propelled oil droplets on a surfactant solution

Minsoo Kim

Abstract

We experimentally and numerically investigate collective behaviors of oil droplets floating on a surfactant solution in a narrow circular channel. A closed environment where a glass cover is placed on the channel shows that ethyl salicylate droplets on the surface of sodium dodecyl sulfate solution exhibit transient oscillatory dynamics, leading to the formation of a single cluster via the merging of sub-clusters. When the glass cover is removed, oscillatory behavior resumes, and the cluster breaks up. To understand these experimental findings, we introduce a mathematical model that combines equations of motion for droplets with a reaction-diffusion system, where droplet dynamics and the chemical reactions are considered on the one-dimensional surface, and the diffusion of chemicals in the air phase and the water phase is treated in the two-dimensional region. Our model successfully reproduces transient oscillations and the characteristics of cluster formation, and the effect of the glass cover. We argue that the long-range attractive interaction due to the global concentration profile of the solution suffices for the cluster formation.

Contents

List of Figures

1 Introduction

The study of collective behavior ranges various fields such as biology, zoology, and physics. Although collective behaviors are considered characteristic of complex organisms in living systems, they also exhibit a variety of collective dynamics and autonomous motion in non-living systems. In this section, we introduce research trends and a variety of examples on collective behavior in the living and non-living systems.

1.1 Collective behaviors in the living systems

The collective behavior of a large number of animals is a magnificent phenomenon that occurs in nature, shown in Fig. 1.1. Conspicuous examples of such behavior are flocks of birds, a school of fish swim, [58], a colony of ants [39], and vortex formation in tadpoles [3]. Micro-organisms such as zooplankton [38], bacteria [61], and epithelial cells [40] also exhibits collective behavior.

Functionality is an important factor for the collective behavior in living systems. For example, it has been suggested that multi-cellularity has emerged from the bacteria behaviors, which initiated communication among cells and induced their coordinated motion [44].

In addition, the theoretical research of collective behavior in a living system has been actively studied, such as the flocks of bird model [2], fish schoolings model [1], and colonies of ant model [10]. However, it is difficult to provide practical means for the exploration of collective behaviors because of the complexity of the motions and the difficulty of controlling the behavior of individual organisms. To make up for these difficulties, studies on non-living systems are essential for understanding collective phenomena, since it is much easier for non-living systems to perform controlled experiments.

1.2 Collective behaviors in the non-living systems

The theoretical research on the collective behavior of the non-living system has been actively studied since the proposal of Vicsek's model [57, 42]. Typical examples of the self-propelled system are the experimental system of camphor motion and chemical droplet motion. The mathematical modeling and mathematical analysis thereof are performed. Below, we review the theoretical and experimental researches, which have been conducted, and introduce a recently reported collective motion.

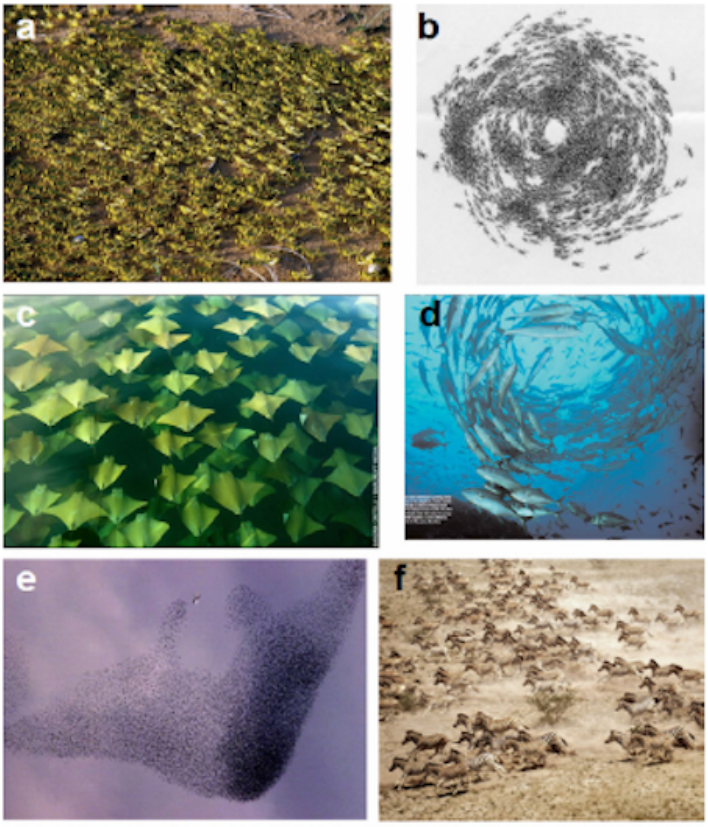

Figure 1.1: A gallery of images related to collective behavior [58]. Among others, it illustrates the possible existence of very general behavioral patterns. (a) Wingless Locusts marching in the field. (b) A rotating colony of army ants. (c) A three-dimensional array of golden rays. (d) Fish are known to produce such vortices. (e) Before roosting, thousands of starlings producing a fascinating aerial display. They are also trying to avoid a predator bird close to the central, finger-like structure. (f) A herd of zebra.

1.2.1 Self-propelled camphor motion

The camphor motion has been experimentally studied to investigate the self-propelled motion involving rotational motion and transition between different dynamical modes [32]. Moreover, analysis of the one-dimensional oscillatory motion [11, 28], and the unidirectional motion on the annual channel [31] was performed by using a mathematical model. In addition, a variety of phenomena under a particular condition such as the deformation and spontaneous separation of camphor scraping [33], the transition of a camphoric acid scraping depending on the pH of aqueous phase [34], and speed of camphor motion induced by water-depth [26] were experimentally investigated. In particular, spontaneous rotation and movement to another chamber of multi camphor scraping under isothermal conditions have been reported [35]. Figure 1.2 shows the rotation and translation of camphor scraping. This switching phenomenon has taken place by the change in the direction of the concentration gradient.

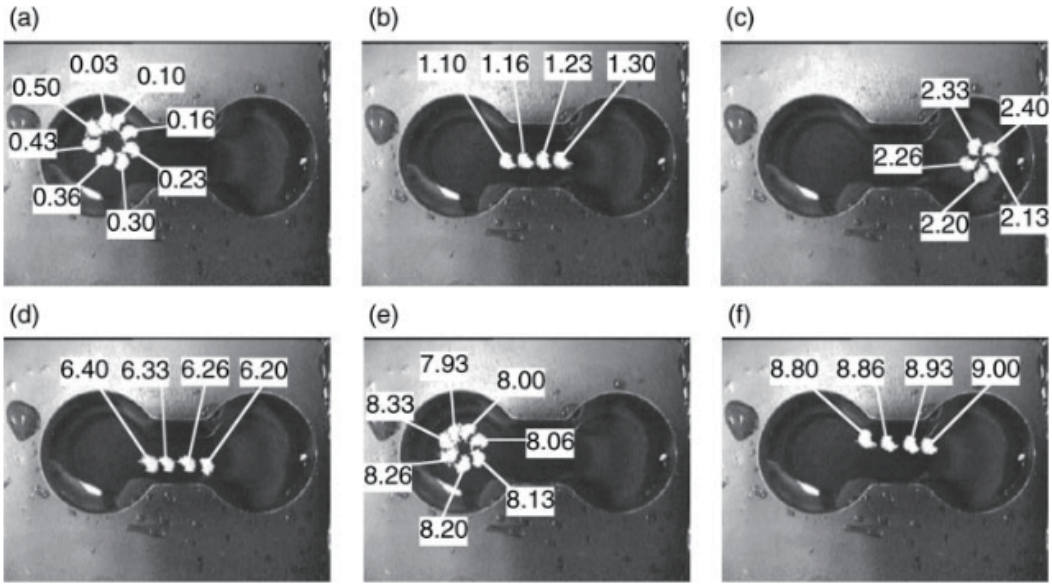

Figure 1.2: Snapshots of the switching motion between the two water phases (top view) [35]. (a) Rotation in chamber L (0-1.0 s), (b) translation from chamber L to R (1.0-1.4 s), (c) rotation in chamber R (1.4-6.0 s), (d) translation from chamber R to L (6.0-6.5 s), (e) rotation in chamber L (6.5-8.7 s) and (f) translation from chamber L to R (8.7-9.1 s). The values are the elapsed time at an interval of 1/15 s.

For example, when self-propelled camphor boats move in a one-dimensional channel, they exhibit various collective behaviors. The research to understand the mechanism of self-propelled motion on the one-dimensional channel was conducted based on the

mathematical model [12]. The synchronized motions of two camphor disks depend on the length of the channel [36, 20], shown in Fig. 1.3, and the collective motion of camphor papers depends on their numbers [14], shown in Fig. 1.4.

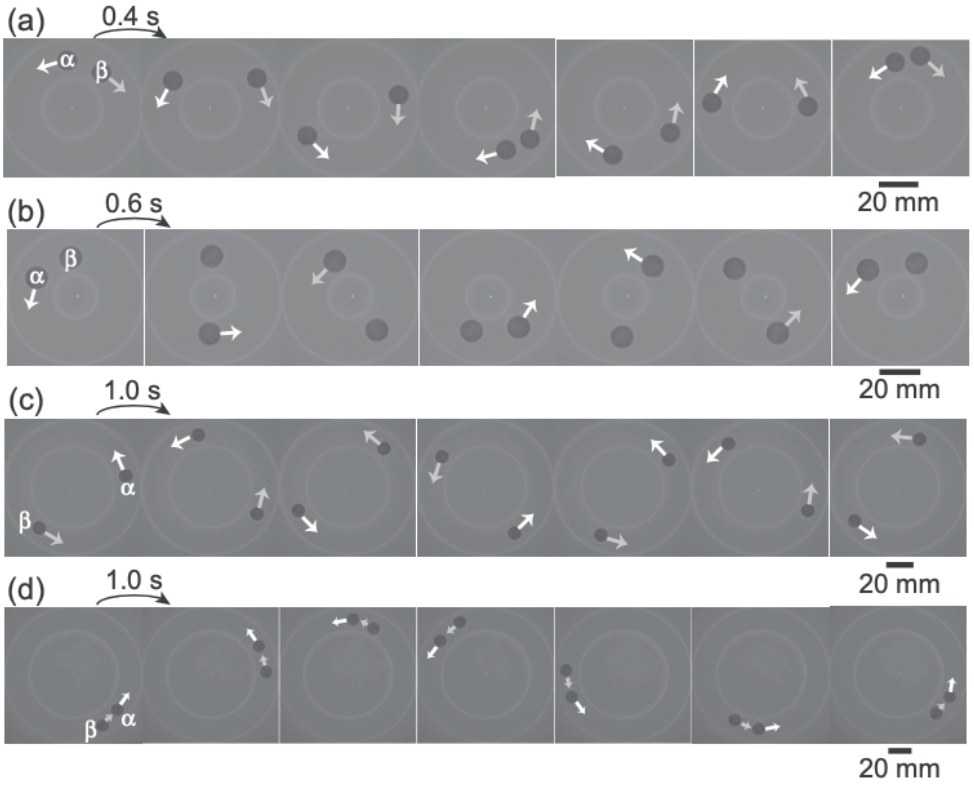

Figure 1.3: Snapshots of experimental results of two camphor disks (α and β) [36]. White and gray arrows denote the directions of motion. Note that, throughout the experiments, the diameters of the camphor disks and the channel width were fixed as 10 and 20 mm, respectively.

Furthermore, the transition was observed on the two-dimensional, indicating that the transition continuously occurs near the boundary of the large area [21, 37]. After sufficient time, it was reported that an initially oscillatory motion could turn into the rotating motion within a small confined area. For millimeter-sized camphor boats and ribbons, the collective motion has taken place if the number of camphor boats exceeds a threshold value [46, 47, 45].

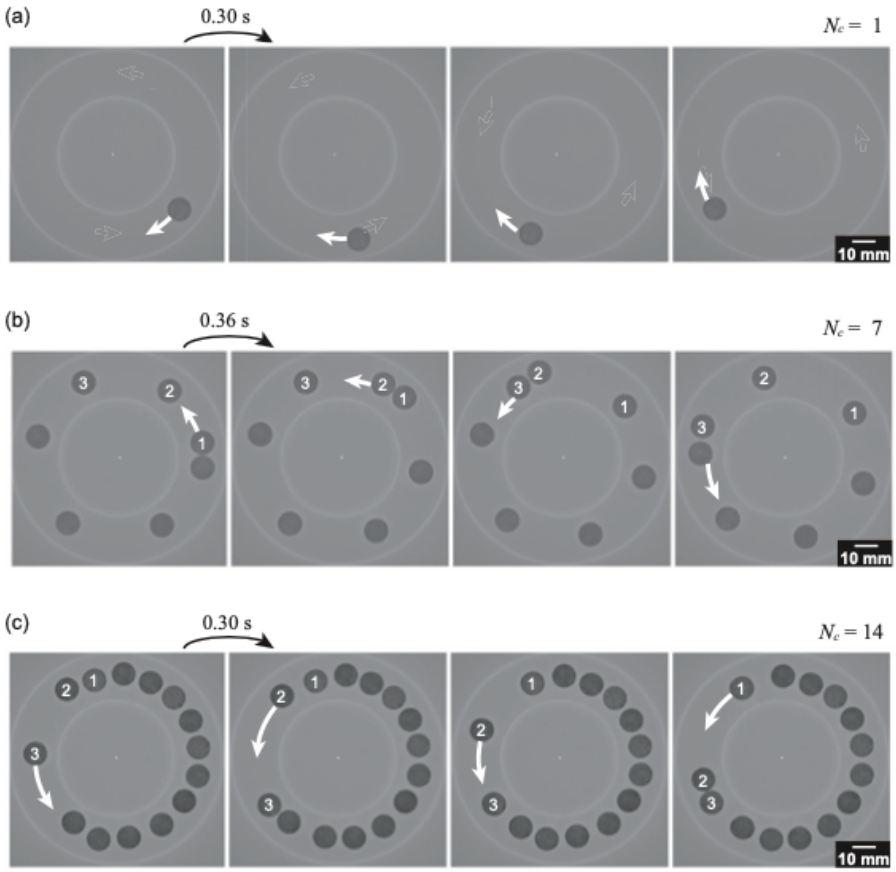

Figure 1.4: Snapshots of the collective motion for Nc = (a) 1, (b) 7, and (c) 14 (top view) [14]. The papers without a white arrow do not move, or hardly move. The number ($i = 1, 2, or 3$) on the camphor paper indicates the different camphor papers.

1.2.2 Self-propelled motion of droplets

As a prime example of self-propelled motion in non-living systems, researches of droplets as a deformable material and solid particles have been actively conducted. There are studies on the self-propelled droplets, which are driven by the gradient of the surface tension of the liquid surface [16, 30]. Furthermore, as another feature on the properties of a chemical substance, it was found that the shape of the droplet spontaneously deform by the gradient of the surface tension [49] or split depending on the volume of the droplet [29]. Besides, researches for a spontaneous motion of droplet according to substances such as Au droplet on the Si and Ge surfaces [9], Janus colloidal particles [17, 27], have been conducted.

In the experiment of pentanol droplet under a condition of specific volume, the tiny droplet has been transformed into crescent shapes and moved spontaneously, shown in Fig. 1.5. On the other hand, when the volume of a droplet is large, the droplet is known to divide into tiny pieces after being deformed. Moreover, the motion of droplets has been observed as irregular motion, shown in Fig. 1.6.

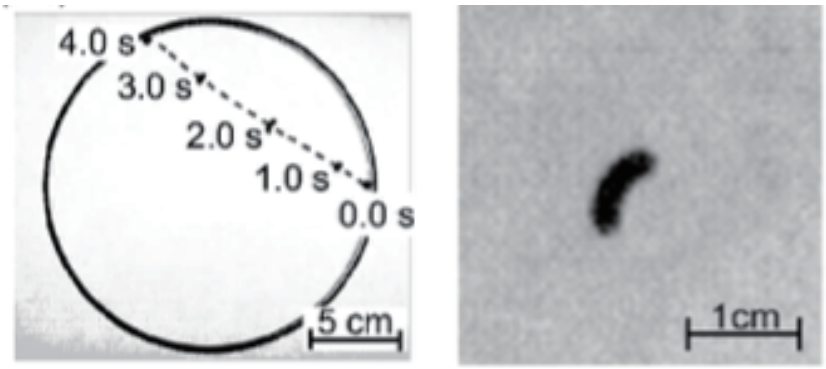

Figure 1.5: When the volume of a droplet is 10μl, it moves in the shape of a crescent to the right [29].

The motion of droplets on a glass substrate has also been reported. For example, a droplet can be driven by the asymmetry of the wetting angle of the droplet due to the chemical gradient of the glass substrate [7] or the asymmetry of the contact angle due to adsorption of surfactant molecules on the glass substrate [25]. Droplets can be driven by cooperative work of surfactant, chemical reaction, and chemical substance leading to surface tension change [54, 41]. From the chemical point of view, we theoretically know that the Marangoni effect occurs due to the surface tension gradient induced by evaporation. This Marangoni effect affects the spontaneous motion of the substances such as miscible liquids [18], liquid marbles [4]. Furthermore, droplets can

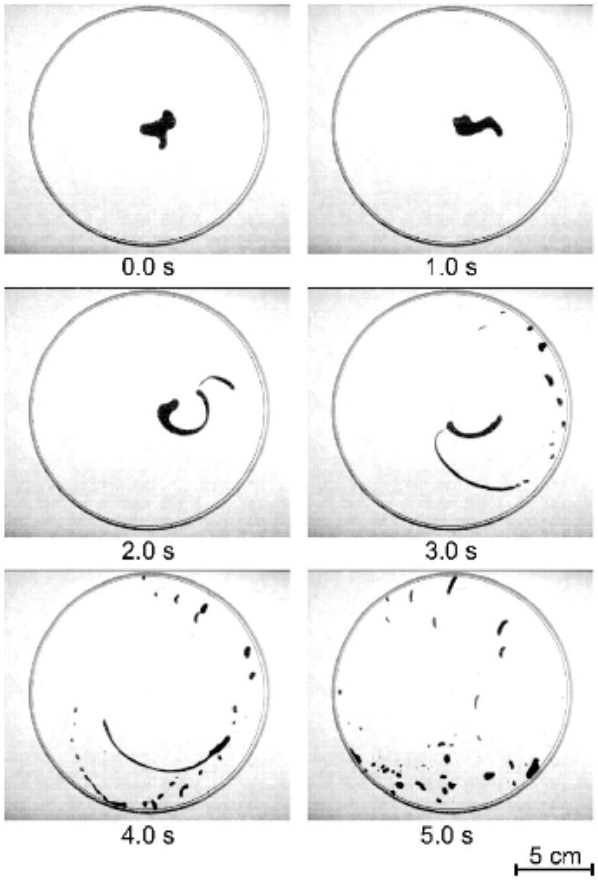

Figure 1.6: When the volume of the droplet is 400μl, the droplet splits and performs irregular motion [29].

be driven because one of the benefits of the non-living system is controlled under certain conditions or external force. To give examples, there are to find the path in the maze in response to the concentration of surfactant solution [24, 5, 62], and to control the motion under electromagnetic field [56, 60].

It has recently been found that butyl salicylate (BS) droplets and ethyl salicylate (ES) droplets on the surface of sodium dodecyl sulfate (SDS) solution, which is known as a surfactant, exhibit a variety of self-propelled motion [50, 43]. The various motion patterns have been observed on the channel when fixed the size of the droplet, which is not divided into small pieces of a droplet. Figure 1.7 shows a variety of patterns of the single ES droplet depending on SDS concentration according to time [50]. Most of the patterns among all patterns form the circular pattern.

The experiments of the single droplet have been studied on the rectangle water tank, which is a simpler geometry to investigate mechanism for the various motion

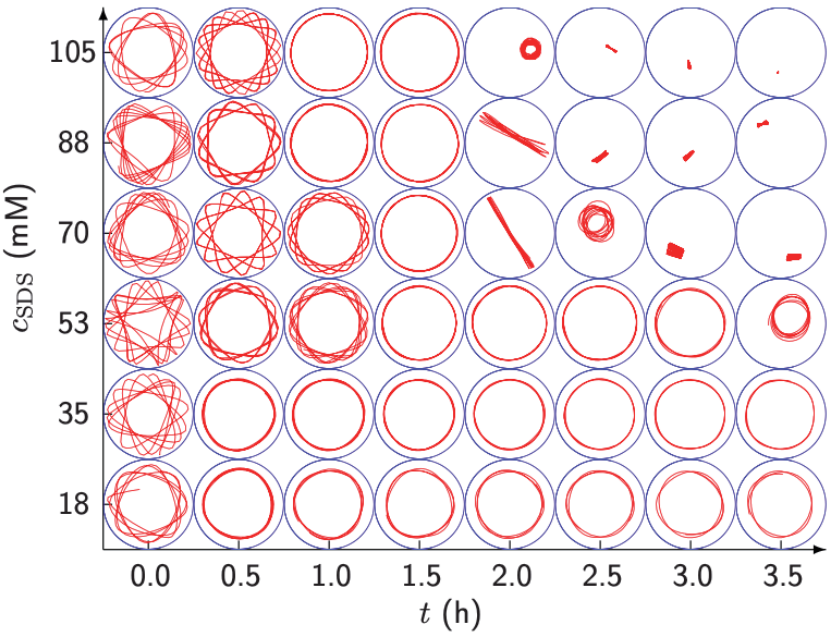

Figure 1.7: Trajectory-pattern transitions with different SDS concentration [50]. Six samples produced different histories. Blue circles represent the dish wall.

[43]. We have known that the dissolution of oil in the surfactant solution causes the Marangoni effect (known as unbalanced surface tension), which causes the droplet to move.

When the velocity of the droplet reached almost zero, shown 3 in Fig. 1.8, it turned to reverse and rapidly moved to the surfactant solution surface in the opposite direction, increasing acceleration, shown as 4-6 in Fig. 1.8. The droplet motion has been recorded by changing the concentration of the SDS surfactant solution according to time as the concentration of the SDS surfactant solution decreases with the adsorption reaction of the ES molecules and the SDS molecules. From these experiment results, three droplet motions changed due to initial SDS concentration have been observed: the droplet motion hardly moves when the concentration of SDS is low, that is, the stationary state, shown in Fig. 1.9; a small oscillatory state was observed, shown in Fig. 1.10; the droplet reached both ends of the water tank and reversed when the concentration is raised to more high, shown in Fig. 1.11.

1.2.3 Collective motion of multiple droplets

Since droplets can split and fuse as shown in the experiment of a pentanol droplet system [29], the collective motion of droplets, experimentally and theoretically, have

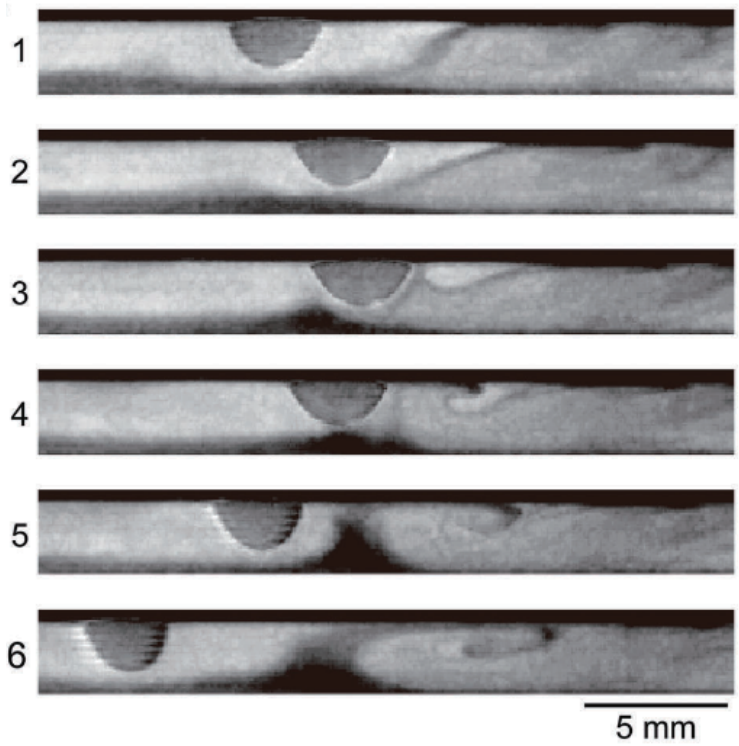

Figure 1.8: Snapshots of droplet's motion together with convection on a SDS surfactant solution according to time [43].

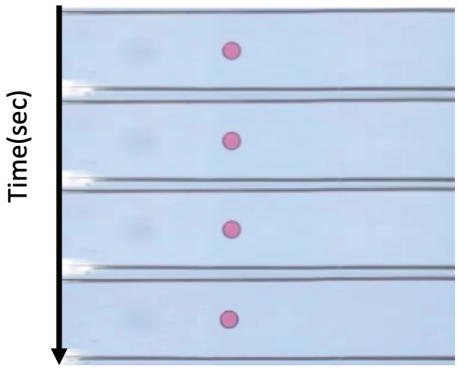

Figure 1.9: A stationary state of the single droplet under 5mM SDS concentration [43].

only recently been reported [6, 15]. Figure 1.12 shows that the droplets started to attract each other after several minutes and eventually formed a single cluster. A single cluster forms a different shape depending on the volume of droplets.

Recently, various kinds of clustering of ES droplets have also been reported, depending on the concentration of surfactant solution [51]. In particular, we have found that under closed cover conditions, the oscillatory motion of droplets stops, and over

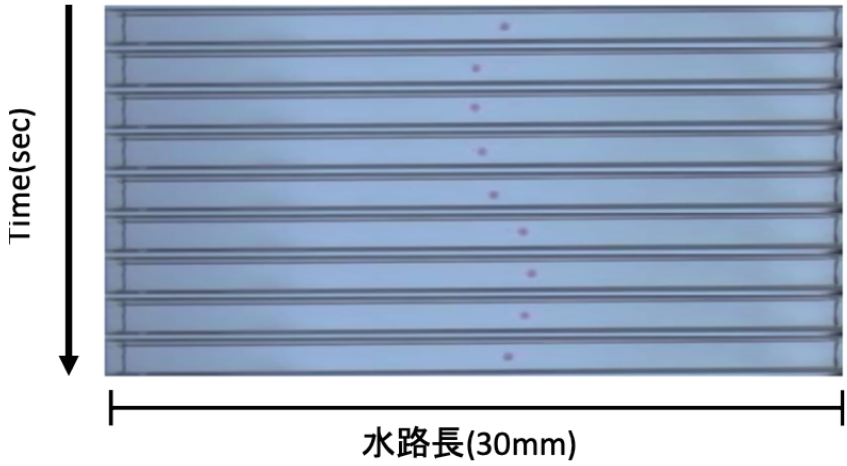

Figure 1.10: An oscillatory state of the single droplet under 20mM SDS concentration [43].

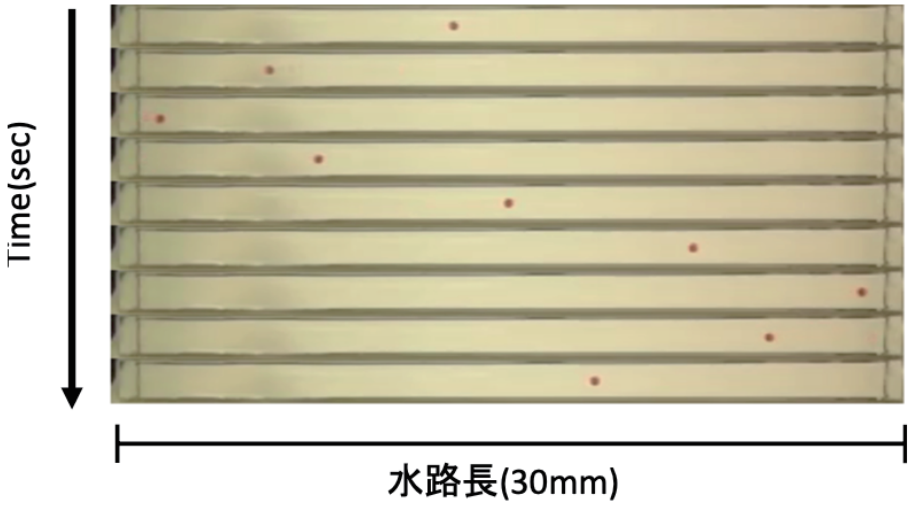

Figure 1.11: A reciprocating state of the single droplet under 60mM SDS concentration [43].

time, the droplets form a cluster and then remain a stationary state. On the other hand, when the cover was removed, the droplets that remained stationary recovered their activity. Furthermore, droplets form a chain structure and a ring structure on the two-dimensional surface, dynamically changing its structure, shown in Fig. 1.13.

The mechanism for the formation of such structures has yet to be precisely explained. In Fig. 1.7 and Fig. 1.13, depending on the concentration of sodium dodecyl sulfate (SDS) surfactant solution, it was observed that the ring structure, one of the kinetic properties of ethyl salicylate (ES) droplets in SDS surfactant solution, was temporarily formed. In addition, the part of the difficulty for understanding the mech-

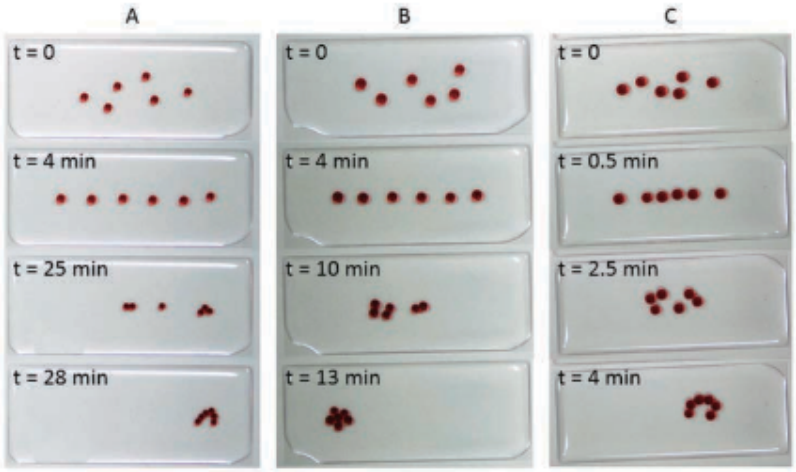

Figure 1.12: Motion of six decanol droplets [6]. The volume of individual droplets is (A) 1μL, (B) 2μL and (C) 5μL. The size of the glass substrate is 24×60 mm. Volume of aqueous decanoate solution is 2 mL.

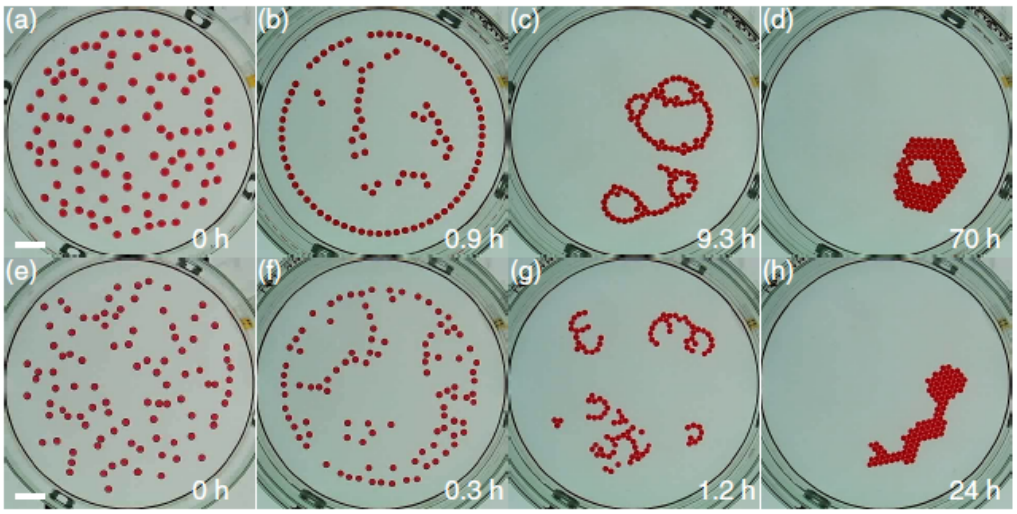

Figure 1.13: Typical structures seen in two samples [51]. (a)−(d) Sample A. cES 70% and cSDS 55mM. (e)−(h) Sample B. cES 90% and cSDS 42mM.The elapsed time is included in the images. (a) and (e) Random, intermittent motion (stage I). (b) and (f) Ring along the wall with some clusters inside (stage II). (c) and (g) Cluster oscillation with characteristic wiggling motion (stage III). (d) and (h) Final static crystal (stage IV).

anism lies in a large variety of states the cluster can take in a two-dimensional surface system. Therefore, to understand the mechanism, it is desirable to set up a simpler geometry such as a narrow channel that enables us to study selected modes of clus-

tering motion. As various causes of this collective phenomenon, interactions between particles bound to the surface have been theoretically explained as lateral capillary force, denoted as the Cheerios effect [22, 23, 13]. On the other hand, the interaction between two droplets, which is the adjoining droplets depending on surface tension gradient induced by the evaporation, has been reported [8]. The interaction between droplets explained by the evaporation leads to surface tension gradients, yielding the formation of the ring structure [59].

1.3 The purpose of this research

Many theoretical studies on such droplet motion have been reported, such as an analysis of a droplet model that moves by coupling with a chemical reaction on a wet substrate [53], the regularly oscillatory motion considering contact angle [48] surface tension change of the air-water interface [30], and convection generated by a chemical reaction that occurs on the water surface [55] or inside the droplet [19]. This research aims to understand the mechanism for the three types of motions for a single droplet and clustering dynamics for multiple droplets through various simulations taking advantage of the mathematical model based on reaction-diffusion equations and several functions of various meanings. In order to build the mathematical model, there are several points to be thoroughly taken into account; the chemical processes such as evaporation, a condensation, and a formation of chemical substance; the effect of the cover [51], and the water phase depending on the water-depth of surfactant solution [26].

Chapter 2 introduces experiments an oscillatory motion of droplet. We present experimental results of an ES droplet system in the quasi-one-dimensional circular water channel. It turns out that the system exhibits transient oscillatory behavior, as well as one-dimensional clustering behavior. It is also shown that the existence of the cover over the chamber changes droplet dynamics. In addition, we suggest several assumptions necessary to construct a mathematical model.

Chapter 3 provides a two-dimensional mathematical model that enables us to study the mechanism of clustering behavior, which is an extension of our previous model [43]. Furthermore, we take into account the chemical concentration, such as the evaporation and the condensation in the air, so that the effect of the cover is studied. Also, we introduce a simplified interaction function between droplets, which is derived by approximating the interaction due to the lateral capillary effect [13]. In addition, we demonstrate a variety of simulation results, such as the reproduction of the motions and clustering dynamics. Besides, we investigate the mechanism of oscillatory motion

and clustering dynamics through simulations.

Chapter 4 describes deriving a one-dimensional mathematical model, an extension of our previous model [52], from a two-dimensional mathematical model, under the condition that the region of the chemical system is thin enough. Likewise, we show that a one-dimensional mathematical model can also qualitatively reproduce the clustering process of droplets, as well as the motions of a single droplet. Moreover, we suggest that the global concentration profile of the surfactant solution suffices for the cluster formation and that attractive forces due to the lateral capillary effect are not necessary to account for the observed phenomena.

Chapter 5 summarizes the simulation results of a two-dimensional and a one-dimensional mathematical model, discusses its limitations, and suggests some areas for further research.

2 Experiments

Prof. Tanaka, Prof. Sogabe, and Prof. Nakata have reported the spontaneous motion of ethyl salicylate (ES) droplets floating on the sodium dodecyl sulfate (SDS) surfactant solution [50, 51]. Both the oscillatory and the clustering motion have been observed through experiments. The effect of the cove, also, has been confirmed experimentally. We introduce our experiment setting and results for the 20 droplets and the chemical mechanism for the oscillatory motion of the droplet.

2.1 Experimental setup and procedure

Both ethyl salicylate (ES) and sodium dodecyl sulfate (SDS, ion-pair chromatography grade) were purchased from Tokyo Chemical Industry Co., Ltd. (Tokyo, Japan), and paraffin liquid was purchased from Sigma-Aldrich Japan (Tokyo, Japan). The droplets were dyed with Oil Red O, purchased from Nacalai Tesque, Inc. (Kyoto, Japan), for visualization. The pure water (18.2 MΩ·cm) used for the surfactant solution was produced with a Milli-Q water purification system (Millipore). The composition of a droplet was fixed at 80 wt% ES, 20 wt% paraffin, and 0.005 wt% Oil red O. The volume of a droplet was 10 μl. The number, N, of droplets in a system was $N = 1$ or $N = 20$ in this study. The channel was made with two glass dishes combined concentrically. The outer dish was 90 mm in inner diameter, and the inner dish was 70 mm in outer diameter so that the width of the channel between them was 10 mm. The channel was filled with 15 ml of SDS solution. The depth of the solution was about 9 mm. The concentration of SDS solutions was fixed at 35 mM. After the droplets were gently placed on the surface of the SDS solution, the channel was covered by a glass cover. No tight sealing was applied. The motion of droplets was captured using a high-speed CMOS camera (Baumer VCXU-04C, Frauenfeld, Switzerland) as 512×512 time-stamped images. The frame rate was 10 Hz. The position of droplets was detected using a color filter and the watershed segmentation algorithm in the OpenCV library. Both the camera and the dishes were placed in a box whose inner temperature was controlled by a heater at 25.0 ± 0.5°C. The room temperature was controlled at about 24°C by air conditioners. The elapsed time t of an experiment was measured from the moment when all the droplets were placed on the surface, and the dishes were covered by a glass cover. A sample was observed firstly until all the droplets stopped entirely for about 12–15 hours. Then, the glass cover was removed, and the effect of fresh air was observed for another 5 hours.

2.2 Experimental results

2.2.1 The single droplet

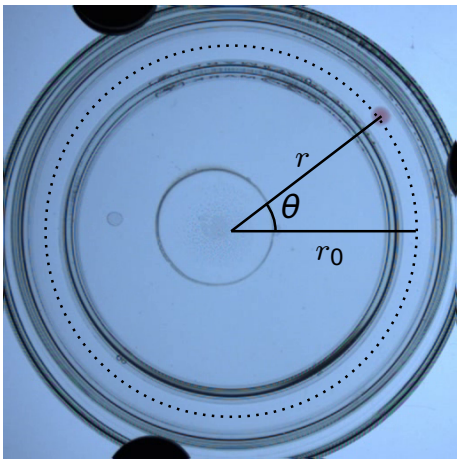

Figure 2.1: Snapshot of the circular channel made by two concentric dishes (top view). A single droplet with the polar coordinates (r, θ) is placed inside the channel. The dotted circle with radius $r_0 = 40$ mm goes through the center of the channel. The round object inside the inner dish is a lump of glue.

Figure 2.1 shows the experimental system and the coordinate to express the position of a droplet. We observed that, through the entire experiment, droplets permanently moved through the center of the channel with $|r - r_0| \lesssim 1$ mm (see Fig. 2.1), except when they moved vigorously in the initial stage of experiments. Therefore, we used only the angular position θ to specify the droplet position.

Figure 2.2 shows a typical observation of the angular position θ of a single droplet as a function of t. Figures 2.2(b)–(d) are enlarged views of those in Fig. 2.2(a). Note the unit of t in each plot. When $t \simeq 1 \sim 6$ h, the droplet exhibited back-and-forth oscillations as shown in Fig.2.2(b)-(c). The oscillation amplitude decreased gradually when $t \gtrsim 6$ h [Fig. 2.2(d)]. Even after the oscillation amplitude was diminished, the droplet kept moving slowly until it stopped completely at $t \simeq 13$ h.

The decrease of the oscillation amplitude $\Delta\theta$ is shown in Fig. 2.2(e), where $\Delta\theta$ at time t is defined by the maximum angular variation in $[t, t + s]$ with $s = 120$ seconds.

2.2.2 The multiple droplets

Through these experiments, we noticed the effect of the existence of the cover of the channel on the motion. The droplets were static clusters, at that time, we removed the

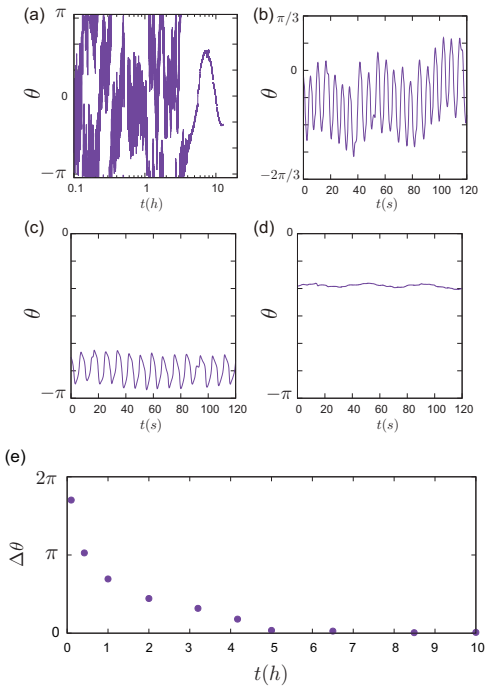

Figure 2.2: Time profile of the angular position θ of a single droplet. (a) The entire profile until the droplet stops. (b)–(d) enlarged views of (a) for 120 seconds starting from (b) $t = 1$ h, (c) $t = 3.6$ h, and (d) $t = 5$ h. (e) Time profile of the oscillation amplitude.

cover, and after sufficient time, we found that the droplets were continuously moved according to time, and each of the droplets was individually separated. When closed the cover, the droplets were formed some clusters according to time and finally kept static state as clusters after sufficient time.

Figure 2.3 shows typical modes of motion when multiple droplets coexist in the channel. At first, each droplet moved in a random direction until it collides with another droplet [see Fig. 2.3(a)]. They changed the direction of motion after the collision. Thus, they showed back-and-forth oscillations between two neighboring droplets. They did not overtake other droplets except at the beginning of the experiment when they were the most active; The motion of droplets quickly subsided. Within an hour, the droplets started forming clusters while continuing oscillatory motion between the two neighboring droplets [Fig. 2.3(b)]. At about $t = 2$ h, oscillatory motion disappeared and the droplets formed several clusters [Fig. 2.3(c)]. Finally, a single cluster was formed [Fig. 2.3(d)]. The entire process took 10–12 hours.

Figure 2.4(a) plots the angular position θ of the droplets as functions of t, whose enlarged views are shown in Fig. 2.4(b)–(d). Vigorous motions of the droplets in

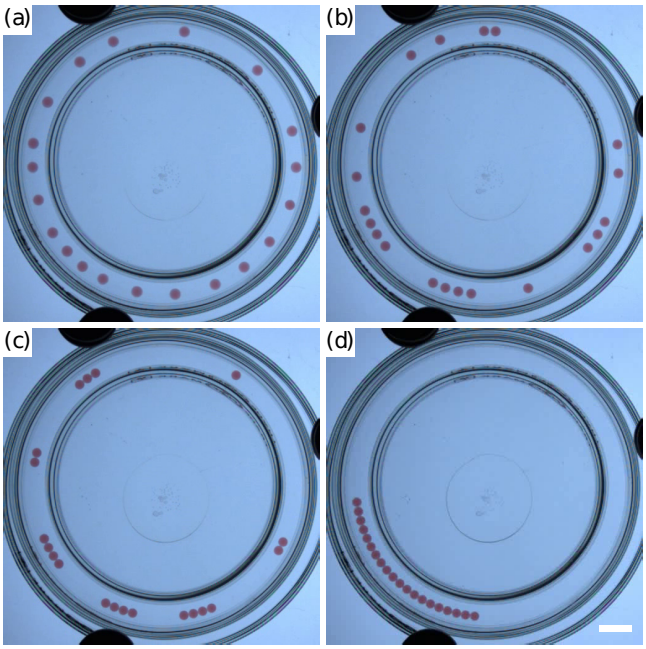

Figure 2.3: Dynamics of 20 droplets in the channel (top view), taken at (a) $t = 0.2$ h, (b) $t = 0.6$ h, (c) $t = 2.0$ h, and (d) $t = 8.0$ h. The scale bar in (d) is 10mm.

$t \lesssim 0.5$ h are shown in Fig. 2.4(b), which subsided within an hour and the trajectories started converging to several bundles [Fig. 2.4(c)]. Whereas the droplets still showed oscillations at $t = 0.6$ h [Fig. 2.4(c)], the oscillations stopped at $t = 2.0$ h [Fig. 2.4(d)]. The trajectories eventually converged to a single bundle, as seen in Fig. 2.4(a) at $t \sim 10$ h. This corresponds to a single cluster of the droplets, as shown in Fig. 2.3(d).

We also noticed the effect of the cover through these experiments, shown in Fig. 2.5. It seemed that the saturation level in the vapor phase affected the motion of droplets significantly. Even after droplets stopped moving, as shown in Fig. 2.3(d), they recovered activity and restarted to move when the glass cover is removed. Figure 2.6 shows the behavior after removing the cover. At first, the cluster broke into several small clusters. As time elapsed, clusters kept breaking and eventually came apart into droplets. In an experiment shown in Fig. 2.6, the droplets tended to move clockwise while oscillating back-and-forth, possibly because of some air flows.

2.3 The chemical mechanism of the oscillatory motion

We have discussed the mechanism for how the droplet oscillate [43]. Briefly, in a balanced state in Fig. 2.7(a), the lateral force was described as interfacial tensions,

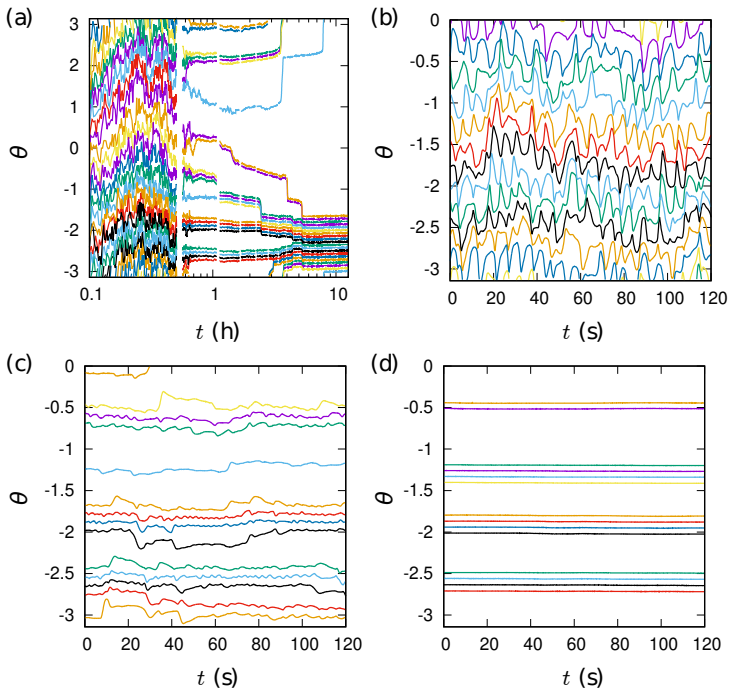

Figure 2.4: Time profiles of the angular positions θ of 20 droplets. (a) The changes in θ measured until the droplets stopped. (b)–(d) The changes in θ for 120 s starting at (b) $t = 0.2$ h, (c) $t = 0.6$ h, and (d) $t = 2.0$ h in (a). In (b)–(d), only the trajectories in $-\pi < \theta < 0$ are plotted. Note that some data points are missing in (a), shown as white vertical strips, because the particle tracking is interrupted roughly every 30 min due to the data transfer.

on the other hand, the vertical force was described as buoyant and gravity forces of the droplet. Furthermore, if the density of ES concentration was higher than the concentration of SDS aqueous solution, the droplet was hung on the surface.

We assume that the adsorption density for the left side was slightly higher than the right side for an explanation of movement. Such a slight difference induce the different contact angle. In structure, there are three kinds of surface tension as air/water, air/solid, solid/water interface, respectively. Therefore, it is possible to assume that surface tension of solid/water interface ignores because it was sufficiently small compared to the surface tension of air/water interface, as shown in Fig. 2.7(c).

With the increased concentration of SDS aqueous solution, the angle was increased, that is, the droplet shape changed to be rounded. Nevertheless, them, the other side was relatively not round under difference density. Also, with increasing concentration of SDS aqueous solution, all of them were decreased. Therefore, the ES droplet accelerated

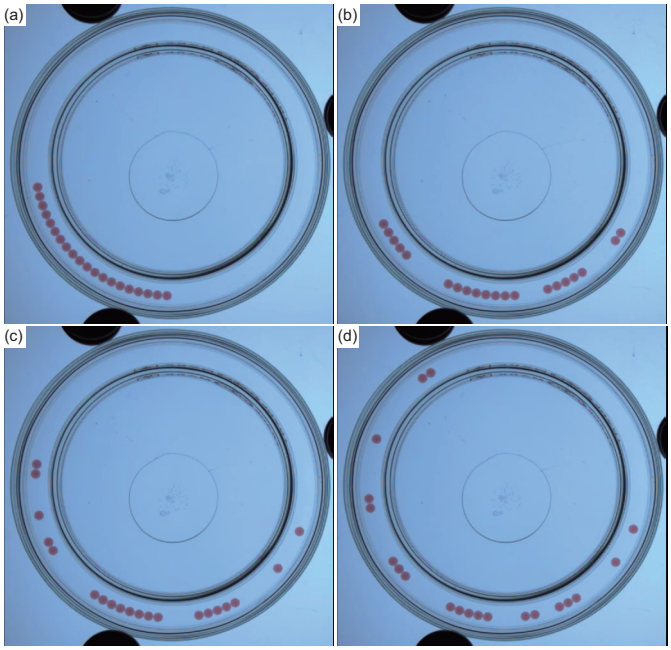

Figure 2.5: Dynamics of 20 droplets without a cover in a channel taken.

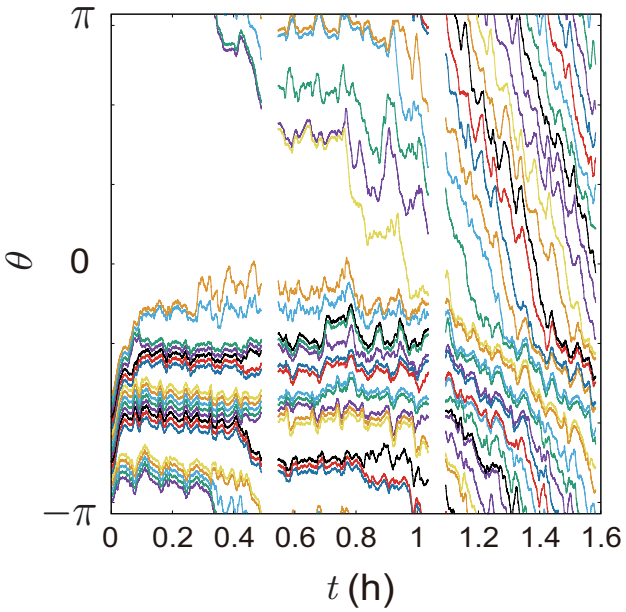

Figure 2.6: Time profiles of the angular positions θ for 20 droplets after the removal of the glass cover. A single stationary cluster under the closed cover condition is chosen as the initial state.

in the direction to the right. Similarly, oscillation occurred, as shown in Fig. 2.7(b).

Experimental result in Fig. 2.7(c), shows that γ_{ow} is negligible compared to γ_{aw}.

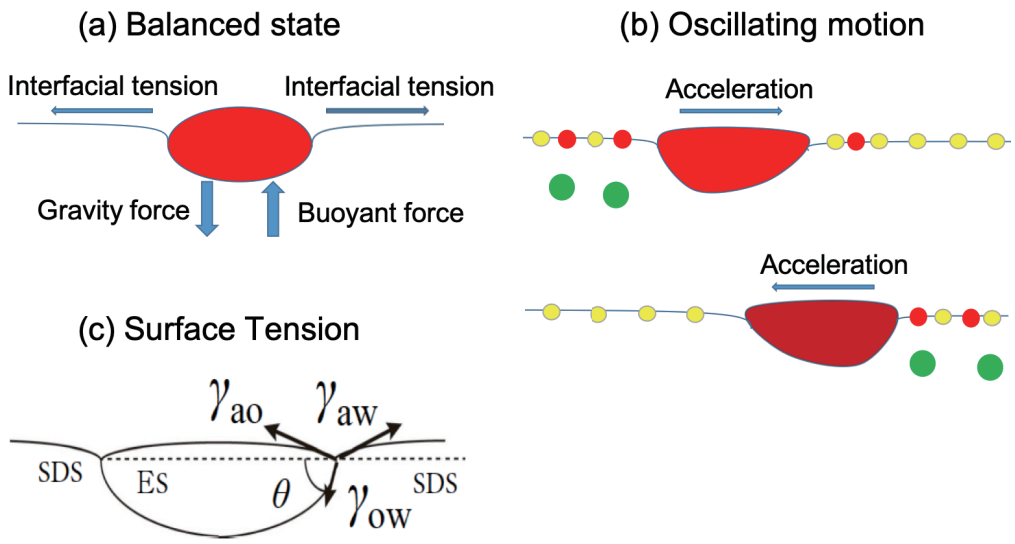

Figure 2.7: Illustration of the principle of the ES droplet motion. (a) the lateral force is described as interfacial tensions, on the other hand, vertical force is described buoyant and gravity forces of droplet, (b) the principle of generating oscillation, (c) angle of surface tension.

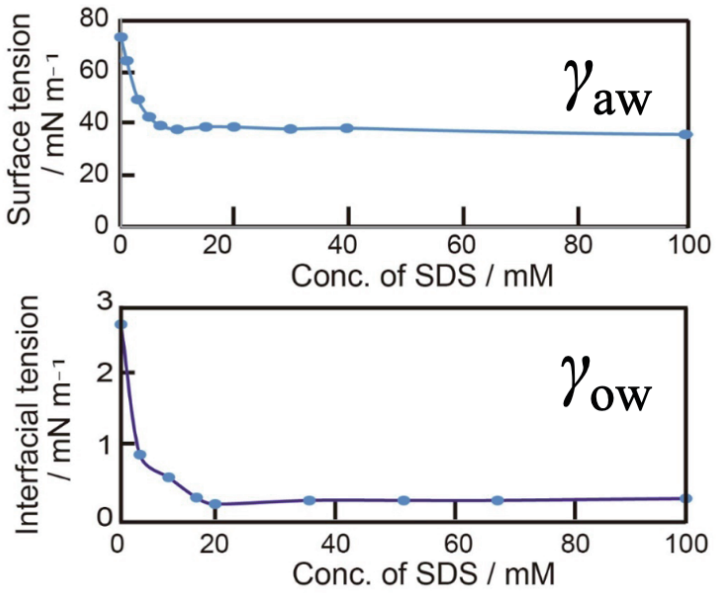

Figure 2.8: The change in each surface tension for SDS concentrations [43]

3 A two-dimensional mathematical model

The experimental results are summarized as follows: a single ES droplet exhibits transient oscillatory motion, leading to an inactive state, and multiple ES droplets, initially showing oscillations, start to form small sub-clusters, which then merge into a single cluster. We have also observed that the behavior of the droplets is affected by the presence/absence of the glass cover. The effect of the cover leads us to think that the SDS concentration in the vapor phase is an essential factor to account for the observed droplet motion. Below we construct a mathematical model that enables us to understand the spontaneous motion and the other observed features theoretically.

3.1 The model assumptions

We consider a two-dimensional system with the one-dimensional channel, depicted in Fig. 3.1.

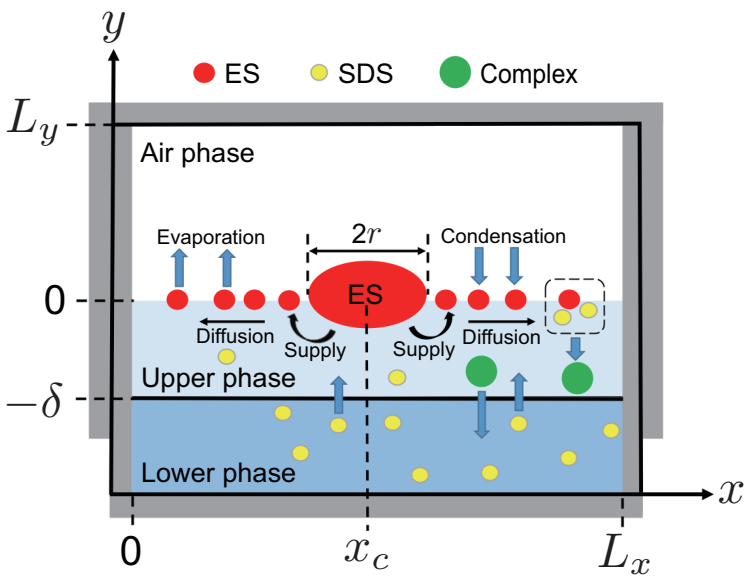

Figure 3.1: Illustration of the model. The system consists of the two-dimensional air region and bulk water (SDS solution) region, and the one-dimensional air/water interface. A droplet lies on the air/water interface at $x = x_c$. ES molecules supplied by the droplet react with SDS to form SDS-ES complexes at the air/water interface ($y = 0$). The water region is divided into the upper and the lower phase at $y = -\delta$; the lower phase is sufficiently deep that chemical concentrations are taken to be constant. Although the droplet is depicted here as an object with nonzero thickness, in the mathematical model it is a one-dimensional object with zero thickness.

Although the droplet is depicted as an object with nonzero thickness, it is a one-dimensional object with zero thickness in the mathematical model. This system consists of the water region, the air region, and the air/water interface region. The concentrations affected by the chemical reactions are separately considered in each region. As an initial state, the water is filled by the SDS molecules as a surfactant, and the surface of the water is covered by the ES molecules emitted from a droplet as an oil. Both of which decrease the surface tension, that is, SDS can alone decrease surface tension, but it can be further reduced by ES coexistence. When a droplet moves, the surface tension in front of the droplet is higher than behind because the droplet leaves molecules behind that effect surface tension. The oscillatory motion occurs when the molecules that remain behind the droplets form the SDS-ES complex and the surface tension in the region increases. The reaction, which forms the SDS-ES complex, diminishes SDS, ES molecules at the surface, and thus the surface tension of that region increases until SDS molecules supply from the bottom of the water. We theoretically know that the chemical concentrations on the air/water interface change the surface tension, and the surface tension influences the droplet dynamics. Hence, we take as variables the position of ES droplets and the concentration of SDS, ES, and SDS-ES complex. To formulate a mathematical model of these processes, we set the following assumptions:

1. The air region and the bulk water region are two-dimensional, and the air/water interface is one-dimensional. The bulk water region is further divided into the upper and lower phase, where the lower phase is sufficiently large that the chemical concentration is constant there; hence the lower phase serves as a reservoir for the upper phase.

2. ES molecules are adsorbed on the air-water interface but are difficult to dissolve into the water phase because of their low solubility. On the other hand, both SDS molecules and SDS-ES complex is dissolved into the water phase. Also, ES molecules are exchanged between the air phase and the air/water interface by evaporation and condensation.

3. The formation of SDS-ES complexes occurs on the air/water interface, which is saturated when the concentration of SDS-ES complexes becomes sufficiently high. The complex formation is an increasing function of both SDS and ES concentrations. Because SDS molecules are abundant relative to ES molecules, the production linearly depends on the ES concentration, whereas the dependence on the SDS concentration has a sigmoidal shape.

4. The surface tension is decreased with an increase in the concentration of ES or SDS. The concentration of the ES-SDS complex does not affect the surface tension: It has been suggested in [50] that ES and SDS form a complex to dissolve into the water so that it no longer affects the air/water interface.

5. The shape of the ES droplets does not change either by motion or by supplying ES molecules onto the air/water interface.

6. Droplets directly interact with each other only by the excluded volume effect; Lateral capillary force is neglected.

3.2 Derivation of the model

Based on the assumptions in Section 3.1, we theoretically develop the two-dimensional model to reflect both the air phase and the depth of water. We introduce a mathematical model of the self-propelled motion and the interaction between droplets when there is more than one droplet.

3.2.1 The model equations of governing system

In this thesis, we study the clustering dynamics for multiple droplets. From a physical point of view, there are various interactions between droplets, especially capillary forces and excluded volume effect are widely known as attractive and repulsive, respectively. Recently, the lateral capillary force and excluded volume effect have been extensively studied. [22, 23, 13]. The origin of the lateral capillary force is the overlap of perturbations formed around such particles on the surface. The mechanism is that because of the deformation of the meniscus caused by the decrease of the potential energy of the two particles when they approach each other, two particles on the surface attract. In contrast, the excluded volume effect occurs when the distance between the centers of the two identical particles is smaller than the sum of their radius because the centers of two identical particles cannot be placed closer to each other than a distance twice as great as their radius. Under multiple droplets condition, the viscous drag force $2\eta r dx_c^i/dt$ equals the net force from the surface tension difference at the ends of both and the adjacent particles. Note that the expression of the viscous drag force is an approximation: here, we have chosen the simplest possible form.

From assumption 1, we define the air/water interface as the region $(0, L_x)$ at $y = 0$, the upper phase of water as $(0, L_x) \times (-\delta, 0)$, and the air phase as $(0, L_x) \times (0, L_y)$;

and we treat the lower phase as a boundary condition of the upper phase at $y = -\delta$.

$$
\begin{cases}
\dfrac{dx_c^i}{dt} = \dfrac{1}{\eta}\left[\gamma\big(u(t,x_c^i+r), s(t,x_c^i+r,0)\big) - \gamma\big(u(t,x_c^i-r), s(t,x_c^i-r,0)\big)\right], \\
\qquad\quad + \dfrac{1}{2\eta r}\left[F_0(x_c^i, x_c^{i-1}) - F_0(x_c^i, x_c^{i+1})\right], \quad t>0, \\
\dfrac{\partial u}{\partial t} = d_u \dfrac{\partial^2 u}{\partial x^2} + \displaystyle\sum_{i=1}^{N} \chi_i^+(x) k_0 \left(1 - \frac{u(t,x)}{u_0}\right) + k_a w(t,x,0)\left(1 - \frac{u(t,x)}{u_0}\right) \\
\qquad\quad - \displaystyle\sum_{i=1}^{N} \chi_i^-(x) k_u \left(1 - \frac{w(t,x,0)}{w_0}\right) u(t,x) \\
\qquad\quad - k_{us}\left(1 - \dfrac{c(t,x,0)}{c_0}\right) f(s(t,x,0))u(t,x), \quad t>0,\ x\in(0,L_x) \\
\dfrac{\partial s}{\partial t} = d_s \Delta s, \quad t>0,\ (x,y)\in(0,L_x)\times(-\delta,0), \\
\dfrac{\partial c}{\partial t} = d_c \Delta c, \quad t>0,\ (x,y)\in(0,L_x)\times(-\delta,0), \\
\dfrac{\partial w}{\partial t} = d_w \Delta w, \quad t>0,\ (x,y)\in(0,L_x)\times(0,L_y).
\end{cases}
\tag{3.1}
$$

Assumption 1 implies that all relevant chemical processes, such as supply and adsorption of ES, and complex formation of ES and SDS, occur in the upper phase. By taking the limit $\delta \to 0$, we have a two-layer system with the air/water interface and the lower phase (bulk water). We have confirmed numerically that the change of δ values does not qualitatively change the droplet behavior. From assumption, the concentration of ES is considered both in the air phase and the air/water interface, each denoted by $w(t,x,y)$ and $u(t,x)$, respectively; and the concentration of SDS and ES-SDS complexes are considered in the upper phase of water, denoted by $s(t,x,y)$ and $c(t,x,y)$, respectively. From assumption, the i-th droplet is specified by its position of the central point x_c^i $(i = 1,\dots,N)$ with a fixed radius r. We initially place N droplets on the air/water interface in such a way that the i-th droplet is always on the left side of $i+1$-th droplet. By taking into account assumptions 3, 4, and 6, we describe dynamics of these variables in Eq. (3.1).

The first equation describes the motion of the i-th droplet. The first bracket represents the surface tension difference, and the second bracket represents the interactions between adjacent droplets when there is more than one droplet ($x_c^0 \coloneqq x_c^N$, $x_c^{N+1} \coloneqq x_c^1$). The parameter η is the friction constant. Following [50], we assume that the surface tension $\gamma(u,s)$ is exerted on the left side ($x = x_c^i - r$) and the right side ($x = x_c^i + r$)

of the droplet, which depends on u and s as below:

$$\gamma(u,s) = \frac{1}{2}\left(\frac{a^2}{a^2+u^2} + \frac{b}{b+s}\right)(\gamma_0 - \gamma_1) + \gamma_1, \tag{3.2}$$

where a and b are positive constants; γ_0 and γ_1 are the maximum and the minimum value of the surface tension, respectively. The maximum γ_0 corresponds to the surface tension of pure water. Note that $s(t,x,y)$ is evaluated at $y=0$.

The interaction of droplets i and j are given by

$$F_0(x_c^i, x_c^j) = \begin{cases} \xi_0 \dfrac{2r - |x_c^i - x_c^j|}{r}, & |x_c^i - x_c^j| \le 2r, \\ 0, & |x_c^i - x_c^j| > 2r. \end{cases} \tag{3.3}$$

where $\xi_0 > 0$ is a constant. Eq. (3.3) describes the excluded volume effect, where the two droplets interact repulsively only when they overlap. This effect prevents overtaking of adjacent droplets and thus preserves the initial ordering. Note that droplet $i-1$ lies on the left side of i and, therefore, the force exerted on i by $i-1$ has the positive sign in Eq. (3.1); Similarly the force on i by $i+1$ has the negative sign.

The equation for $u(t,x)$ is considered at the air/water interface. The first term represents one-dimensional diffusion with diffusion coefficient d_u. The subsequent terms describe the supply of ES molecules from each droplet, condensation of ES from the air phase, evaporation of ES into the air phase, and the formation of SDS-ES complexes, respectively, with k_0, k_a, k_u, and k_{us} the rate constants. The constants u_0, w_0, and c_0 are the saturation concentrations of u, w, and c, respectively. The supply of ES molecules term implies the amount of ES molecules distributed from the droplet. Therefore, the ES concentration at the air/water interface increases but, the supplied amount decreases as ES saturation approaches. The condensation means the movement of ES molecules from the air to the air/water interface. Thus, the ES concentration at the air/water interface increases and the movement decreases as ES saturation approaches. The evaporation also means the movement of ES molecules from the air/water interface to the air. So, the ES concentration at the air/water interface decreases, and the movement decreases as ES saturation in the air approaches. By the complex formation, the ES concentration decreases because of consuming ES molecules when combining with SDS molecules. The complex formation decreases as the complex saturation approaches.

The supply and the evaporation occur inside and outside of the region covered with droplet i, respectively, which is characterized by $\chi_i^+(x)$ and $\chi_i^-(x)$:

$$\chi_i^+(x) = \begin{cases} 1, & |x - x_c^i| \le r, \\ 0, & |x - x_c^i| > r, \end{cases} \qquad \chi_i^-(x) = 1 - \chi_i^+(x). \tag{3.4}$$

The dependence of the complex formation on s is given by the following Michaelis-Menten type function:

$$f(s) = \frac{\alpha s}{\beta + s}. \tag{3.5}$$

where α and β are the maximum rate and the Michaelis constant, respectively.

The last three equations describe diffusion of $s(t, x, y)$ and $c(t, x, y)$ in the upper phase, and $w(t, x, y)$ in the air phase, respectively, with Δ the two-dimensional Laplacian and d_s, d_c, and d_w the diffusion coefficients. The boundaries of three equations play an important role in this system.

3.2.2 The boundary conditions

In the horizontal direction, we set the periodic boundary conditions. This boundary condition is equivalent to considering an annular water channel with a narrow channel width, as in the experimental setup.

$$u(t,0) = u(t,L_x), \quad \frac{\partial u}{\partial x}(t,0) = \frac{\partial u}{\partial x}(t,L_x), \tag{3.6}$$

$$s(t,0,y) = s(t,L_x,y), \quad \frac{\partial s}{\partial x}(t,0,y) = \frac{\partial s}{\partial x}(t,L_x,y), \tag{3.7}$$

$$c(t,0,y) = c(t,L_x,y), \quad \frac{\partial c}{\partial x}(t,0,y) = \frac{\partial c}{\partial x}(t,L_x,y), \tag{3.8}$$

$$w(t,0,y) = w(t,L_x,y), \quad \frac{\partial w}{\partial x}(t,0,y) = \frac{\partial w}{\partial x}(t,L_x,y). \tag{3.9}$$

where $t > 0$, $x \in (0, L_x)$, and $y \in (0, L_y)$. In the vertical direction, we assign the following boundary conditions depending on δ, 0, and L_y:

$$d_s \frac{\partial s}{\partial y}(t,x,-\delta) = -d_1(s_0 - s(t,x,-\delta)), \tag{3.10}$$

$$d_c \frac{\partial c}{\partial y}(t,x,-\delta) = d_2 c(t,x,-\delta), \tag{3.11}$$

$$d_s \frac{\partial s}{\partial y}(t,x,0) = -k_{us}\left(1 - \frac{c(t,x,0)}{c_0}\right) f(s(t,x,0))u(t,x), \tag{3.12}$$

$$d_c \frac{\partial c}{\partial y}(t,x,0) = k_{us}\left(1 - \frac{c(t,x,0)}{c_0}\right) f(s(t,x,0))u(t,x), \tag{3.13}$$

$$\begin{aligned} d_w \frac{\partial w}{\partial y}(t,x,0) = & -\sum_{i=1}^{N} \chi_i^-(x) k_u \left(1 - \frac{w(t,x,0)}{w_0}\right) u(t,x) \\ & + k_a w(t,x,0)\left(1 - \frac{u(t,x)}{u_0}\right), \end{aligned} \tag{3.14}$$

$$d_w \frac{\partial w}{\partial y}(t,x,L_y) = -k_w w(t,x,L_y). \tag{3.15}$$

Conditions (3.10) and (3.11) at $y = -\delta$ represent diffusion between the upper phase and the lower phase of the water region. The constant s_0 is the initial concentration of SDS. In the lower phase the concentrations remain unchanged so that $s = s_0$ and $c = 0$, according to assumption 1, with diffusion constants d_1 and d_2. At $y = 0$, conditions (3.12) and (3.13) reflect the formation of SDS-ES complexes, and condition (3.14) corresponds to evaporation and condensation of ES. Condition (3.15) at $y = L_y$ represents the effect of the cover on the channel. The parameter $k_w = 0$ implies the zero-flux at $y = L_y$, which corresponds to the closed cover situation; $k_w > 0$ implies a non-zero flux, which corresponds to the opened cover situation.

3.2.3 The initial conditions

Since the channel is filled only with SDS surfactant solution and the ES droplet not places on the air/water interface, in the beginning, there are no complex concentration of ES and SDS molecules and the ES concentration. In addition, the ES concentration in the air phase not exists by no evaporation. Therefore, we set the initial conditions to conduct simulations for the two-dimensional model as follows:

$$\begin{aligned} u(0,x,y) &= 0, \quad s(0,x,y) = s_0, \\ c(0,x,y) &= 0, \quad w(0,x,y) = 0. \end{aligned} \tag{3.16}$$

Since the initial concentration of SDS, s_0, is the unique variable in the initial conditions, it is crucial to choose a suitable s_0.

3.3 The excluded volume effect

In this mathematical model, only the excluded volume effect is considered between two droplets. We will show that clustering dynamics of droplets are still observed without the lateral capillary forces in the results section. On the other hand, in [13], both the excluded volume effect and the lateral capillary forces are considered by using the following function:

$$F_{capillary}(x_c^i, x_c^j) = \begin{cases} \xi \mathrm{e}^{-2qr} \dfrac{(2-\varepsilon)r - |x_c^i - x_c^j|}{\varepsilon r}, & |x_c^i - x_c^j| \le 2r, \\ -\xi \mathrm{e}^{-q(|x_c^i - x_c^j|)}, & |x_c^i - x_c^j| > 2r. \end{cases} \tag{3.17}$$

This force describes attractive long-range interaction and short-range repulsive interaction, with ξ the interaction strength. The parameter ε adjusts the range of repulsive

interaction: $F_{capillary}$ becomes positive (repulsive) when $|x_c^i - x_c^j| < (2-\varepsilon)r$. The capillary length is represented by q^{-1}.

The function F_0 in our model can be interpreted as an approximation of Eq. (3.17) by taking the capillary length $q^{-1} \to 0$ in the following sense. Assuming q dependence of ε as $\varepsilon = \mathrm{e}^{-2qr}\kappa$, and taking $q \to \infty$ while keeping ξ and κ as constants, we obtain

$$\lim_{q\to\infty} F_{capillary}(x_c^i, x_c^j) = F_0(x_c^i, x_c^j), \tag{3.18}$$

with the parameter ξ_0 in Eq. (3.3) defined as $\xi_0 \coloneqq \xi/\kappa$. Figure 3.2 shows the two functions F_0 and $F_{capillary}$.

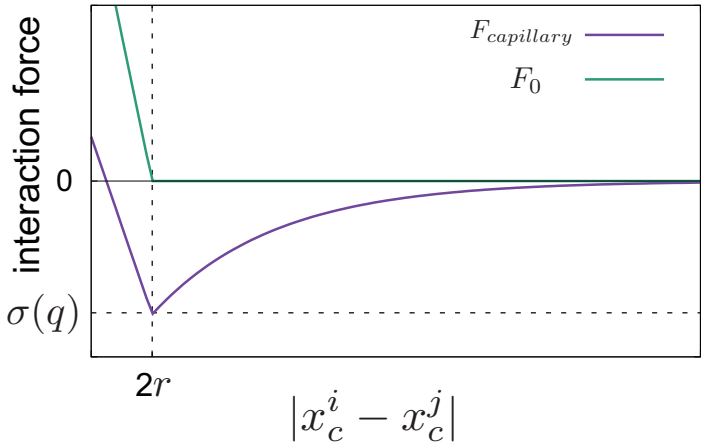

Figure 3.2: $F_{capillary}$ describes the long-range attractive force due to the lateral capillary effect and the short-range repulsive force due to the excluded volume effect. The function F_0 is derived from $F_{capillary}$ by taking $q \to \infty$ and contains only the repulsive part.

The minimum of $F_{capillary}$, which is given by $\sigma(q) = -\xi e^{-2qr}$, approaches zero as $q \to \infty$. This limit corresponds to neglecting the attractive interaction originated from the lateral capillary effect. Note that $F_{capillary}$ is still attractive when the distance is below $2r$, which implies a slight deformation of the droplet due to attraction, whereas F_0, which is used in this work, has an equilibrium point at $2r$. Making similar assumptions, we have previously constructed a model for a single Butyl salicylate (BS) droplet [43]. The main difference is that the present model includes the air phase. Also, in the present model, we focus on the collective behavior of droplets, whereas in the previous model, the focus is on the behavior of a single droplet.

3.4 Nondimensionalization

Taking advantage of parameters L_y, c_0, k_{us}, and η, we can construct the scales of the length, the time, the mass, and the number of molecules as L_y, $1/k_{us}$, $\eta L_y/k_{us}$,

and $c_0 L_y^2$, respectively, with which we non-dimensionalize the variables and the other parameters as

$$\tilde{t} = k_{us}t, \quad \tilde{x} = \frac{1}{L_y}x, \quad \tilde{x}_c^i(t) = \frac{1}{L_y}x_c^i(t),$$
$$\tilde{u}(t,x) = \frac{1}{c_0 L_y}u(t,x), \quad \tilde{c}(t,x,y) = \frac{1}{c_0}c(t,x,y),$$
$$\tilde{s}(t,x,y) = \frac{1}{c_0}s(t,x,y), \quad \tilde{w}(t,x,y) = \frac{1}{c_0}w(t,x,y),$$
$$\tilde{r} = \frac{1}{L_y}r, \quad \tilde{\delta} = \frac{1}{L_y}\delta, \quad \tilde{L}_x = \frac{1}{L_y}L_x,$$
$$\tilde{u}_0 = \frac{1}{c_0 L_y}u_0, \quad \tilde{s}_0 = \frac{1}{c_0}s_0, \quad \tilde{w}_0 = \frac{1}{c_0}w_0,$$
$$\tilde{d}_u = \frac{1}{k_{us}L_y^2}d_u, \quad \tilde{d}_s = \frac{1}{k_{us}L_y^2}d_s, \quad \tilde{d}_c = \frac{1}{k_{us}L_y^2}d_c, \quad \tilde{d}_w = \frac{1}{k_{us}L_y^2}d_w,$$
$$\tilde{d}_1 = \frac{1}{k_{us}L_y}d_1, \quad \tilde{d}_2 = \frac{1}{k_{us}L_y}d_2, \quad \tilde{k}_0 = \frac{1}{c_0 k_{us}L_y}k_0,$$
$$\tilde{k}_u = \frac{1}{k_{us}}k_u, \quad \tilde{k}_a = \frac{1}{k_{us}L_y}k_a, \quad \tilde{k}_w = \frac{1}{k_{us}L_y}k_w,$$
$$\tilde{\alpha} = \alpha, \quad \tilde{\beta} = \frac{1}{c_0}\beta, \quad \tilde{a} = \frac{1}{c_0 L_y}a, \quad \tilde{b} = \frac{1}{c_0}b,$$
$$\tilde{\gamma_0} = \frac{1}{\eta k_{us}L_y}\gamma_0, \quad \tilde{\gamma_1} = \frac{1}{\eta k_{us}L_y}\gamma_1, \quad \tilde{\xi_0} = \frac{1}{\eta k_{us}L_y^2}\xi_0.$$

Equivalently, we can reinterpret all variables and parameters in Equations (3.1)-(3.15) as nondimensionalized ones in the above sense, with $L_y = c_0 = \eta = k_{us} = 1$.

Applying the above non-dimensionalized parameters, the mathematical model (3.1)

can be arranged as follows:

$$
\begin{cases}
\dfrac{d\tilde{x}_c^i}{d\tilde{t}} = \left[\tilde{\gamma}\big(\tilde{u}(\tilde{t},\tilde{x}_c^i+\tilde{r}),\tilde{s}(t,\tilde{x}_c^i+\tilde{r},0)\big) - \tilde{\gamma}\big(\tilde{u}(\tilde{t},\tilde{x}_c^i-\tilde{r}),\tilde{s}(t,\tilde{x}_c^i-\tilde{r},0)\big)\right], \\
\qquad\quad + \dfrac{1}{2\tilde{r}}\left[\tilde{F}_0(\tilde{x}_c^i,\tilde{x}_c^{i-1}) - \tilde{F}_0(\tilde{x}_c^i,\tilde{x}_c^{i+1})\right],\ \tilde{t}>0, \\
\dfrac{\partial\tilde{u}}{\partial\tilde{t}} = \tilde{d}_u\dfrac{\partial^2\tilde{u}}{\partial\tilde{x}^2} + \displaystyle\sum_{i=1}^{N}\tilde{\chi}_i^+(\tilde{x})\tilde{k}_0\left(1-\frac{\tilde{u}(\tilde{t},\tilde{x})}{\tilde{u}_0}\right) + \tilde{k}_a\tilde{w}(\tilde{t},\tilde{x},0)\left(1-\frac{\tilde{u}(\tilde{t},\tilde{x})}{\tilde{u}_0}\right) \\
\qquad\quad - \displaystyle\sum_{i=1}^{N}\tilde{\chi}_i^-(\tilde{x})\tilde{k}_u\left(1-\frac{\tilde{w}(\tilde{t},\tilde{x},0)}{\tilde{w}_0}\right)\tilde{u}(\tilde{t},\tilde{x}) \\
\qquad\quad - (1-\tilde{c}(\tilde{t},\tilde{x},0))\tilde{f}(\tilde{s}(\tilde{t},\tilde{x},0))\tilde{u}(\tilde{t},\tilde{x}), \quad \tilde{t}>0,\ \tilde{x}\in(0,\tilde{L_x}), \\
\dfrac{\partial\tilde{s}}{\partial\tilde{t}} = \tilde{d}_s\Delta\tilde{s}, \quad \tilde{t}>0,\ (\tilde{x},\tilde{y})\in(0,\tilde{L_x})\times(-\tilde{\delta},0), \\
\dfrac{\partial\tilde{c}}{\partial\tilde{t}} = \tilde{d}_c\Delta\tilde{c}, \quad \tilde{t}>0,\ (\tilde{x},\tilde{y})\in(0,\tilde{L_x})\times(-\tilde{\delta},0), \\
\dfrac{\partial\tilde{w}}{\partial\tilde{t}} = \tilde{d}_w\Delta\tilde{w}, \quad \tilde{t}>0,\ (\tilde{x},\tilde{y})\in(0,\tilde{L_x})\times(0,\tilde{L_y}).
\end{cases}
\tag{3.19}
$$

Likewise, the surface tension Eq. (3.2), the excluded volume effect Eq. (3.3), the characteristic Eq. (3.4), the Michaelis-Menten functions Eq. (3.5), and the initial conditions Eq. (3.16) in the two-dimensional model are also able to be rewritten as below:

$$
\tilde{\gamma}(\tilde{u},\tilde{s}) = \frac{1}{2}\left(\frac{\tilde{a}^2}{\tilde{a}^2+\tilde{u}^2}+\frac{\tilde{b}}{\tilde{b}+\tilde{s}}\right)(\tilde{\gamma}_0-\tilde{\gamma}_1)+\tilde{\gamma}_1, \tag{3.20}
$$

$$
\tilde{F}_0(\tilde{x}_c^i,\tilde{x}_c^j) = \begin{cases} \tilde{\xi}_0\dfrac{2\tilde{r}-|\tilde{x}_c^i-\tilde{x}_c^j|}{\tilde{r}}, & |\tilde{x}_c^i-\tilde{x}_c^j|\le 2\tilde{r}, \\ 0, & |\tilde{x}_c^i-\tilde{x}_c^j|>2\tilde{r}, \end{cases} \tag{3.21}
$$

$$
\tilde{\chi}_i^+(\tilde{x}) = \begin{cases} 1, & |\tilde{x}-\tilde{x}_c^i|\le\tilde{r}, \\ 0, & |\tilde{x}-\tilde{x}_c^i|>\tilde{r}, \end{cases} \qquad \tilde{\chi}_i^-(\tilde{x}) = 1-\tilde{\chi}_i^+(\tilde{x}), \tag{3.22}
$$

$$
\tilde{f}(\tilde{s}) = \frac{\tilde{\alpha}\tilde{s}}{\tilde{\beta}+\tilde{s}}, \tag{3.23}
$$

$$
\begin{aligned}
&\tilde{u}(0,\tilde{x},\tilde{y}) = 0, \quad \tilde{s}(0,\tilde{x},\tilde{y}) = \tilde{s}_0, \\
&\tilde{c}(0,\tilde{x},\tilde{y}) = 0, \quad \tilde{w}(0,\tilde{x},\tilde{y}) = 0.
\end{aligned} \tag{3.24}
$$

The vertical boundary conditions depending on δ, 0, and L_y, Eq. (3.10), Eq. (3.11), Eq. (3.12), Eq. (3.13), Eq. (3.14), and Eq. (3.15), can be expressed by the nondimensionalized parameters as follows:

$$\tilde{d}_s \frac{\partial \tilde{s}}{\partial \tilde{y}}(\tilde{t}, \tilde{x}, -\tilde{\delta}) = -\tilde{d}_1(\tilde{s}_0 - \tilde{s}(\tilde{t}, \tilde{x}, -\tilde{\delta})), \tag{3.25}$$

$$\tilde{d}_c \frac{\partial \tilde{c}}{\partial \tilde{y}}(\tilde{t}, \tilde{x}, -\tilde{\delta}) = \tilde{d}_2 \tilde{c}(\tilde{t}, \tilde{x}, -\tilde{\delta}), \tag{3.26}$$

$$\tilde{d}_s \frac{\partial \tilde{s}}{\partial \tilde{y}}(\tilde{t}, \tilde{x}, 0) = -(1 - \tilde{c}(\tilde{t}, \tilde{x}, 0))\tilde{f}(\tilde{s}(\tilde{t}, \tilde{x}, 0))\tilde{u}(\tilde{t}, \tilde{x}), \tag{3.27}$$

$$\tilde{d}_c \frac{\partial \tilde{c}}{\partial \tilde{y}}(\tilde{t}, \tilde{x}, 0) = (1 - \tilde{c}(\tilde{t}, \tilde{x}, 0))\tilde{f}(\tilde{s}(\tilde{t}, \tilde{x}, 0))\tilde{u}(\tilde{t}, \tilde{x}), \tag{3.28}$$

$$\begin{aligned} \tilde{d}_w \frac{\partial \tilde{w}}{\partial \tilde{y}}(\tilde{t}, \tilde{x}, 0) = & -\sum_{i=1}^{N} \tilde{\chi}_i^-(\tilde{x}) \tilde{k}_u \left(1 - \frac{\tilde{w}(\tilde{t}, \tilde{x}, 0)}{\tilde{w}_0}\right) \tilde{u}(\tilde{t}, \tilde{x}) \\ & + \tilde{k}_a \tilde{w}(\tilde{t}, \tilde{x}, 0)\left(1 - \frac{\tilde{u}(\tilde{t}, \tilde{x})}{\tilde{u}_0}\right), \end{aligned} \tag{3.29}$$

$$\tilde{d}_w \frac{\partial \tilde{w}}{\partial \tilde{y}}(\tilde{t}, \tilde{x}, 1) = -\tilde{k}_w \tilde{w}(\tilde{t}, \tilde{x}, 1). \tag{3.30}$$

3.5 Numerical results

In this section, we show a variety of simulation results for the two-dimensional model. The numerical simulations investigate the behavior of droplets based on a two-dimensional model with a periodic boundary condition for the horizon and assigned boundary conditions for vertical. We find suitable parameters set and reproduce the clustering dynamics of both a single droplet and multiple droplets through the simulations. As mentioned above, the presence/absence of the cover in the experiment is represented in our two-dimensional model by changing the parameter $\tilde{k}_w$; here, we set $\tilde{k}_w = 0$ when the cover is closed and $\tilde{k}_w = \tilde{k}_w^+ > 0$ when the cover is open. The horizontal length $\tilde{L}_x$ depends on the number of droplets N. To investigate the mechanisms for each motion for a single droplet and the clustering dynamics for multiple droplets, we take into account the each concentration, $\tilde{u}$, $\tilde{s}$, $\tilde{c}$, and $\tilde{w}$. The concentrations are evaluated at $\tilde{y} = 0$ and normalized by $\tilde{u}_0$, $\tilde{s}_0$, $\tilde{c}_0$, and $\tilde{w}_0$. They are distinguished as each color, shown in Fig. 3.3.

u/u_0 s/s_0 c/c_0 w/w_0

Figure 3.3: Distinction of the normalized concentration.

3.5.1 A single droplet

We choose the parameter values in order to simulate the two-dimensional model as follows : $\tilde{\delta} = 1.0$, $\tilde{r} = 2.5$, $\tilde{d_u} = 300$, $\tilde{d_s} = 60$, $\tilde{d_c} = 30$, $\tilde{d_w} = 3.0 \times 10^6$, $\tilde{d_1} = 4.8 \times 10^{-2}$, $\tilde{d_2} = 0.15$, $\tilde{u}_0 = 0.018$, $\tilde{w}_0 = 0.001$, $\tilde{k}_0 = 3.0$, $\tilde{k}_u = 80$, $\tilde{k}_a = 2.4 \times 10^3$, $\tilde{k}_w^+ = 3 \times 10^7$, $\tilde{\alpha} = 1.0$, $\tilde{\beta} = 0.1$, $\tilde{\gamma}_0 = 1.0 \times 10^5$, $\tilde{\gamma}_1 = 0.0$, $\tilde{a} = 0.18$, $\tilde{b} = 3.0$, $\tilde{\xi}_0 = 5.0 \times 10^3$. These parameter values have been chosen in such a way that the same behavior as in [43] is qualitatively reproduced for a single droplet. The initial concentration of SDS, $\tilde{s}_0$, is chosen at first as a control parameter. As the initial conditions we set $\tilde{u}(0, \tilde{x}) = 0$, $\tilde{s}(0, \tilde{x}, \tilde{y}) = \tilde{s}_0$, $\tilde{c}(0, \tilde{x}, \tilde{y}) = 0$, and $\tilde{w}(0, \tilde{x}, \tilde{y}) = 0$. Note that s_0 appears also in the boundary condition between the lower and the upper phases in Eq. (3.25). The SDS concentration on the surface can decrease through chemical reactions but is continuously supplied from the lower phase. Below, to compare our current model to the previous model [43], we first investigate the effect of $\tilde{s}_0$. Later on, we fix the $\tilde{s}_0$ value with which a single droplet exhibits oscillatory motions.

3.5.1.1 Phase diagram

To select a suitable $\tilde{s}_0$, we check the phase diagram, which means the behavior of a single droplet depending on $\tilde{s}_0$. Therefore, we study the behavior of a single droplet by varying the initial SDS concentration $\tilde{s}_0$ within the range $[0.5, 8.0]$ under the open cover condition ($\tilde{k}_w = \tilde{k}_w^+$). We set $\tilde{L}_x = 40$. We find three distinct kinds of droplet behavior identical to the chemical experiment results (Fig. 1.9, and Fig. 1.10, Fig. 1.11): the stationary state, the oscillatory state, and the rotating state, as shown in Fig. 3.4(a). Although experiments in [43] were conducted in the water tank, it is an identity of a narrow channel under the periodic boundary condition. Here the amplitude ($\Delta\theta$) is defined by the range of the angular position $\theta = 2\pi x/\tilde{L}_x$ covered by the droplet after settling in a steady state. Note that $\Delta\theta$ is zero for the stationary state and is equal to 2π for the rotating state. The appearance of these three states as increasing SDS concentration in this order is consistent with the previous result [43]. As shown in Fig. 3.4(b), the oscillation period increases as s_0 in the oscillatory regime. In the rotating state, the period of rotation only slightly decreases. Note that the rotation period depends on the system size $\tilde{L}_x$. T means the time taken for one round trip around the center of the oscillation. We can confirm that period, and amplitude changes are consistent because the amplitude increases as the droplet regularly oscillate as the $\tilde{s}_0$ increases, as shown in Fig. 3.5. At $\tilde{s}_0 = 5.55$, which is the point of transition from the oscillatory motion to the rotating motion, the droplet irregularly oscillates, and

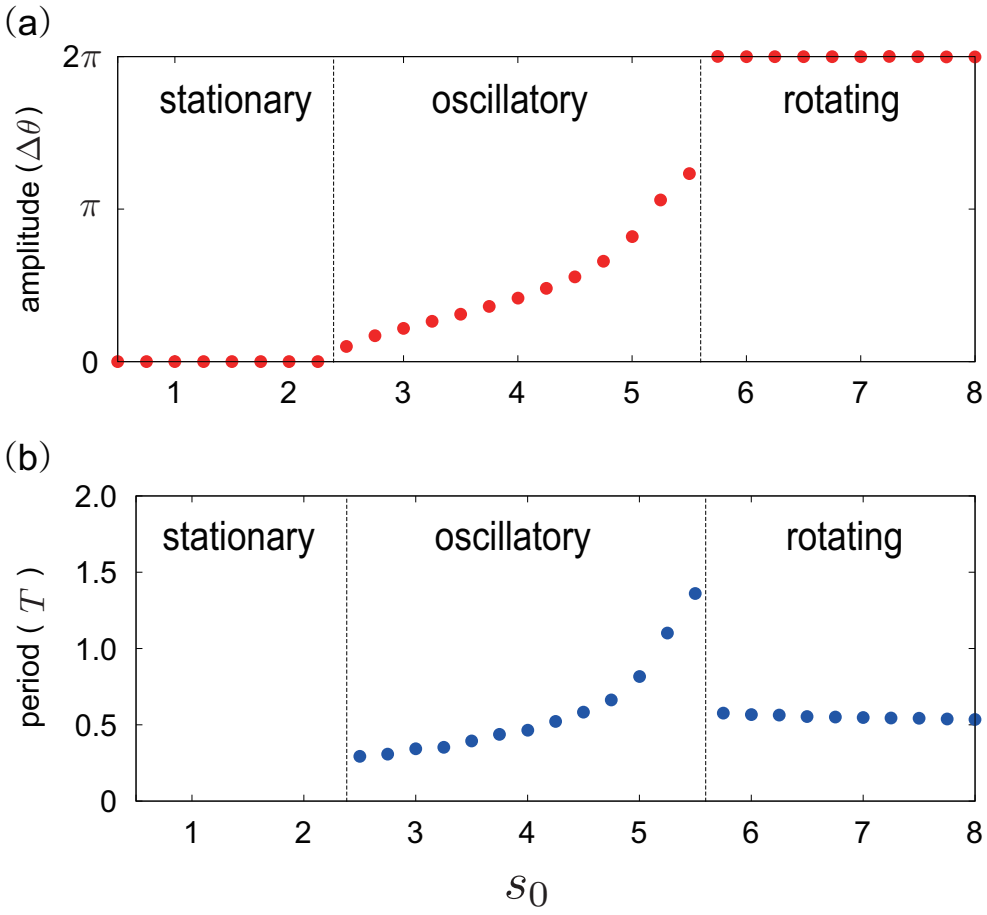

Figure 3.4: Three distinct states of a single droplet observed by changing the initial SDS concentration $\tilde{s}_0$, under an open cover condition. (a) The oscillation amplitude measured in terms of azimuth: in the oscillating motion, it is defined by the distance covered by one oscillation multiplied by $2\pi/\tilde{L}_x$. The amplitude is 2π for the rotating motion. (b) The oscillation period depending on $\tilde{s}_0$.

the motion is converted into the rotating state at over $\tilde{s}_0 = 5.55$, as shown in Fig. 3.6.

Thus, we finally choose $\tilde{s}_0 = 5.25$, which corresponds to the oscillatory regime in Fig. 3.4.

3.5.1.2 The effect of the cover on a single droplet behavior

The effect of the cover is studied in the following way: a simulation is run with the cover opened ($\tilde{k}_w = \tilde{k}_w^+$) until the droplet reaches a steady-state; then the cover is closed ($\tilde{k}_w = 0$), and the simulation is continued until, again, it reaches a steady-state; finally, the cover is removed ($\tilde{k}_w = \tilde{k}_w^+$) and the simulation is continued. At first, we calculate an open cover case. Then, it consistently takes place the oscillatory motion

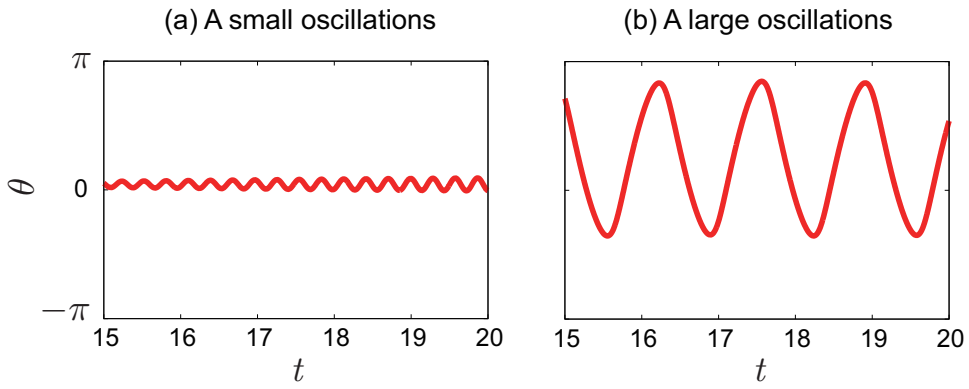

Figure 3.5: A regular oscillatory motion of the droplet. The amplitude and period are increased as $\tilde{s}_0$ increases. (a): The oscillations at $\tilde{s}_0 = 2.5$, (b): The oscillations at $\tilde{s}_0 = 5.25$.

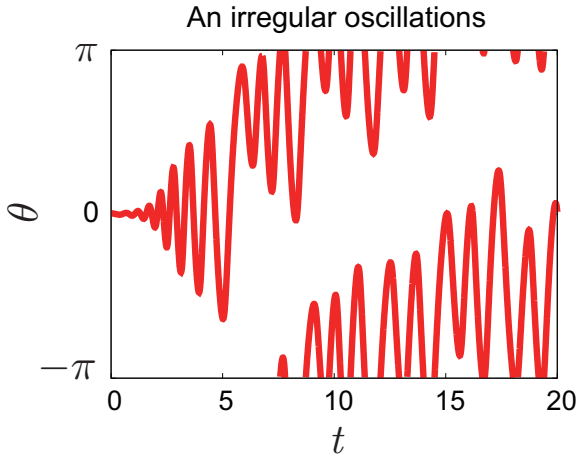

Figure 3.6: An irregular oscillatory motion of the droplet at $\tilde{s}_0 = 5.55$. The amplitude increases and changes irregularly at some point.

when the cover is open, as shown in Fig. 3.7.

Figure 3.8 shows the concentration profiles for $\tilde{u}$, $\tilde{s}$, $\tilde{c}$, and $\tilde{w}$ according to droplet position under an open the cover. The remarkable point is that the ES concentration is the asymmetric profile as a criterion of the center of the droplet when the droplet moves. It represents that the surface tension is higher in front of the droplet than behind it when the droplet moves, from the chemical perspective, because the droplet leaves surface-active molecules behind more than in front of it. Furthermore, we can confirm the profile, which is perfectly reversed when the direction of the droplet is reversed. It implies that the surface tension gradient is periodically reversed.

To proceed a simulation for a closed cover case, the last data of $\tilde{u}$, $\tilde{s}$, $\tilde{c}$, $\tilde{w}$, and the droplet position, $\tilde{x}_c$ is continuously applied as the initial data of a closed cover case. When the cover is closed, the droplet moves for a short time initially and immediately

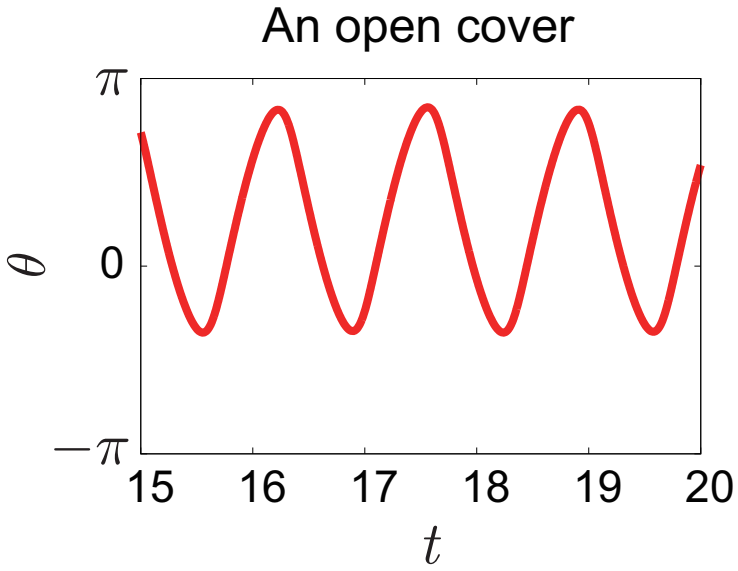

Figure 3.7: Trajectory of a single droplet when an open cover, $\tilde{k}_w = 3 \times 10^7$. The droplet oscillates consistently.

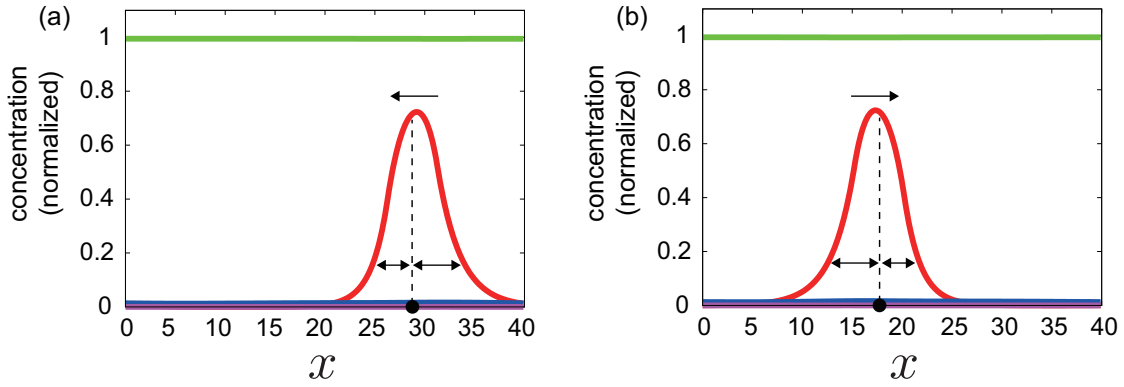

Figure 3.8: Concentration profiles of a single droplet when an open is cover. According to the moving direction, the asymmetric profile of the ES concentration is a criterion of the center of the droplet and reversed profile. (a) Move toward the left side. (b) Move toward the right side.

reaches a stationary state, as shown in Fig. 3.9.

Figure 3.10 shows the concentration profiles for $\tilde{u}$, $\tilde{s}$, $\tilde{c}$, and $\tilde{w}$ according to droplet position under a closed cover. The ES concentration in the air is increased by the cover, which prevents ES molecules from spreading into the air. Since the evaporation of ES molecules on the surface is disturbed by the increase of ES concentration in the air, the ES concentration increases. Therefore, the ES concentration on the surface, as well as in the air, increases under a closed cover case. At the same time, the SDS concentration

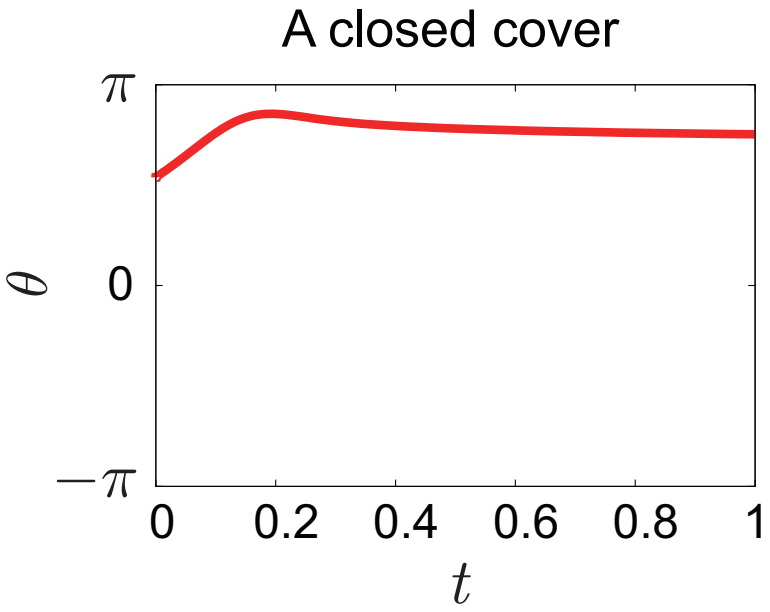

Figure 3.9: Trajectory of a single droplet when the cover is closed, $\tilde{k}_w = 0$. As initial data, the last data of $\tilde{u}$, $\tilde{s}$, $\tilde{c}$, $\tilde{w}$, and droplet position, $\tilde{x}_c$ under an open cover case are applied.

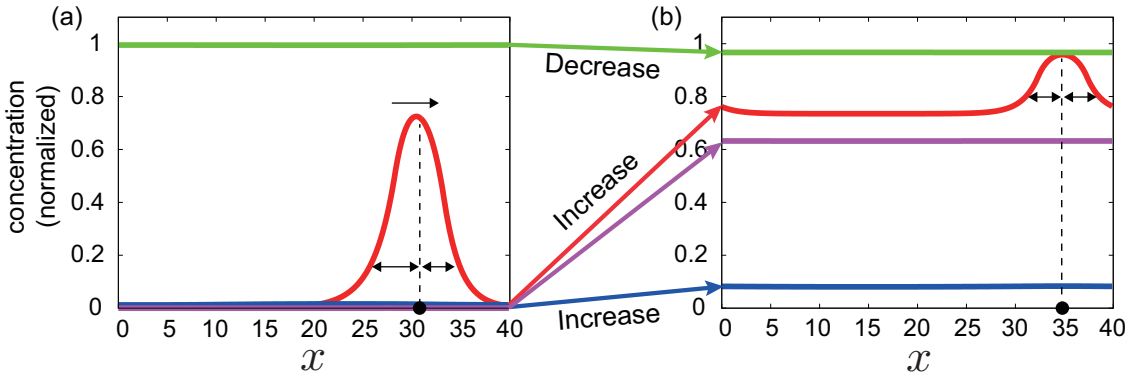

Figure 3.10: Concentration profiles of a single droplet when a closed cover. The asymmetric profile of the ES concentration is converted into the symmetry. (a) Move toward the right side. (b) Reach the stationary state.

decreases due to increased consumption of the SDS molecules because of the increase of the ES concentration, which implies increased ES molecules on the surface. This thing reflects the increase of the complex concentration. Therefore, the SDS concentration and the complex concentration slightly decrease and increases, respectively. When the ES concentration in the air and on the surface increases sufficiently, the droplet starts to stop. The remarkable point is that the ES concentration is the symmetric profile when the droplet reaches the stationary state. Therefore, we find that the ES

concentrations on the surface and in the air significant affect the stationary state and oscillating motion of the droplet.

Likewise a closed cover case, we apply the last data of a closed cover case as the initial data of a removed cover. When the cover is removed, the oscillatory motion is recovered. The late stage of resumed oscillations is shown in Fig. 3.11. We can confirm the regular oscillatory motion of the droplet.

Figure 3.12 shows the concentration profiles for $\tilde{u}$, $\tilde{s}$, $\tilde{c}$, and $\tilde{w}$ according to droplet position, $\tilde{x}_c$ under a removed cover.

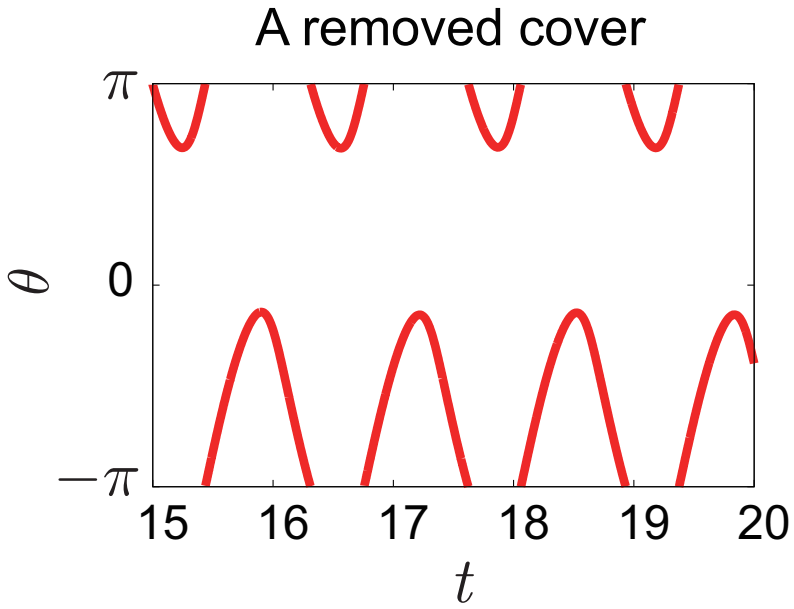

Figure 3.11: Trajectory of a single droplet when a removed cover, $\tilde{k}_w = 3 \times 10^7$. As initial data, the last data of $\tilde{u}$, $\tilde{s}$, $\tilde{c}$, and $\tilde{w}$, and droplet position, $\tilde{x}_c$ are applied under a closed cover. The droplet is restored as the regular oscillatory motion.

Since the effect of the cover is ignored when the cover is removed, the opposite situation to the closed cover takes place. In other words, the ES concentration in the air quickly decreases because the ES molecules are simultaneously spread into the air. The ES concentration on the surface also decreases since the evaporation of ES molecules on the surface recovers. Because the ES molecules are diminished on the surface by evaporation, the SDS concentration is slightly increased since the consumption of SDS molecules decreases. In contrast, the complex concentration decreases due to the reduced formation of the complex. Therefore, the symmetric profile of ES concentration is broken when it restarts to move.

From the oscillatory motion to the stationary state and again oscillatory motion, this behavior change qualitatively agrees with the experimental result (Fig. 2.2), where

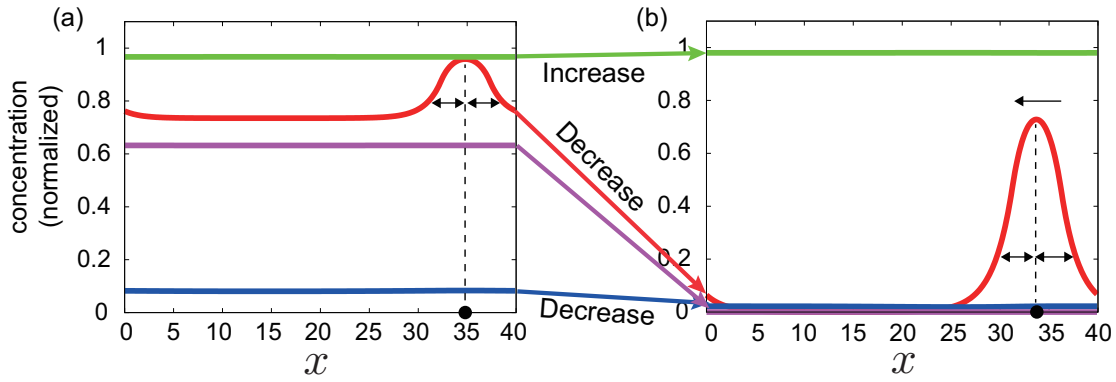

Figure 3.12: Concentration profiles of a single droplet when a removed cover. The symmetric profile of the ES concentration is converted into the asymmetry. (a) The stationary state. (b) Move toward the left side.

an initially oscillating droplet settles in a stationary state. Time $\tilde{t}$ is reset to zero after each change of the cover state under the closed cover condition.

3.5.1.3 Analysis of the oscillatory motion

First of all, as elaborated in the previous work [43], the transition of a single droplet is explained in terms of the profiles of $\tilde{u}$ and $\tilde{s}$, both of which changes the surface tension. The positive peak of $\tilde{u}$ is created around a single droplet, which is the driving force for the droplet. Since $\tilde{u}$ and $\tilde{s}$ are consistently consumed around the droplet due to the complex formation, the profile of $\tilde{s}$ has the inverse peak around the droplet, which contributes to decelerating the droplet, leading to either a stationary state, an oscillatory state, or a rotating state. We numerically check our intuition that the profile of the ES concentration can explain the oscillatory motion. For this purpose, we decompose the surface tension $\tilde{\gamma}(\tilde{u}, \tilde{s})$ into the $\tilde{u}$-dependent and $\tilde{s}$-dependent terms as

$$\tilde{g}(\tilde{u}) = \frac{1}{2}\frac{\tilde{a}^2}{\tilde{a}^2 + \tilde{u}^2}(\tilde{\gamma}_0 - \tilde{\gamma}_1), \quad \tilde{h}(\tilde{s}) = \frac{1}{2}\frac{\tilde{b}}{\tilde{b} + \tilde{s}}(\tilde{\gamma}_0 - \tilde{\gamma}_1), \tag{3.31}$$
$$\tilde{\gamma}(\tilde{u}, \tilde{s}) = \tilde{g}(\tilde{u}) + \tilde{h}(\tilde{s}) + \tilde{\gamma}_1.$$

We have theoretically known that the chemical mechanism of the oscillatory motion occurs by the surface tension difference in subsection 2.3. To compare the surface tension difference on the right-hand and left-hand sides of a droplet, we calculate the

difference of $\tilde{g}(\tilde{u})$, $\tilde{g}(\tilde{s})$ between both ends sides of the droplet, that is,

$$\begin{aligned}\Delta\tilde{g}(\tilde{u}) &= \tilde{g}\big(\tilde{u}(\tilde{t},\tilde{x}_c+\tilde{r})\big) - \tilde{g}\big(\tilde{u}(\tilde{t},\tilde{x}_c-\tilde{r})\big)\\ \Delta\tilde{h}(\tilde{s}) &= \tilde{h}\big(\tilde{s}(\tilde{t},\tilde{x}_c+\tilde{r})\big) - \tilde{h}\big(\tilde{s}(\tilde{t},\tilde{x}_c-\tilde{r})\big)\end{aligned} \tag{3.32}$$

Figure 3.13 means the contribution of the $\tilde{u}$-dependent and the $\tilde{s}$-dependent terms under an open cover and a closed cover. This results provide a confidence for our intuition that the oscillatory motion is dominated by the $\tilde{u}$ because $\Delta\tilde{g}(\tilde{u})$ is bigger than $\Delta\tilde{h}(\tilde{s})$. Note that, although the effect of $\tilde{g}(\tilde{u})$ dominates the surface tension variations, it is still necessary for the effect of $\tilde{g}(\tilde{s})$ to exhibit a self-propelled motion for a droplet. Furthermore, the surface tension is regularly changed when the droplet oscillates, whereas, the surface tension converges to zero when the droplet reaches the stationary state.

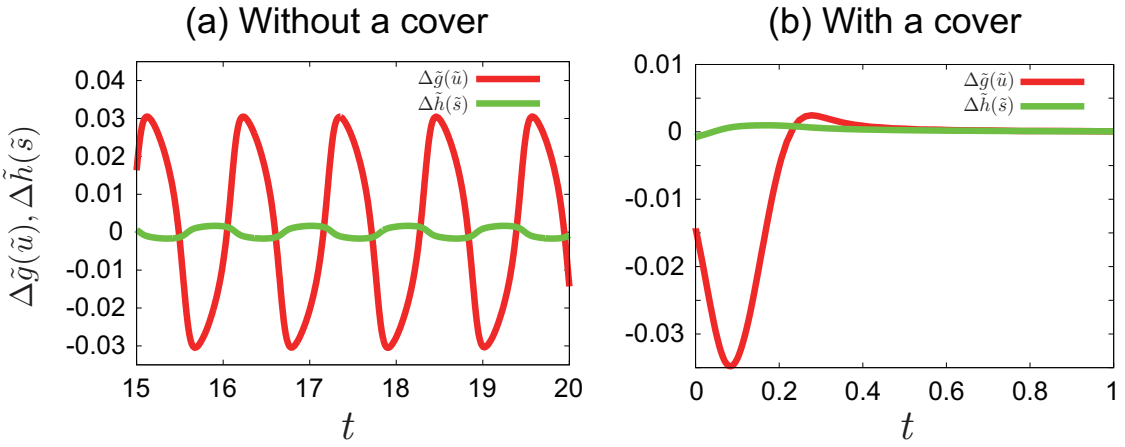

Figure 3.13: Contribution of $\tilde{u}$ and $\tilde{s}$ to the surface tension $\tilde{\gamma}(\tilde{u},\tilde{s})$. (a) The change of the force $\tilde{g}(\tilde{u})$ is larger than the force $\tilde{h}(\tilde{s})$ under an open cover. (b) The change of the all force converges to zero when the droplet reaches the stationary state under a closed cover.

3.5.2 Multiple droplet

In this section, we perform simulations to study the clustering mechanism of multiple droplets for the two-dimensional model. First, we show that our model reproduces experimentally observed clustering for twenty droplets. Then we take advantage of the two-droplet and three-droplet systems to investigate the clustering mechanism.

3.5.2.1 Twenty droplets

To simulate for twenty droplets, we set as $\tilde{L}_x = 300$ because in as much as the oscillatory motion of a single droplet occurs within a specific range among the whole

length of a narrow channel, the length of each simulation was adjusted according to the number of droplets set. We, first, take into account a closed cover condition. We find the following clustering process (Fig. 3.14): In the early stage, nearby droplets approach each other to form three clusters (depicted as P_1 in Fig. 3.14). Note that the distance between the fifth and the sixth droplets from below increases until reaching P_1. The smallest cluster is absorbed into the largest cluster within a short time (P_2 in Fig. 3.14), resulting in the two clusters, which finally merge into a single cluster (P_3 in Fig. 3.14).

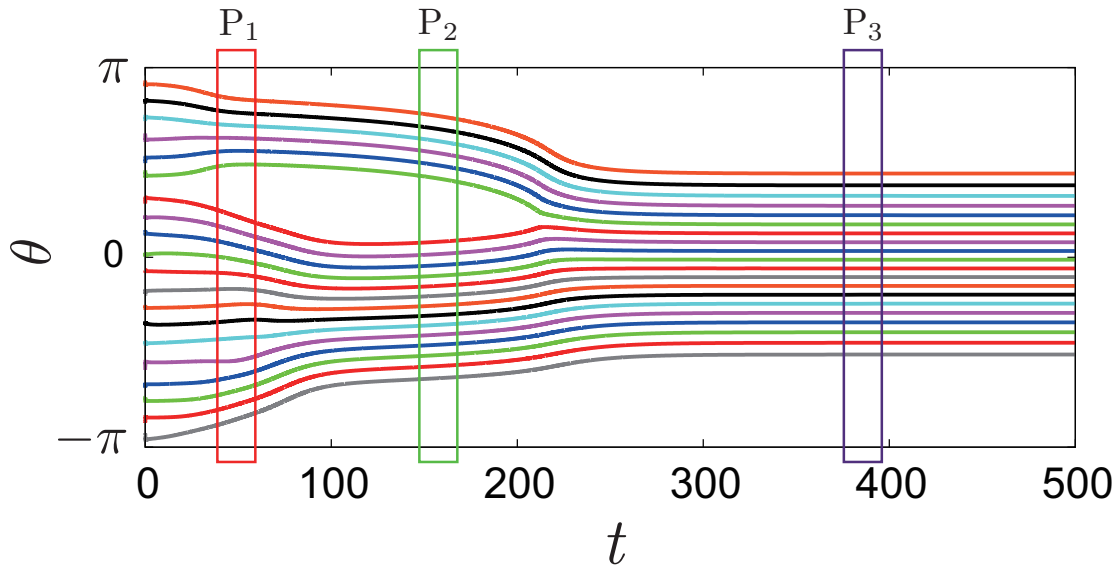

Figure 3.14: Trajectories of 20 droplets with a closed cover. Three distinct stages of clustering process are depicted as P_1 (three clusters), P_2 (two clusters), and P_3 (one cluster).

To investigate the mechanisms for P_1, P_2, and P_3, we take into account the each concentration of $\tilde{u}$, $\tilde{s}$, $\tilde{c}$, and $\tilde{w}$. The concentrations are evaluated at $y = 0$ and normalized by $\tilde{u}_0$, $\tilde{s}_0$, $\tilde{c}_0$, and $\tilde{w}_0$, respectively. Points on the horizontal axis indicate twenty droplets. The three clusters are labeled as c_1, c_2, and c_3.

Figure 3.15(a) focuses on the trajectories that form the three clusters in the beginning, depicted as P_1 in Fig. 3.14. Likewise the results of a single droplet under a closed cover, the concentrations of $\tilde{u}$, $\tilde{w}$ have fairly reached a saturation, and the concentrations of $\tilde{c}$ slightly increased. In the case of cluster formation in the beginning, the spatial profile of SDS concentration at the air/water interface, $\tilde{s}(\tilde{t}, \tilde{x}, 0)$, well captures the clustering process.

In the early stage P_1, the droplets in the largest cluster, c_1 approach each other, simultaneously, the SDS concentration has a bumpy shape. Three clusters are confined in low-concentration regions, separated by three peaks, τ_1, τ_2, and τ_3. The three peak

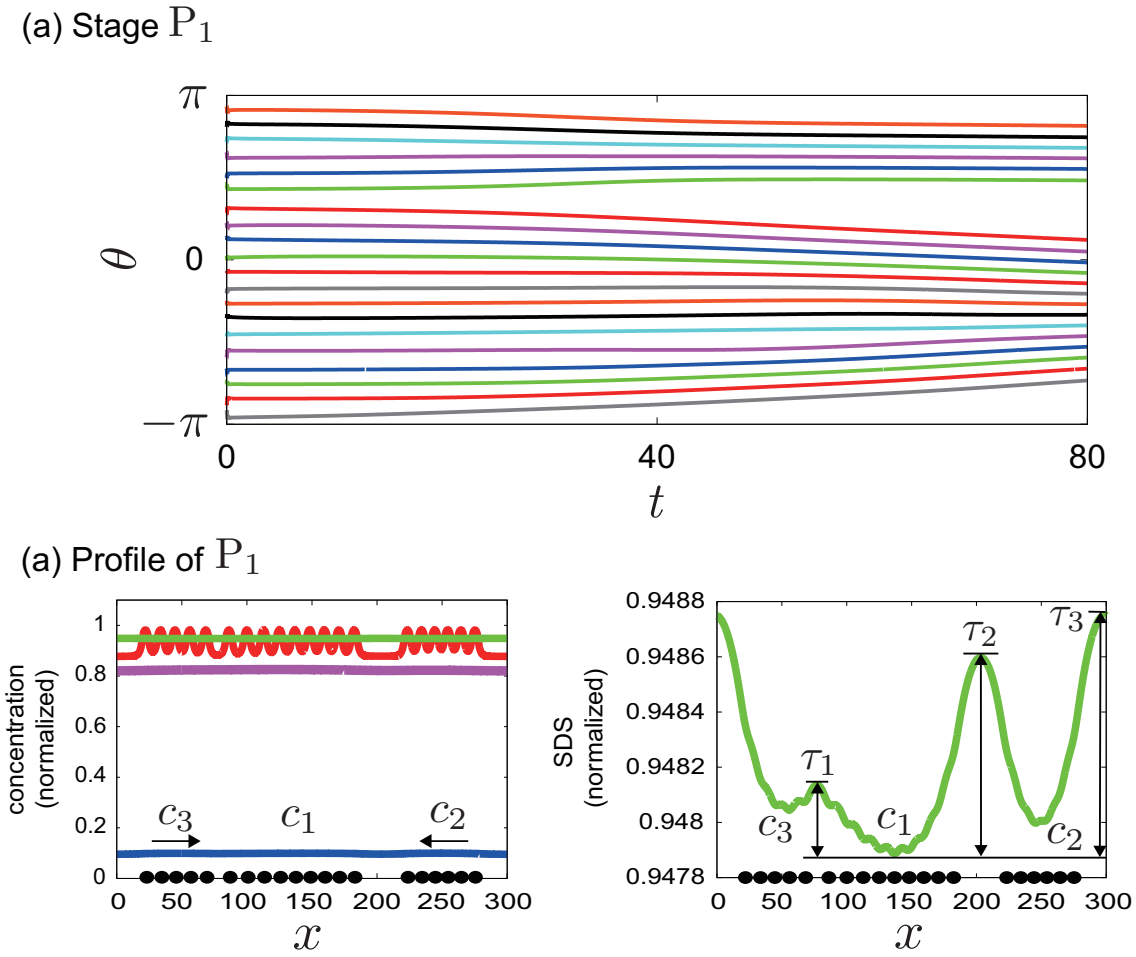

Figure 3.15: (a) The magnification for trajectories of the three clusters depicted as P_1. (b) Profiles of $\tilde{u}$, $\tilde{s}$, $\tilde{c}$, and $\tilde{w}$ for droplets on the air/water interface during the clustering process P_1 in Fig. 3.14. The right side shows the magnification of the profile of $\tilde{s}/\tilde{s}_0$. The peak height of $\tilde{s}/\tilde{s}_0$ from the minimum is denoted by τ_1, τ_2, and τ_3.

height occurred between clusters lead to the surface tension difference since the surface tension, $\tilde{\gamma}(\tilde{u}, \tilde{s})$ is influenced by the SDS concentration, shown in Fig. 3.15(b).

Figure 3.16(a) magnifies the trajectories of the two clusters, depicted as P_2. As the two clusters, c_1, c_2 merged, the one of the peaks, τ_1 disappeared. The rough shape of the largest cluster converted into a smooth one and symmetry, concurrently, and the motion of droplets in the largest cluster reached the stationary state. Two peak separate the two clusters, but they sluggishly attract each other.

Figure 3.17(a) enlarges the trajectories that form the largest cluster in the end, depicted as P_3. As the height of the peak decreases, the two clusters were god close. Finally, in the later stage P_3, a single cluster is confined within the valley of the one-

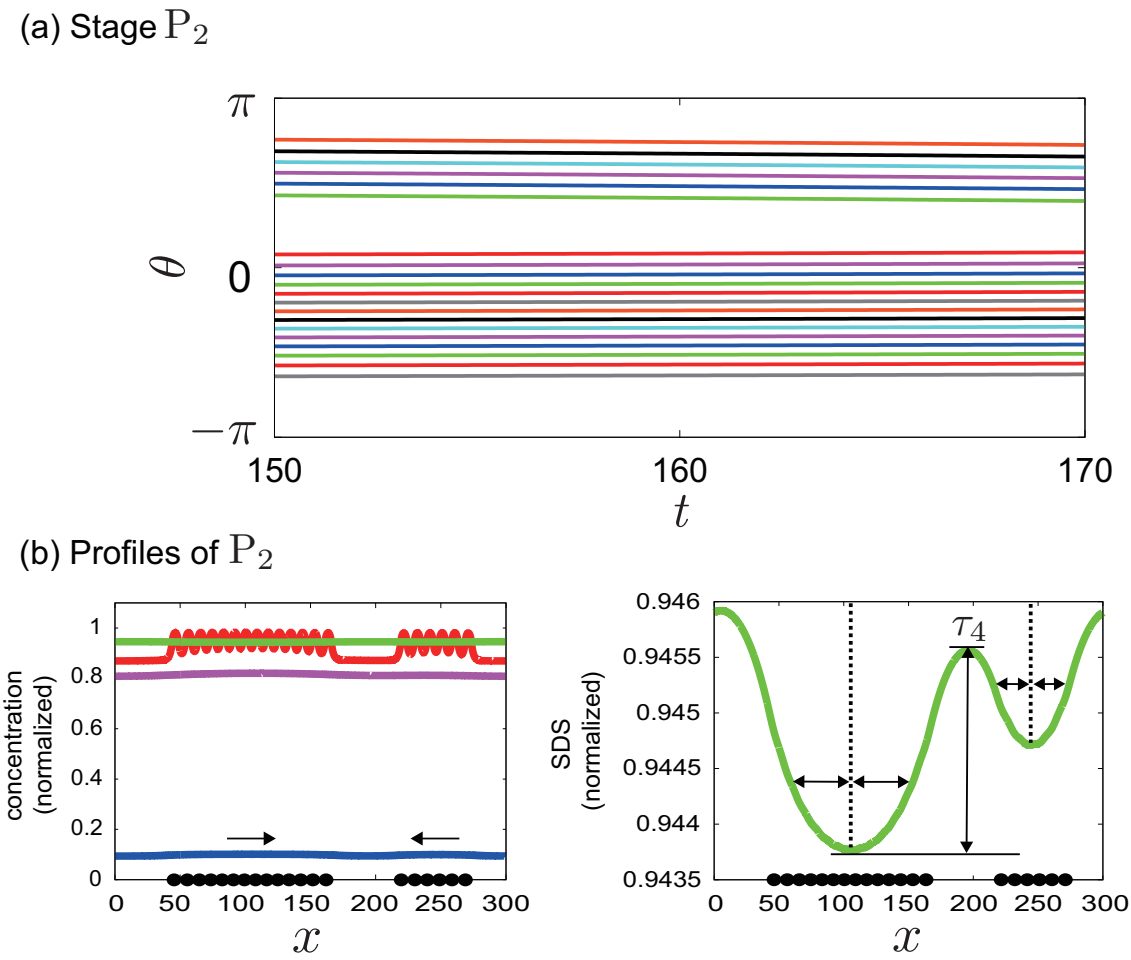

Figure 3.16: Magnification of P_2 in Fig. 3.14. (a) The magnified trajectories of two clusters. (b) Profiles of $\tilde{u}$, $\tilde{s}$, $\tilde{c}$, and $\tilde{w}$ on the air/water interface during the clustering process. The right side shows the enlarged profile of $\tilde{s}/\tilde{s}_0$. The peak height of $\tilde{s}/\tilde{s}_0$ from the minimum is denoted by τ_4.

hump profile of $\tilde{s}$. Since a high concentration of $\tilde{s}$ means low surface tension, the profile of $\tilde{s}$ nicely causes the droplets between the peaks to drive into the valley, resulting in the practical and attractive force between the droplets. Thus, the transition from one stage to the next can be understood by the two factors. One is the cluster size. Viscous friction is proportional to the cluster size, and, therefore, larger clusters have smaller mobility. The other is the surface tension difference of both sides of a cluster, which approximately corresponds to the peak height difference. For example, $\tau_3 > \tau_1$ [Fig. 3.15(b)] means that the surface tension is smaller on the left side of cluster c_3 (the smallest cluster) than on the right side, so that c_3 moves toward the right.

Similarly, $\tau_3 > \tau_2$ implies that the cluster, c_2, moves leftward. Because of $\tau_3 - \tau_2 <$

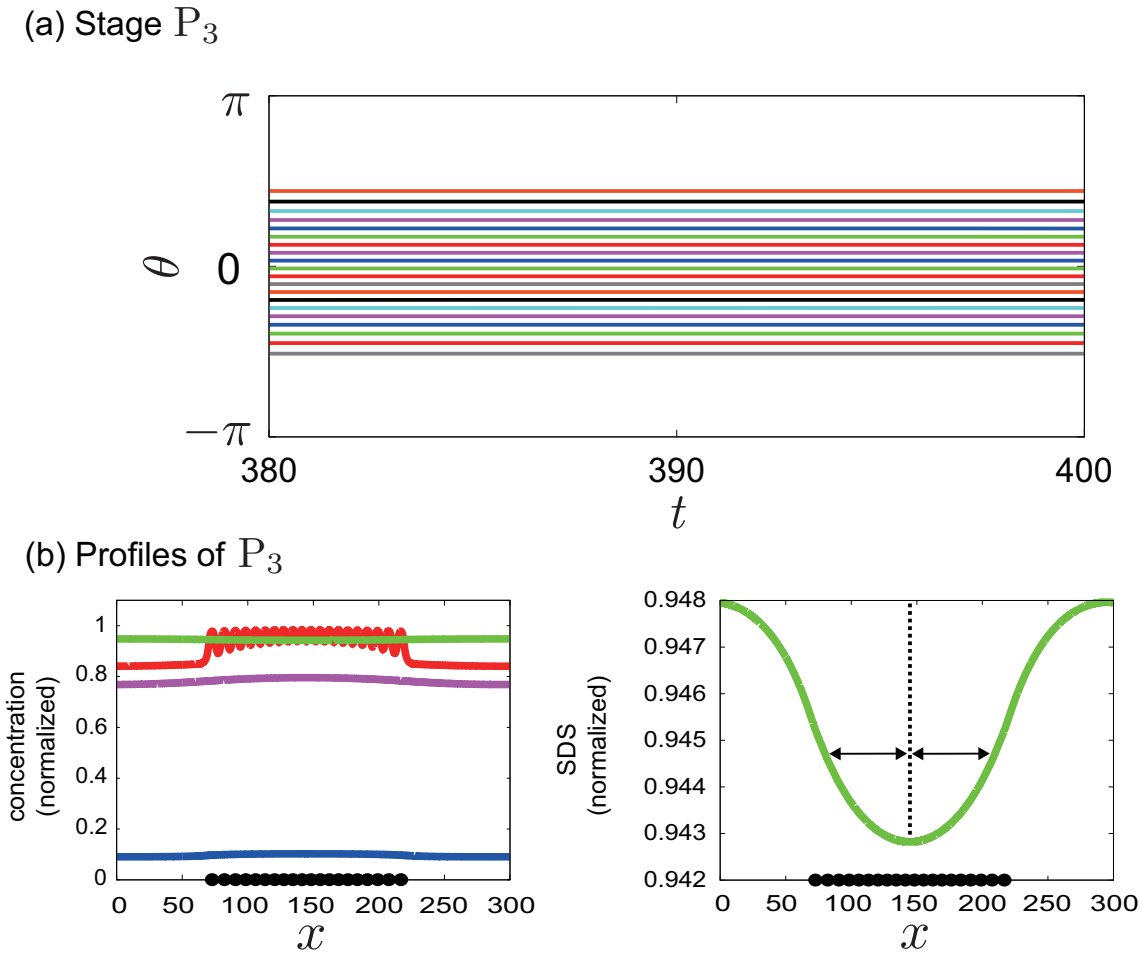

Figure 3.17: (a) The magnification for trajectories of the one cluster depicted as P_3. (b) Profiles of $\tilde{u}$, $\tilde{s}$, $\tilde{c}$, and $\tilde{w}$ for droplets on the air/water interface during the clustering process P_3 in Fig. 3.14. The right side shows the magnification of the profile of $\tilde{s}/\tilde{s}_0$. All peak height of $\tilde{s}/\tilde{s}_0$ from the minimum is vanished.

$\tau_3 - \tau_1$, however, c_3 moves faster than c_2, resulting in c_3 absorbed into c_1 earlier than c_2; and since SDS molecules are consumed due to the complex formation mostly near the droplet regions, the peak that had separated two clusters disappears when they merge.

3.5.2.2 Analysis of clustering dynamics

To confirm the above scenario, we study the cases of $N = 2$ and $N = 3$, with a closed cover. Two and three droplet simulations imply the clustering dynamics of each droplet, as well as the small cluster and a single droplet, respectively.

For $N = 2$ we choose $\tilde{L}_x = 60$. As shown in Fig. 3.18, two droplets approach each

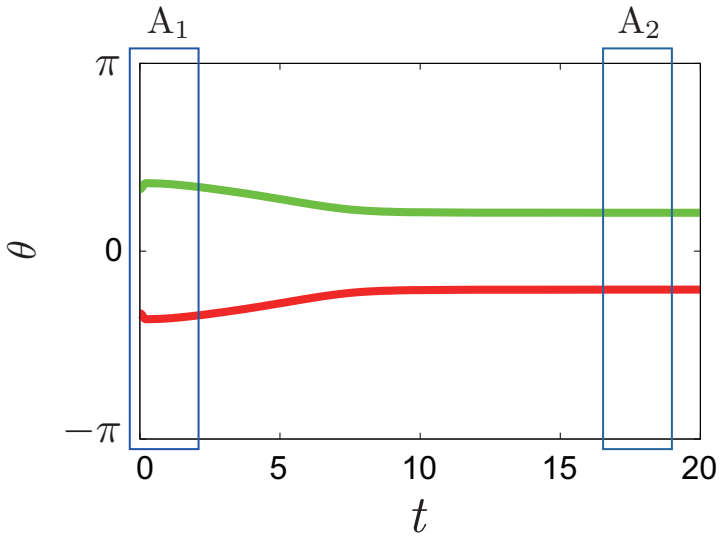

Figure 3.18: Trajectories of clustering dynamics for two droplets under a closed cover. Two droplets are merged within a short time.

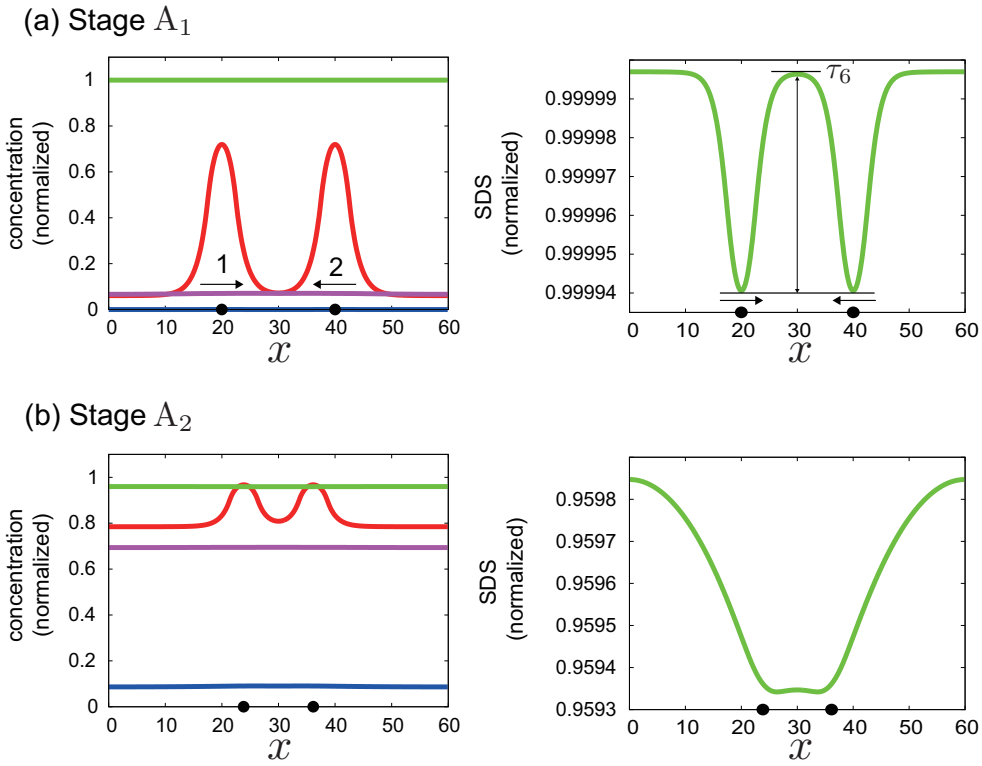

Figure 3.19: Concentration profiles of $\tilde{u}$, $\tilde{s}$, $\tilde{c}$, and $\tilde{w}$, normalized by $\tilde{u}_0$, $\tilde{s}_0$, $\tilde{c}_0$, and $\tilde{w}_0$, respectively, corresponding to stage A_1 and A_2, depicted in Fig. 3.18. Points on the horizontal axis indicate droplets 1 and 2. Two droplets move toward each other because of the peak, τ_6.

other and form a two-droplet cluster. The profile of concentrations in this process is shown in Fig. 3.19. We found that the peak between the two droplets is sufficiently high in the early stage A_1 so that the movement is negligible; as they slowly move towards each other, the peak gradually decreases and finally vanishes in the late-stage A_2, where the two droplets settle in a steady-state, confined by the valley of the SDS profile. Next, we study $N = 3$ with $\tilde{L}_x = 150$.

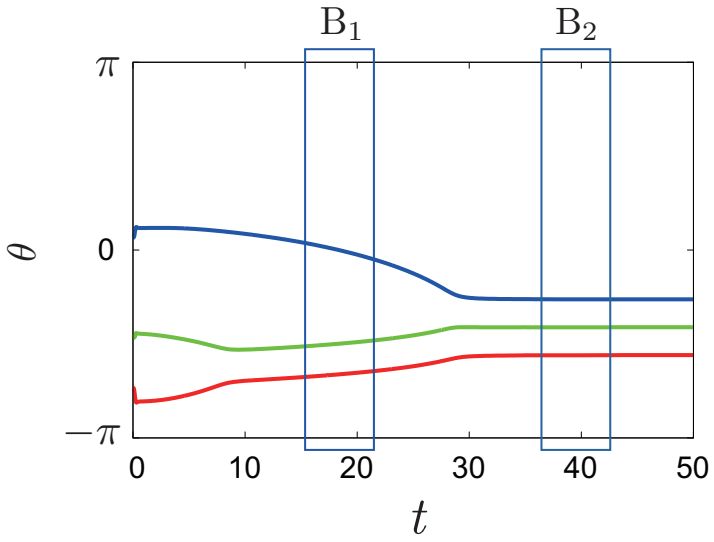

Figure 3.20: Trajectories of clustering dynamics for three droplets under a closed cover. Nearby two droplets are merged in the beginning, and all droplets are merged.

Figure 3.20 shows the trajectories of three droplets. The two nearby droplets form a small cluster first, which then merges with the third droplet to form a single cluster. From stage B_1 to B_2 in Fig. 3.20, both the two-droplet cluster and the single droplet move towards each other, but the single droplet moves faster. The profile of chemical concentrations in this process is shown in Fig. 3.21. Upon the transition from stage B_1 to B_2, the droplets move in such a way that the middle peak of the SDS profile (denoted by τ_7) vanishes. The leftward motion of droplet 3 is driven by the surface tension difference due to the peak difference $\tau_8 > \tau_7$ [Fig. 3.21]. The same surface tension difference drives the two-droplet cluster toward the right.

As ever a single droplet case, we also check our assumption that the profile of the SDS concentration can explain the motion. For this purpose, we apply to Eq. (3.31) for investigating change of each surface tension depending on the ES and SDS concentration. Likewise, a single droplet simulations, a single droplet ($\tilde{x}_c^3$) in Fig. 3.21 is calculated as Eq. (3.32). In particular, we calculate a difference of two-droplet cluster applying the left-hand side of left droplet ($\tilde{x}_c^1$) in Fig. 3.21 and the right-hand side of

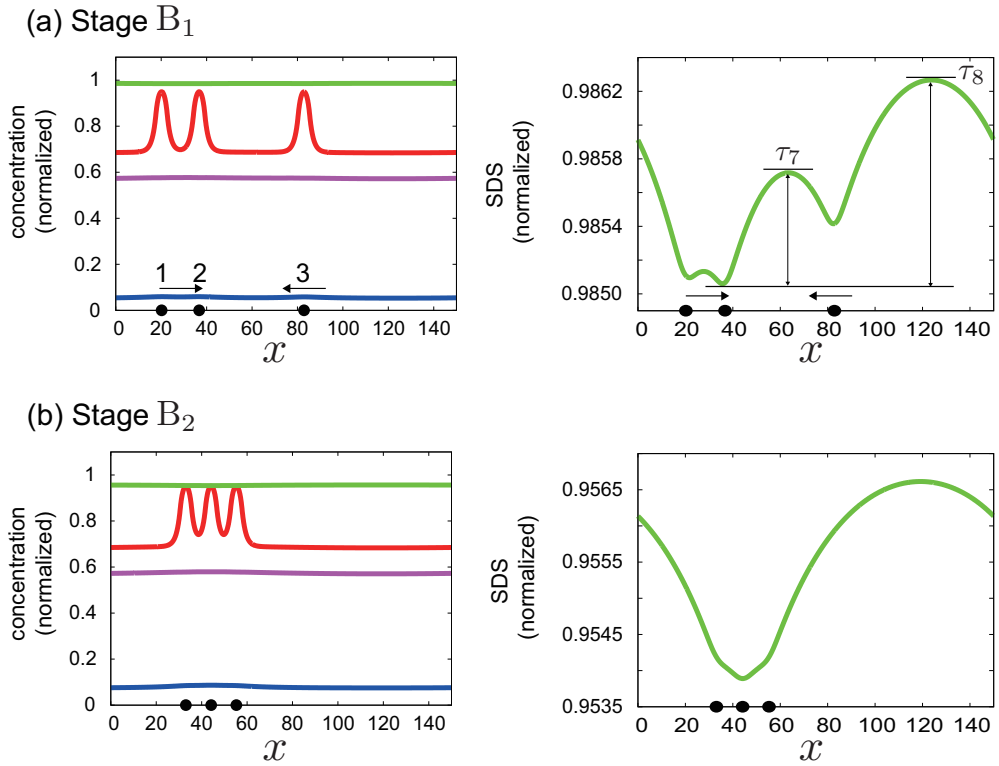

Figure 3.21: Concentration profiles of $\tilde{u}$, $\tilde{s}$, $\tilde{c}$, and $\tilde{w}$ for droplets, normalized by $\tilde{u}_0$, $\tilde{s}_0$, $\tilde{c}_0$, and $\tilde{w}_0$, respectively, corresponding to stage B_1 and B_2, depicted in Fig. 3.20. Points on the horizontal axis indicate droplets 1, 2, and 3. A small cluster and a single droplet are separated by the peak, τ_7, τ_8. They are merged as the peak, τ_7, is vanished.

right droplet ($\tilde{x}_c^2$) in Fig. 3.21, that is,

$$\begin{aligned}\Delta\tilde{g}(\tilde{u}) &= \tilde{g}\big(\tilde{u}(\tilde{t}, \tilde{x}_c^2 + \tilde{r})\big) - \tilde{g}\big(\tilde{u}(\tilde{t}, \tilde{x}_c^1 - \tilde{r})\big) \\ \Delta\tilde{h}(\tilde{s}) &= \tilde{h}\big(\tilde{s}(\tilde{t}, \tilde{x}_c^2 + \tilde{r})\big) - \tilde{h}\big(\tilde{s}(\tilde{t}, \tilde{x}_c^1 - \tilde{r})\big)\end{aligned} \tag{3.33}$$

Figure 3.22 shows $\tilde{g}(\tilde{u})$ and $\tilde{h}(\tilde{s})$ for the single droplet (a) and the two-droplet cluster (b), respectively, during stage B_1. In both cases, the effect of $\tilde{g}(\tilde{u})$ is negligible compared to that of $\tilde{h}(\tilde{s})$, suggesting that the dynamics is dominated by the profile of $\tilde{s}$. Note that, although the effect of $\tilde{h}(\tilde{s})$ dominates the surface tension variations, the effect of $\tilde{g}(\tilde{u})$ is still required for a single droplet to exhibit a self-propelled motion. To compare the surface tension difference containing both ES and SDS concentration, $\tilde{u}$ and $\tilde{s}$ of each position is substituted for the surface tension, $\tilde{\gamma}(\tilde{u}, \tilde{s})$, that is,

$$\Delta\tilde{\gamma}(\tilde{u}, \tilde{s}) = \tilde{\gamma}\big(\tilde{u}(\tilde{t}, \tilde{x}_c^i + \tilde{r}), \tilde{s}(\tilde{t}, \tilde{x}_c^i + \tilde{r})\big) - \tilde{\gamma}\big(\tilde{u}(\tilde{t}, \tilde{x}_c^i - \tilde{r}), \tilde{u}(\tilde{t}, \tilde{x}_c^i - \tilde{r})\big) \tag{3.34}$$

where $i = 1, 2, 3$. The surface tension difference of a two-droplet cluster is calculated in the order of droplets such as Eq. (3.33).

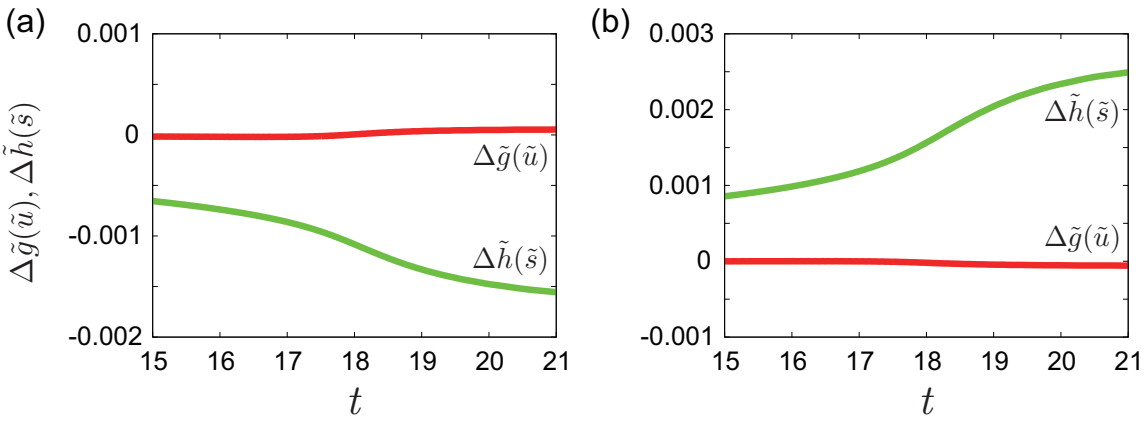

Figure 3.22: Contribution of $\tilde{u}$ and $\tilde{s}$ to the surface tension. See text for the definition of $\tilde{g}(\tilde{u})$ and $\tilde{h}(\tilde{s})$. $\Delta\tilde{g}(\tilde{u})$, $\Delta\tilde{h}(\tilde{s})$ is measured with the difference of the right and left side of a single droplet, as well as the right side of the right droplet and the left side of the left droplet of the small cluster. The variation of $\Delta\tilde{h}(\tilde{s})$ is larger than $\Delta\tilde{g}(\tilde{u})$. (a) The single droplet. (b) The two-droplet cluster.

Figure 3.23 show the surface tension difference $\Delta\tilde{\gamma}(\tilde{u}, \tilde{s})$. For the single droplet,

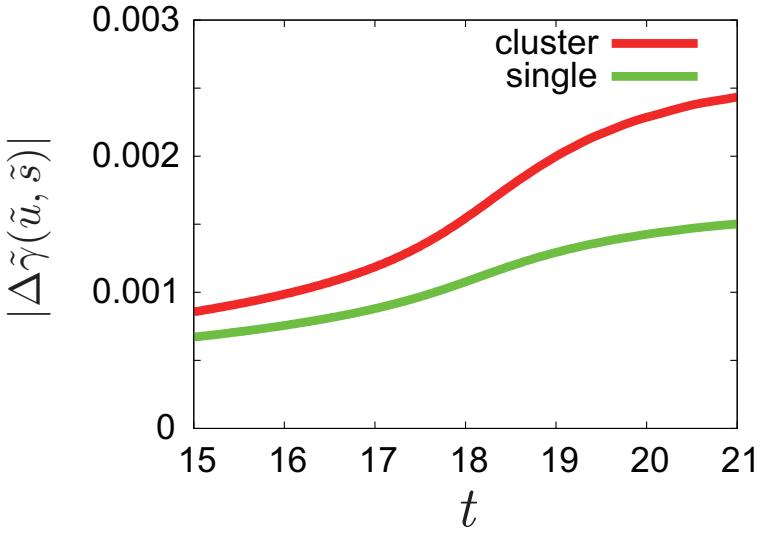

Figure 3.23: The surface tension difference, $\Delta\tilde{\gamma}(\tilde{u}, \tilde{s})$, for the single droplet (green) and the two-droplet cluster (red). The surface tension difference is measured with the difference of the right and left side of a single droplet, as well as the right side of the right droplet and the left side of the left droplet of the small cluster. The force of a small cluster is one-half of the curve due to the cluster size.

$\Delta\tilde{\gamma}(\tilde{u}, \tilde{s})$ is the difference of $\tilde{\gamma}$ between the right side and the left side of the droplet; For the two-droplet cluster, it is the difference between the right side of the right droplet

and the left side of the left droplet of the two. As shown in Fig. 3.23, the magnitudes of the force difference are comparable for both the single droplet and the two-droplet cluster, reflecting the fact that the peak-height difference of $\tilde{s}$ is precisely the same for both. This cluster size dependence is expected to become smaller as the cluster size increases since the concentration profiles of $\tilde{u}$ and $\tilde{s}$ change less and less when a new droplet is added to the cluster, which means that for large clusters, the force due to the surface tension difference weakly depends on the cluster size. On the other hand, the friction becomes larger when the cluster size becomes larger: because of the force balance between the droplets inside the cluster, the equation of motion for the center of mass X of the cluster of n_c droplets, with viscous force $\tilde{r}\eta\dot{X}$ and the surface tension difference $\tilde{r}\Delta\tilde{\gamma}$ is given by $n_c\eta\dot{X} = \Delta\tilde{\gamma}$, or the velocity is given by $\dot{X} = \Delta\tilde{\gamma}/(n_c\eta)$. In the case of Fig. 3.23, the force for the two-droplet cluster is one-half of the actual force shown by the curve, which is smaller than that of the single droplet. This result explains the fact that the single droplet moves faster than the two-droplet cluster, as shown in Fig. 3.20.

3.5.2.3 The effect of the cover on multiple droplet behavior

To understand the recovery activity, we show a simulation result of twenty droplets for the two-dimensional model when the cover is removed after the droplets form a cluster and reach a stationary state under a closed cover condition. As shown in Fig. 3.24, the cluster slowly expands (P_4 in Fig. 3.24), and then, each droplet restarts to oscillate (P_5). This result consistent with the experimental result (Fig. 2.6). This behavior is, also, understood from the concentration profiles. In the same manner with a closed cover, the each concentration of $\tilde{u}$, $\tilde{s}$, $\tilde{c}$, and $\tilde{w}$ is applied to investigate the mechanisms for P_4 and P_5. Likewise, the concentrations are calculated at $\tilde{y} = 0$ and normalized by $\tilde{u}_0$, $\tilde{s}_0$, $\tilde{c}_0$, and $\tilde{w}_0$, respectively. Points on the horizontal axis indicate twenty droplets.

Figure 3.25(a) shows a magnification of the trajectories that the one cluster spreads out in the beginning, depicted as P_4 in Fig. 3.24. As with the results of a single droplet under a removed cover, the concentrations of both $\tilde{u}$ and $\tilde{w}$ have converged zero, and the concentrations of $\tilde{c}$ also was decreased. In contrast, the SDS concentration slowly returns to $\tilde{s}_0$. Since high $\tilde{w}$ hinders evaporation of $\tilde{u}$ on the air/water interface, opening the cover induces evaporation of $\tilde{u}$ through the decrease of $\tilde{w}$, resulting in an enhanced concentration difference of $\tilde{u}$ around the droplet. Hence, after opening the cover, the surface tension difference due to $\tilde{u}$ recovers, and the droplet motion resumes. In the case of separation of both ends of the cluster, in the beginning, the spatial profile of SDS concentration at the air/water interface well shows the process. Namely, the

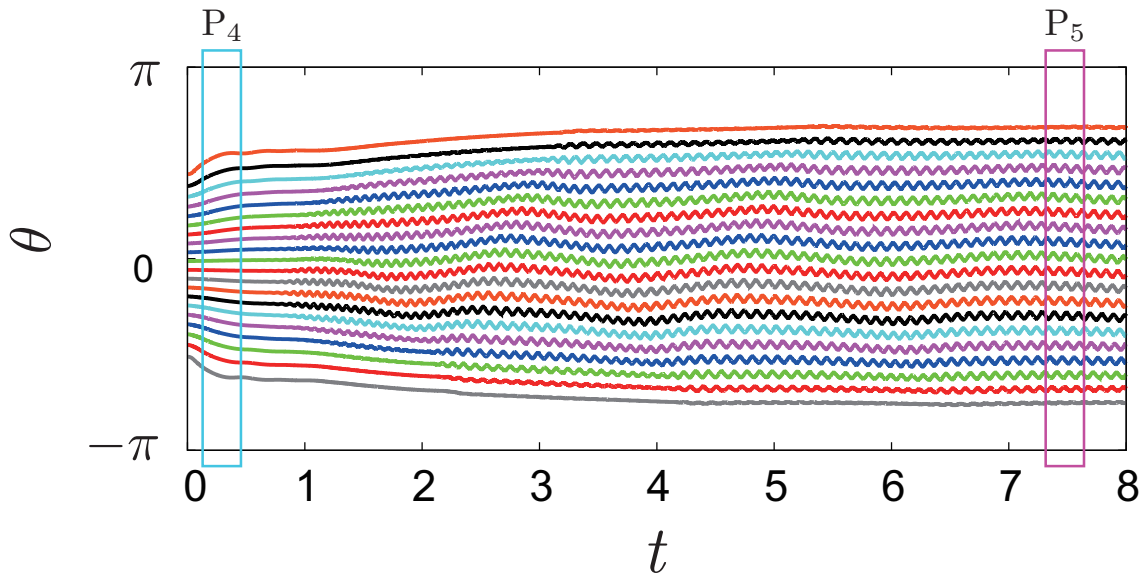

Figure 3.24: The trajectory of twenty droplets when the cover is removed, using as the initial condition the stationary state of the twenty droplets under a closed cover condition (Fig. 3.14).

smooth shape of the profile of SDS concentration sluggishly is converted into the rough shape, shown in Fig. 3.25(b).

Figure 3.26(a) shows a magnification of the trajectories that the oscillatory motion for droplets one cluster, depicted as P_5 in Fig. 3.24. In the oscillation for the droplets in the middle, the distance between the droplets at both ends keeps because of the peak between droplets. The droplets placed inside the cluster are oscillated continuously, shown in Fig. 3.26(b).

3.5.3 Comparison with the experimental results

The clustering process observed in the numerical simulation is qualitatively the same as the experimentally observed one for 20 droplets, as shown in Fig. 2.4. In particular, we can recognize two features of clustering both in the simulation and the experiment. One is the formation of sub-clusters that merge into larger and larger clusters; another is the tendency that, when several clusters exist, smaller clusters move faster.

Let us compare the timescale for a cluster formation in the simulation with that in the experiment. The droplet diameter is 2.5 mm in the experiment and $2\tilde{r} = 5$ in the simulation. Therefore, 1 unit length in the simulation corresponds to 0.5 mm. Therefore, the typical velocity of a single droplet in the experiment is approximately 500 mm/h, which can be measured from Fig. 2.6. In the simulation the typical velocity

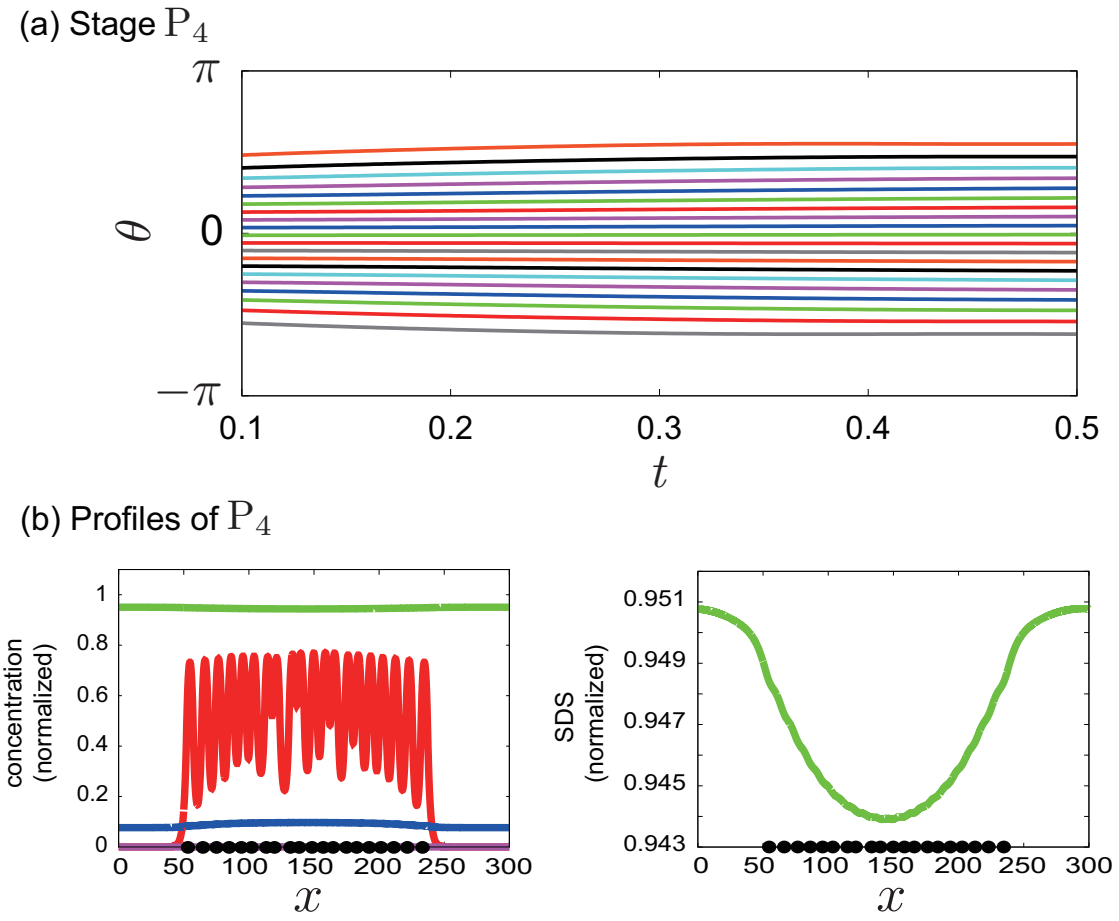

Figure 3.25: (a) The magnification for trajectories of the one cluster, depicted as P_4. (b) Profiles of $\tilde{u}$, $\tilde{s}$, $\tilde{c}$, and $\tilde{w}$ for droplets on the air/water interface during the clustering process P_4 in Fig. 3.24. The right side shows the magnification of the profile of $\tilde{s}/\tilde{s}_0$. The smooth shape is converted into the minute bumpy shape.

is estimated 40 unit length/unit time from Fig. 3.7. The length is compared as $\tilde{L}_x =$ 40 unit length = 20 mm, equating the two velocities from the experiment and the simulation yields 1 unit time = 0.04 h. Using this, we can estimate the timescale for the cluster formation. In the simulation, fig. 3.14 shows that the cluster is formed approximately at $\tilde{t} = 250$ unit time = 10 h, which is consistent with the experimental observation as shown in Fig. 2.4(a).

We next compared the first clustering time t_{cluster}, defined as the time to form a sub-cluster (mostly a two-droplet cluster) starting from an initial configuration for a given number of droplets n_{d}. We performed experiments for n_{d} =5, 6, 8, 10, 15, 20, 25, and 30. For each n_{d}, we repeated the experiment three times and measured the average and the standard deviation of t_{cluster}. Then we performed the corresponding

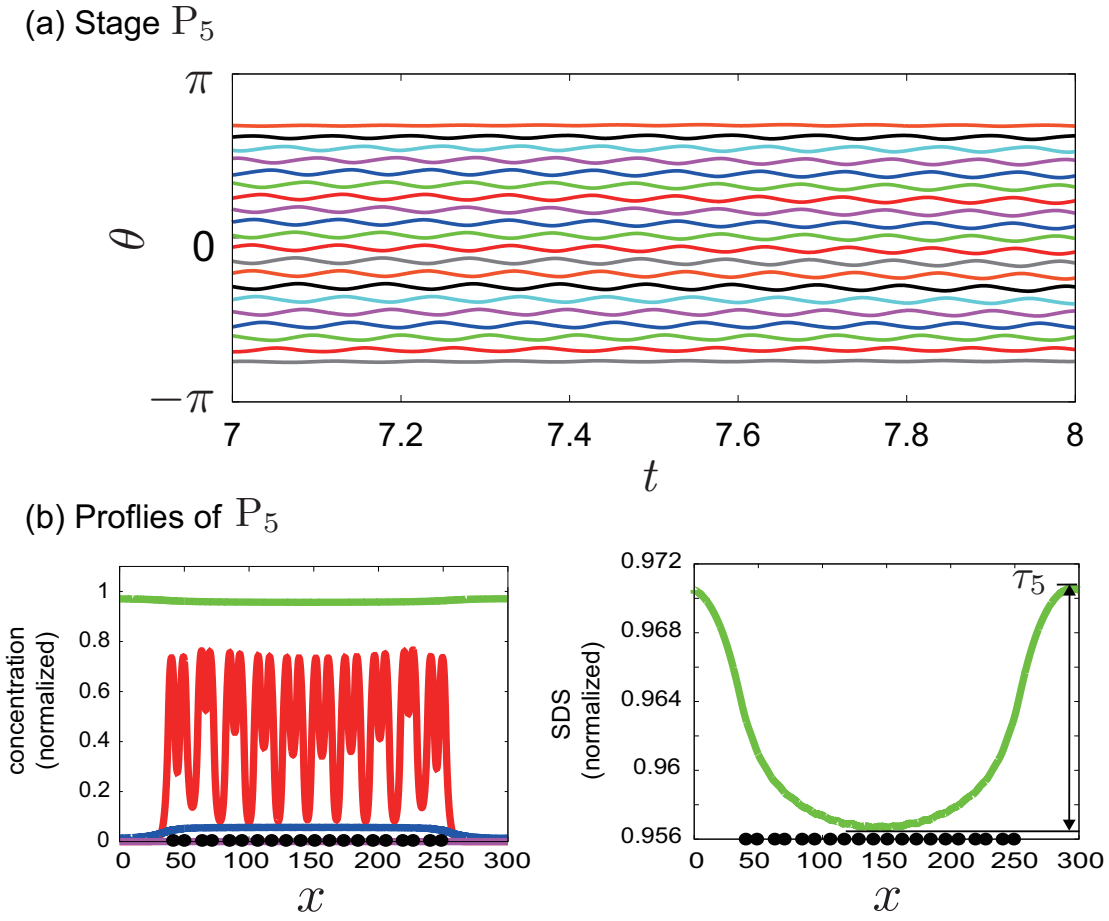

Figure 3.26: (a) The magnification for trajectories of the oscillatory motion for the droplets, depicted as P_5. (b) Profiles of $\tilde{u}$, $\tilde{s}$, $\tilde{c}$, and $\tilde{w}$ for droplets on the air/water interface during the clustering process P_5 in Fig. 3.24. The right side shows the magnification of the profile of $\tilde{s}/\tilde{s}_0$. The certain distance between the droplets at both ends is maintained because of the peak, τ_5.

numerical simulations for different n_d with three different initial random configurations of the droplets with $\tilde{L}_x = 500$, which is approximately equal to the experimental system size. The result is shown in Fig. 3.27. For n_d. We observed the same tendency in experiment and simulation in that t_cluster is a decreasing function of n_d. In particular, good agreement between experiment and simulation was found for $n_\mathrm{d} \geq 20$. Discrepancy becomes conspicuous, however, as n_d decreases. In particular, for $n_\mathrm{d} = 5$, we performed experiments four times and observed cluster formation only once in 15 hours of observation time, whereas numerical simulations always produced clusters.

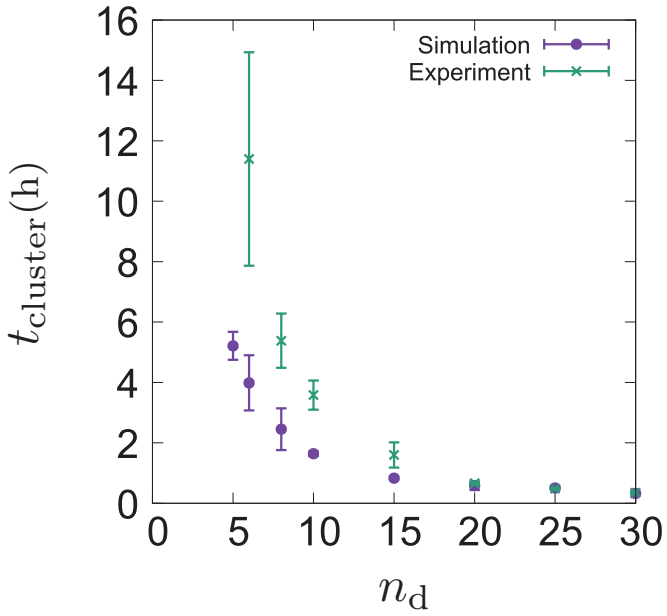

Figure 3.27: The first clustering time t_{cluster} as a function of the number of droplets n_{d} in simulation and experiment. For each n_{d}, Points are the average over three measurements. The error bars are the standard deviation. In the experiment, no clusters were observed for $n_{\mathrm{d}} = 5$ in three out of four trials.

4 The one-dimensional mathematical model

A mathematical model has been constructed as a two-dimensional model in which the depth of the channel and the air between the surface and the cover are considered with respect to s, c, and w. The clustering dynamics have to be applied as a three-dimensional system consisted of the two-dimensional surface. However, we considered it a one-dimensional surface because it is complicated to construct a three-dimensional mathematical model, in section 3. To construct a mathematical model considering a two-dimensional surface, as the first step, we derive a one-dimensional mathematical model from Eq. (3.1), as well as boundary conditions, Eq. (3.10), Eq. (3.11), Eq. (3.12), Eq. (3.13), Eq. (3.14), and Eq. (3.15).

4.1 Reduction to the one-dimensional equation

Although it faithfully dealt with the diffusion of bulk and air, and the surface was modeled as a one-dimensional space, a mathematical model has recently been reported considering the two-dimensional surface concentration field with only the SDS reservoir, that is, the bulk was treated as an infinite source of surfactants under a supply rate.

[52]. This means that we can have a one-layer system with the lower phase as bulk water by taking the limit $\delta \to 0$. We can also consider another one-layer system, which is the air phase between the surface and the cover, by taking the limit $L_y \to 0$. To neglect a two-dimensional system containing the depth and the air, we set an additional assumption as follows:

7. The depth of the upper phase, δ, and the heigh between the surface and cover, L_y, is sufficiently thin.

Applying assumption 7, the three equations, s, c, and w of Eq. (3.1) are able to be derived as a one-dimensional system containing each boundary condition at $y = -\delta$, $y = L_y$.

4.1.1 The equation of the SDS concentration

Due to diffusion in the upper phase, the equation of SDS concentration in Eq. (3.1) is expressed as a two-dimensional equation as follows:

$$\frac{\partial s}{\partial t} = d_s \Delta s \tag{4.1}$$

Integrate from $-\delta$ to 0 on both sides and take an average for Eq. (4.1),

$$\frac{1}{\delta}\int_{-\delta}^{0} \frac{\partial s}{\partial t}(t,x,y)dy = \frac{1}{\delta}\int_{-\delta}^{0} d_s \Delta s dy = \frac{1}{\delta}\int_{-\delta}^{0} d_s \left(\frac{\partial^2 s}{\partial x^2} + \frac{\partial^2 s}{\partial y^2}\right) dy. \tag{4.2}$$

From assumption 7, the left-hand side and right-hand side in Eq. (4.2) can be derived:

$$\frac{1}{\delta}\int_{-\delta}^{0} \frac{\partial s}{\partial t}(t,x,y)dy = \frac{\partial s}{\partial t}(t,x), \tag{4.3}$$

$$\frac{1}{\delta}\int_{-\delta}^{0} d_s \left(\frac{\partial^2 s}{\partial x^2}(t,x,y) + \frac{\partial^2 s}{\partial y^2}(t,x,y)\right) dy = d_s \frac{\partial^2 s}{\partial x^2}(t,x) + \frac{1}{\delta}\int_{-\delta}^{0} d_s \frac{\partial^2 s}{\partial y^2}(t,x,y)dy. \tag{4.4}$$

Applying Eq. (3.10) and Eq. (3.12), the second term of the right-hand side in Eq. (4.4) can be arranged in a one-dimensional equation by taking the limit $\delta \to 0$:

$$\frac{1}{\delta}\int_{-\delta}^{0} d_s \frac{\partial^2 s}{\partial y^2}(t,x,y)dy = \frac{d_s}{\delta}\left(\frac{\partial s}{\partial y}(t,x,0) - \frac{\partial s}{\partial y}(t,x,-\delta)\right) \tag{4.5}$$

$$= -\frac{k_1}{\delta}\left(1 - \frac{c(t,x)}{c_0}\right) f(s)u(t,x) + \frac{d_1}{\delta}(s_0 - s(t,x)). \tag{4.6}$$

Substituting Eq. (4.2) with Eq. (4.3) and Eq. (4.6), a one-dimensional equation is able to be derived as follows:

$$\frac{\partial s}{\partial t}(t,x) = d_s \frac{\partial^2 s}{\partial x^2}(t,x) - k_1^* \left(1 - \frac{c(t,x)}{c_0}\right) f(s)u + d_1^*(s_0 - s(t,x)). \tag{4.7}$$

where $k_1^* = \dfrac{k_1}{\delta}$, $d_1^* = \dfrac{d_1}{\delta}$.

4.1.2 The equation of the complex concentration

In such a way, the equation of SDS concentration, the equation of complex concentration can also be converted into a one-dimensional equation on the $[-\delta, 0]$ under assumption 7. The equation of complex concentration in Eq. (3.1) is expressed as a two-dimensional equation due to diffusion in the upper phase:

$$\frac{\partial c}{\partial t} = d_c \Delta c \tag{4.8}$$

Integrate on both sides and take an average for Eq. (4.8) ,

$$\frac{1}{\delta}\int_{-\delta}^{0} \frac{\partial s}{\partial t}(t,x,y)dy = \frac{1}{\delta}\int_{-\delta}^{0} d_c \Delta c dy = \frac{1}{\delta}\int_{-\delta}^{0} d_c \left(\frac{\partial^2 c}{\partial x^2} + \frac{\partial^2 c}{\partial y^2}\right) dy. \tag{4.9}$$

Then, the left-hand side and right-hand side in Eq. (4.9) is able to be derived:

$$\frac{1}{\delta}\int_{-\delta}^{0} \frac{\partial c}{\partial t}(t,x,y)dy = \frac{\partial c}{\partial t}(t,x), \tag{4.10}$$

$$\frac{1}{\delta}\int_{-\delta}^{0} d_c \left(\frac{\partial^2 c}{\partial x^2}(t,x,y) + \frac{\partial^2 c}{\partial y^2}(t,x,y)\right) dy = d_c \frac{\partial^2 c}{\partial x^2}(t,x) + \frac{1}{\delta}\int_{-\delta}^{0} d_c \frac{\partial^2 c}{\partial y^2}(t,x,y)dy. \tag{4.11}$$

Taking advantage of Eq. (3.11), as well as Eq. (3.13), the second term of right-hand side of Eq. (4.11) can be derived as a one-dimensional equation by taking the limit $\delta \to 0$:

$$\frac{1}{\delta}\int_{-\delta}^{0} d_c \frac{\partial^2 s}{\partial y^2}(t,x,y)dy = \frac{d_c}{\delta}\left(\frac{\partial c}{\partial y}(t,x,0) - \frac{\partial c}{\partial y}(t,x,-\delta)\right) \tag{4.12}$$

$$= \frac{k_1}{\delta}\left(1 - \frac{c(t,x)}{c_0}\right) f(s)u(t,x) - \frac{d_2}{\delta}c(t,x). \tag{4.13}$$

Replacing Eq. (4.9) with Eq. (4.10) and Eq. (4.13), the one-dimensional equation is able to be theoretically managed:

$$\frac{\partial c}{\partial t}(t,x) = d_c \frac{\partial^2 c}{\partial x^2}(t,x) + k_1^* \left(1 - \frac{c(t,x)}{c_0}\right) f(s)u(t,x) - d_2^* c(t,x) \tag{4.14}$$

where $k_1^* = \dfrac{k_1}{\delta}$, $d_2^* = \dfrac{d_2}{\delta}$.

4.1.3 The equation of the ES concentration in the air

As well, the equation for ES concentration in the air can be derived as a one-dimensional equation under assumption 7. Due to diffusion in the air phase, the

equation of ES concentration in the air in Eq. (3.1) is expressed as a two-dimensional equation:

$$\frac{\partial w}{\partial t} = d_w \Delta w \tag{4.15}$$

Since the region of the air phase is on the $[0, L_y]$, we integrate from 0 to L_y on both sides and take an average for Eq. (4.15),

$$\frac{1}{L_y}\int_0^{L_y} \frac{\partial w}{\partial t}(t,x,y)dy = \frac{1}{L_y}\int_0^{L_y} d_w \Delta w dy = \frac{1}{L_y}\int_0^{L_y} d_w \left(\frac{\partial^2 w}{\partial x^2} + \frac{\partial^2 w}{\partial y^2}\right) dy. \tag{4.16}$$

Then, we can arrange the left-hand side of Eq. (4.16) as below:

$$\frac{1}{L_y}\int_0^{L_y} \frac{\partial w}{\partial t}(t,x,y)dy = \frac{\partial w}{\partial t}(t,x) \tag{4.17}$$

As ever, the right-hand side of Eq. (4.16) can be derived as follows:

$$\begin{aligned}\frac{1}{L_y}\int_0^{L_y} d_w \left(\frac{\partial^2 w}{\partial x^2}(t,x,y) + \frac{\partial^2 w}{\partial y^2}(t,x,y)\right) dy = d_w \frac{\partial^2 w}{\partial x^2}(t,x) \\ + \frac{1}{L_y}\int_0^{L_y} d_w \frac{\partial^2 w}{\partial y^2}(t,x,y)dy.\end{aligned} \tag{4.18}$$

Also, Eq. 4.19 derive from the second term of right-hand side of Eq. (4.18).

$$\frac{1}{L_y}\int_0^{L_y} d_w \frac{\partial^2 w}{\partial y^2}(t,x,y)dy = \frac{d_w}{L_y}\left(\frac{\partial w}{\partial y}(t,x,L_y) - \frac{\partial w}{\partial y}(t,x,0)\right) \tag{4.19}$$

Eq. (4.20) by taking the limit $L_y \to 0$ is able to be derived by Eq. (3.14), as well as Eq.(3.15).

$$\begin{aligned}&\frac{d_w}{L_y}\left(\frac{\partial w}{\partial y}(t,x,L_y) - \frac{\partial w}{\partial y}(t,x,0)\right) = \\ &\sum_{i=1}^{N} \chi_i^- \frac{k_u}{L_y}\left(1 - \frac{w(t,x)}{w_0}\right) u(t,x) - \frac{k_a}{L_y} w(t,x)\left(1 - \frac{u(t,x)}{u_0}\right) - \frac{k_w}{L_y} w(t,x)\end{aligned} \tag{4.20}$$

In the end, Eq. (4.21) can be obtained as substituting Eq. (4.16) with Eq. (4.17) and Eq. (4.20).

$$\begin{aligned}\frac{\partial w}{\partial t}(t,x) = d_w \frac{\partial^2 w}{\partial x^2}(t,x) + \sum_{i=1}^{N} \chi_i^- k_u^* \left(1 - \frac{w(t,x)}{w_0}\right) u(t,x) \\ - k_a^* w(t,x)\left(1 - \frac{u(t,x)}{u_0}\right) - k_w^* w(t,x)\end{aligned} \tag{4.21}$$

where $k_u^* = \dfrac{k_u}{L_y}$, $k_a^* = \dfrac{k_a}{L_y}$, and $k_w^* = \dfrac{k_w}{L_y}$.

4.2 The one-dimensional model system

We have shown the process theoretically derived the one-dimensional equations in subsection 4.1. This simplifies our two-dimensional model Eq. (3.1) so that it can be applied to one-dimensional cases, which is a step before develop the mathematical model taking into account two-dimensional surface concentration fields. Substituting Eq.(3.1) to Eq.(4.7), Eq.(4.14), and Eq.(4.21), eventually, a two-dimensional model system is able to be converted into a one-dimensional model system as follows:

$$
\begin{cases}
\dfrac{dx_c^i}{dt} = \dfrac{1}{\eta}\left[\gamma\Big(u(t,x_c^i+r), s(t,x_c^i+r)\Big) - \gamma\Big(u(t,x_c^i-r), s(t,x_c^i-r)\Big)\right] \\
\qquad\quad + \dfrac{1}{2\eta r}\left[F_0(x_c^i, x_c^{i-1}) - F_0(x_c^i, x_c^{i+1})\right], \\
\dfrac{\partial u}{\partial t} = d_u\dfrac{\partial^2 u}{\partial x^2} + \displaystyle\sum_{i=1}^{N}\chi_i^+(x)k_0\left(1-\frac{u(t,x)}{u_0}\right) + k_a^* w(t,x)\left(1-\frac{u(t,x)}{u_0}\right) \\
\qquad\quad - \displaystyle\sum_{i=1}^{N}\chi_i^-(x)k_u^*\left(1-\frac{w(t,x)}{w_0}\right)u(t,x) - k_{us}^*\left(1-\frac{c(t,x)}{c_0}\right)f(s(t,x))u(t,x), \\
\dfrac{\partial s}{\partial t} = d_s\dfrac{\partial^2 s}{\partial x^2}(t,x) - k_{us}^*\left(1-\frac{c(t,x)}{c_0}\right)u(t,x)f(s(t,x)) + d_1^*(s_0 - s(t,x)), \\
\dfrac{\partial c}{\partial t} = d_c\dfrac{\partial^2 c}{\partial x^2}(t,x) + k_{us}^*\left(1-\frac{c(t,x)}{c_0}\right)u(t,x)f(s(t,x)) - d_2^* c(t,x), \\
\dfrac{\partial w}{\partial t} = d_w\dfrac{\partial^2 w}{\partial x^2}(t,x) + \displaystyle\sum_{i=1}^{N}\chi_i^-(x)k_u^*\left(1-\frac{w(t,x)}{w_0}\right)u(t,x) \\
\qquad\quad - k_a^*\left(1-\frac{u(t,x)}{u_0}\right)w(t,x) - k_w^* w(t,x).
\end{cases}
\tag{4.22}
$$

where $k_u^* = \dfrac{k_u}{L_y}$, $k_a^* = \dfrac{k_a}{L_y}$, $k_w^* = \dfrac{k_w}{L_y}$, $k_{us}^* = \dfrac{k_{us}}{\delta}$, $d_1^* = \dfrac{d_1}{\delta}$ and $d_2^* = \dfrac{d_2}{\delta}$.

By converting into a one-dimensional model, the diffusion in the vertical direction can be ignored, but the boundary conditions need to be considered because the horizontal direction is still valid. In the one-dimensional model, the periodic boundary conditions, such as boundary conditions in the horizontal direction of the two-dimensional model, are set horizontally since we only affect the vertical direction, δ, L_y, in the two-dimensional model.

$$u(t,0) = u(t,L_x), \quad \frac{\partial u}{\partial x}(t,0) = \frac{\partial u}{\partial x}(t,L_x), \tag{4.23}$$

$$s(t,0) = s(t,L_x), \quad \frac{\partial s}{\partial x}(t,0) = \frac{\partial s}{\partial x}(t,L_x), \tag{4.24}$$

$$c(t,0) = c(t,L_x), \quad \frac{\partial c}{\partial x}(t,0) = \frac{\partial c}{\partial x}(t,L_x), \tag{4.25}$$

$$w(t,0) = w(t,L_x), \quad \frac{\partial w}{\partial x}(t,0) = \frac{\partial w}{\partial x}(t,L_x). \tag{4.26}$$

where $x \in (0, L_x)$.

The initial conditions are set similar to the two-dimensional model because of the identical setting with the two-dimensional model:

$$\begin{aligned} u(0,x) = 0, \quad s(0,x) = s_0, \\ c(0,x) = 0, \quad w(0,x) = 0. \end{aligned} \tag{4.27}$$

4.3 Nondimensionalization

As ever the two-dimensional model, the one-dimensional model can be interpreted by non-dimensionalized parameters. The index $*$ has been applied to the one-dimensional model to distinguish a two-dimensional model. Using parameters r^*, w_0^*, k_{us}^*, and η^*, we can construct the scales of the radius, the time, the mass, and the number of molecules as r^*, $1/k_{us}^*$, $\eta^* r^*/k_{us}^*$, and $w_0^* r^{*2}$, respectively. We, therefore, nondimensional the variables and the following nondimensionalized parameters:

$$\tilde{t}^* = k_{us}^* t^*, \quad \tilde{x}^* = \frac{1}{r^*} x^*, \quad \tilde{x}_c^{*i}(t) = \frac{1}{r^*} x_c^{*i}(t),$$

$$\tilde{u}^*(t^*, x^*) = \frac{1}{w_0^*} u^*(t^*, x^*), \quad \tilde{c}^*(t^*, x^*) = \frac{1}{w_0^*} c^*(t^*, x^*),$$

$$\tilde{s}^*(t^*, x^*) = \frac{1}{w_0^*} s^*(t^*, x^*), \quad \tilde{w}^*(t^*, x^*) = \frac{1}{w_0^*} w(t^*, x^*),$$

$$\tilde{L}_x^* = \frac{1}{r^*} L_x^*, \quad \tilde{u}_0^* = \frac{1}{w_0^*} u_0^*, \quad \tilde{s}_0^* = \frac{1}{w_0^*} s_0^*, \quad \tilde{w}_0^* = \frac{1}{w_0^*} w_0^*,$$

$$\tilde{d}_u^* = \frac{1}{k_{us}^* r^{*2}} d_u^*, \quad \tilde{d}_s^* = \frac{1}{k_{us}^* r^{*2}} d_s^*, \quad \tilde{d}_c^* = \frac{1}{k_{us}^* r^{*2}} d_c^*, \quad \tilde{d}_w^* = \frac{1}{k_{us}^* r^{*2}} d_w^*, \quad \tilde{d}_1^* = \frac{1}{k_{us}^*} d_1^*,$$

$$\tilde{d}_2^* = \frac{1}{k_{us}^*} d_2^*, \quad \tilde{k}_0^* = \frac{1}{w_0^* k_{us}^*} k_0^*, \quad \tilde{k}_u^* = \frac{1}{k_{us}^*} k_u^*, \quad \tilde{k}_a^* = \frac{1}{k_{us}^*} k_a^*, \quad \tilde{k}_w^* = \frac{1}{k_{us}^*} k_w^*,$$

$$\tilde{\alpha}^* = \alpha^*, \quad \tilde{\beta}^* = \frac{1}{w_0^*} \beta^*, \quad \tilde{a}^* = \frac{1}{w_0^*} a^*, \quad \tilde{b}^* = \frac{1}{w_0^*} b^*,$$

$$\tilde{\gamma_0^*} = \frac{1}{\eta^* k_{us}^* r^*} \gamma_0^*, \quad \tilde{\gamma_1^*} = \frac{1}{\eta^* k_{us}^* r^*} \gamma_1^*, \quad \tilde{\xi_0}^* = \frac{1}{\eta^* k_{us}^* r^{*2}} \xi_0^*.$$

Substituting above nondimensionalized parameters, equivalently, all variables and parameters in Eq. (4.22) can be rewritten with $r^* = w_0^* = k_{us}^* = \eta^* = 1$:

$$
\begin{cases}
\dfrac{d\tilde{x}_c^{*i}}{d\tilde{t}^*} = \Big[\tilde{\gamma}^*\Big(\tilde{u}^*(\tilde{t}^*, \tilde{x}_c^{*i}+1), \tilde{s}^*(\tilde{t}^*, \tilde{x}_c^{*i}+1)\Big) - \tilde{\gamma}^*\Big(\tilde{u}^*(\tilde{t}^*, \tilde{x}_c^{*i}-1), \tilde{s}^*(\tilde{t}^*, \tilde{x}_c^{*i}-1)\Big)\Big] \\
\qquad + \dfrac{1}{2}\Big[\tilde{F}_0^*(\tilde{x}_c^{*i}, \tilde{x}_c^{*i-1}) - \tilde{F}_0^*(\tilde{x}_c^{*i}, \tilde{x}_c^{*i+1})\Big], \\
\dfrac{\partial \tilde{u}^*}{\partial \tilde{t}^*} = \tilde{d}_u^* \dfrac{\partial^2 \tilde{u}^*}{\partial \tilde{x}^{*2}} + \displaystyle\sum_{i=1}^{N} \tilde{\chi}_i^{*+}(\tilde{x}^*)\tilde{k}_0^*\left(1 - \dfrac{\tilde{u}^*(\tilde{t}^*, \tilde{x}^*)}{\tilde{u}_0^*}\right) + \tilde{k}_a^*\tilde{w}^*(\tilde{t}^*, \tilde{x}^*)\left(1 - \dfrac{\tilde{u}^*(\tilde{t}^*, \tilde{x}^*)}{\tilde{u}_0^*}\right) \\
\qquad - \displaystyle\sum_{i=1}^{N} \tilde{\chi}_i^{*-}(\tilde{x}^*)\tilde{k}_u^*\big(1 - \tilde{w}^*(\tilde{t}^*, \tilde{x}^*)\big)\tilde{u}^*(\tilde{t}^*, \tilde{x}^*) \\
\qquad - \left(1 - \dfrac{\tilde{c}^*(\tilde{t}^*, \tilde{x}^*)}{\tilde{c}_0^*}\right)\tilde{f}^*\big(\tilde{s}^*(\tilde{t}^*, \tilde{x}^*)\big)\tilde{u}^*(\tilde{t}^*, \tilde{x}^*), \\
\dfrac{\partial \tilde{s}^*}{\partial \tilde{t}^*} = \tilde{d}_s^* \dfrac{\partial^2 \tilde{s}^*}{\partial \tilde{x}^{*2}}(\tilde{t}^*, \tilde{x}^*) - \left(1 - \dfrac{\tilde{c}^*(\tilde{t}^*, \tilde{x}^*)}{\tilde{c}_0^*}\right)\tilde{u}^*(\tilde{t}^*, \tilde{x}^*)\tilde{f}^*\big(\tilde{s}^*(\tilde{t}^*, \tilde{x}^*)\big) \\
\qquad + \tilde{d}_1^*\big(\tilde{s}_0^* - \tilde{s}^*(\tilde{t}^*, \tilde{x}^*)\big), \\
\dfrac{\partial \tilde{c}^*}{\partial \tilde{t}^*} = \tilde{d}_c^* \dfrac{\partial^2 \tilde{c}^*}{\partial \tilde{x}^{*2}}(\tilde{t}^*, \tilde{x}^*) + \left(1 - \dfrac{\tilde{c}^*(\tilde{t}^*, \tilde{x}^*)}{\tilde{c}_0^*}\right)\tilde{u}^*(\tilde{t}^*, \tilde{x}^*)\tilde{f}^*\big(\tilde{s}^*(\tilde{t}^*, \tilde{x}^*)\big) - \tilde{d}_2^*\tilde{c}^*(\tilde{t}^*, \tilde{x}^*), \\
\dfrac{\partial \tilde{w}^*}{\partial \tilde{t}^*} = \tilde{d}_w^* \dfrac{\partial^2 \tilde{w}^*}{\partial \tilde{x}^{*2}}(\tilde{t}^*, \tilde{x}^*) + \displaystyle\sum_{i=1}^{N} \tilde{\chi}_i^{*-}(\tilde{x}^*)\tilde{k}_u^*\big(1 - \tilde{w}^*(\tilde{t}^*, \tilde{x}^*)\big)\tilde{u}^*(\tilde{t}^*, \tilde{x}^*) \\
\qquad - \tilde{k}_a^*\left(1 - \dfrac{\tilde{u}^*(\tilde{t}^*, \tilde{x}^*)}{\tilde{u}_0^*}\right)\tilde{w}^*(\tilde{t}^*, \tilde{x}^*) - \tilde{k}_w^*\tilde{w}^*(\tilde{t}, \tilde{x}^*).
\end{cases}
\tag{4.28}
$$

Converting into a one-dimensional model has not a direct influence on Eq. (3.2), Eq. (3.3), Eq. (3.4), Eq. (3.5), and Eq. (4.27) in the two-dimensional model but, these equations can be expressed by nondimensionalized parameters:

$$
\tilde{\gamma}^*(\tilde{u}^*, \tilde{s}^*) = \frac{1}{2}\left(\frac{\tilde{a}^{*2}}{\tilde{a}^{*2} + \tilde{u}^{*2}} + \frac{\tilde{b}^*}{\tilde{b}^* + \tilde{s}^*}\right)(\tilde{\gamma}_0^* - \tilde{\gamma}_1^*) + \tilde{\gamma}_1^*, \tag{4.29}
$$

$$
\tilde{F}_0^*(\tilde{x}_c^{*i}, \tilde{x}_c^{*j}) = \begin{cases} \tilde{\xi}_0^*\big(2 - |\tilde{x}_c^{*i} - \tilde{x}_c^{*j}|\big), & |\tilde{x}_c^{*i} - \tilde{x}_c^{*j}| \le 2, \\ 0, & |\tilde{x}_c^{*i} - \tilde{x}_c^{*j}| > 2, \end{cases} \tag{4.30}
$$

$$
\tilde{\chi}_i^{*+}(\tilde{x}^*) = \begin{cases} 1, & |\tilde{x}^* - \tilde{x}_c^{*i}| \le 1, \\ 0, & |\tilde{x}^* - \tilde{x}_c^{*i}| > 1, \end{cases} \qquad \tilde{\chi}_i^{*-}(\tilde{x}^*) = 1 - \tilde{\chi}_i^{*+}(\tilde{x}^*), \tag{4.31}
$$

$$\tilde{f}^*(\tilde{s}^*) = \frac{\tilde{\alpha}^*\tilde{s}^*}{\tilde{\beta}^* + \tilde{s}^*}. \tag{4.32}$$

$$\begin{aligned} \tilde{u}^*(0,\tilde{x}^*) = 0, \quad \tilde{s}^*(0,\tilde{x}^*) = \tilde{s}_0^*, \\ \tilde{c}^*(0,\tilde{x}^*) = 0, \quad \tilde{w}^*(0,\tilde{x}^*) = 0. \end{aligned} \tag{4.33}$$

4.4 Numerical results

In this section, we show the different simulation results for the one-dimensional model. A single droplet to find proper parameters set, and the multiple droplets to reproduce the clustering dynamics are simulated with a periodic boundary condition. Likewise a two-dimensional model, we find suitable parameters set and reproduce the clustering dynamics of both a single droplet and multiple droplets through the simulations, and the effect of the cover is expressed by changing the parameter $\tilde{k}_w^*$; a zero-flux, $\tilde{k}_w^* = 0$, with a cover and a non-zero flux, $\tilde{k}_w^* > 0$, without a cover. The horizontal length $\tilde{L}_x^*$ is varied depending on the number of droplets N.

4.4.1 A single droplet

To investigate the motions of a single droplet and clustering dynamics of multiple droplets based on the one-dimensional model, we apply a periodic boundary condition as ever a two-dimensional model. We opt for the parameters for the benefit of simulating for the one-dimensional model as below: $\tilde{d}_u^* = 48.0$, $\tilde{d}_s^* = 9.6$, $\tilde{d}_c^* = 1.6$, $\tilde{d}_w^* = 1.6 \times 10^7$, $\tilde{d}_1^* = 0.8$, $\tilde{d}_2^* = 5.0$, $\tilde{u}_0^* = 0.006$, $\tilde{c}_0^* = 0.02$ $\tilde{k}_0^* = 0.9$, $\tilde{k}_u^* = 80.0$, $\tilde{k}_a^* = 1.0$, $\tilde{k}_w^{*+} = 1.0 \times 10^4$, $\tilde{\alpha}^* = 1.0$, $\tilde{\beta}^* = 0.002$, $\tilde{\gamma}_0^* = 4.0 \times 10^4$, $\tilde{\gamma}_1^* = 0.0$, $\tilde{a}^* = 0.06$, $\tilde{b}^* = 0.06$, $\tilde{\xi}_0^* = 6.08 \times 10^3$. As the initial conditions, we set $\tilde{u}^*(0,\tilde{x}^*) = 0$, $\tilde{s}^*(0,\tilde{x}^*) = \tilde{s}_0^*$, $\tilde{c}^*(0,\tilde{x}^*) = 0$, and $\tilde{w}^*(0,\tilde{x}^*) = 0$. These parameters have been chosen in such a way that the consistent motion as in [43] and result of a two-dimensional model, depicted as Fig. 3.4 is qualitatively reproduced for a single droplet. Furthermore, as the initial conditions we set $\tilde{u}^*(0,\tilde{x}^*) = 0$, $\tilde{s}^*(0,\tilde{x}^*) = \tilde{s}_0^*$, $\tilde{c}^*(0,\tilde{x}^*) = 0$, and $\tilde{w}^*(0,\tilde{x}^*) = 0$. Alike the simulation results of a two-dimensional model, we discern the normalized concentration profiles as each color, shown in Fig. 3.3.

4.4.1.1 Phase diagram

As the first step in order to find suitable parameters set, it is necessary to confirm the phase diagram for a one-dimensional model. Thus, we study the transition of a single

droplet depending on the initial SDS concentration $\tilde{s}_0^*$ within the range $[0.06, 0.15]$ under an open cover condition ($\tilde{k}_w^* = \tilde{k}_w^{*+}$). We set $\tilde{L}_x^* = 16$.

The stationary, oscillatory, and rotating state of a single droplet identical to the chemical experiment results (Fig. 1.9, Fig. 1.10, Fig. 1.11), previous result in [43], and a two-dimensional model (Fig. 3.4) are confirmed, as shown in Fig. 4.1(a). The meaning of $\Delta\theta$, T consistent with the indication, in paragraph 3.5.1.1. The appearance of the period as increasing $\tilde{L}_x^*$ is consistent with the result of the two-dimensional model, as shown in Fig. 4.1(b).

The oscillation period increases as $\tilde{s}_0^*$ in the oscillatory regime. In the rotating state, the period of rotation only slightly decreases. Note that the period of rotation depends on the system size $\tilde{L}_x^*$.

As a result of the simulation results of a two-dimensional model, we have found that the droplet oscillates irregularly before shifting from an oscillatory state to a rotating state. Therefore, we choose $\tilde{s}_0^* = 0.12$, which corresponds to the oscillatory regime in Fig. 4.1(a).

4.4.1.2 The effect of the cover on a single droplet behavior

The effect of the cover is considered in the same as the way a two-dimensional model: without a cover ($\tilde{k}_w^* = \tilde{k}_w^{*+}$); with a cover ($\tilde{k}_w^* = 0$). As the first step for showing the effect of the cover, we simulate the case without a cover until the droplet reaches the stable oscillation state. Then, the droplet oscillates consistently when the cover is open, as shown in Fig. 4.2.

Figure 4.3 shows the concentration profiles for $\tilde{u}^*$, $\tilde{s}^*$, $\tilde{c}^*$, and $\tilde{w}^*$ according to droplet position, $\tilde{x}_c^*$ under an open cover condition. The remarkable point is that the profile of the ES concentration is the asymmetry when the droplet moves, as ever the simulation results of the two-dimensional model.

To simulate the case of a closed cover, we set the initial data as the last data of $\tilde{u}^*$, $\tilde{s}^*$, $\tilde{c}^*$, and $\tilde{w}^*$, and the droplet position $\tilde{x}_c^*$ under an open cover condition. Unlike the simulation results of the two-dimensional model, the droplet does not quickly reach the stationary state. The droplet continuously oscillates in the beginning, and the amplitude is gradually decreased. Eventually, the droplet reaches the stationary state, as shown in Fig. 4.4.

Figure 4.5 shows the concentration profiles for $\tilde{u}^*$, $\tilde{s}^*$, $\tilde{c}^*$, and $\tilde{w}^*$ according to droplet position under a closed cover.

Each concentration increases or decreases , similar to the concentration results of the two-dimensional model: the complex and the ES concentration on the air/water

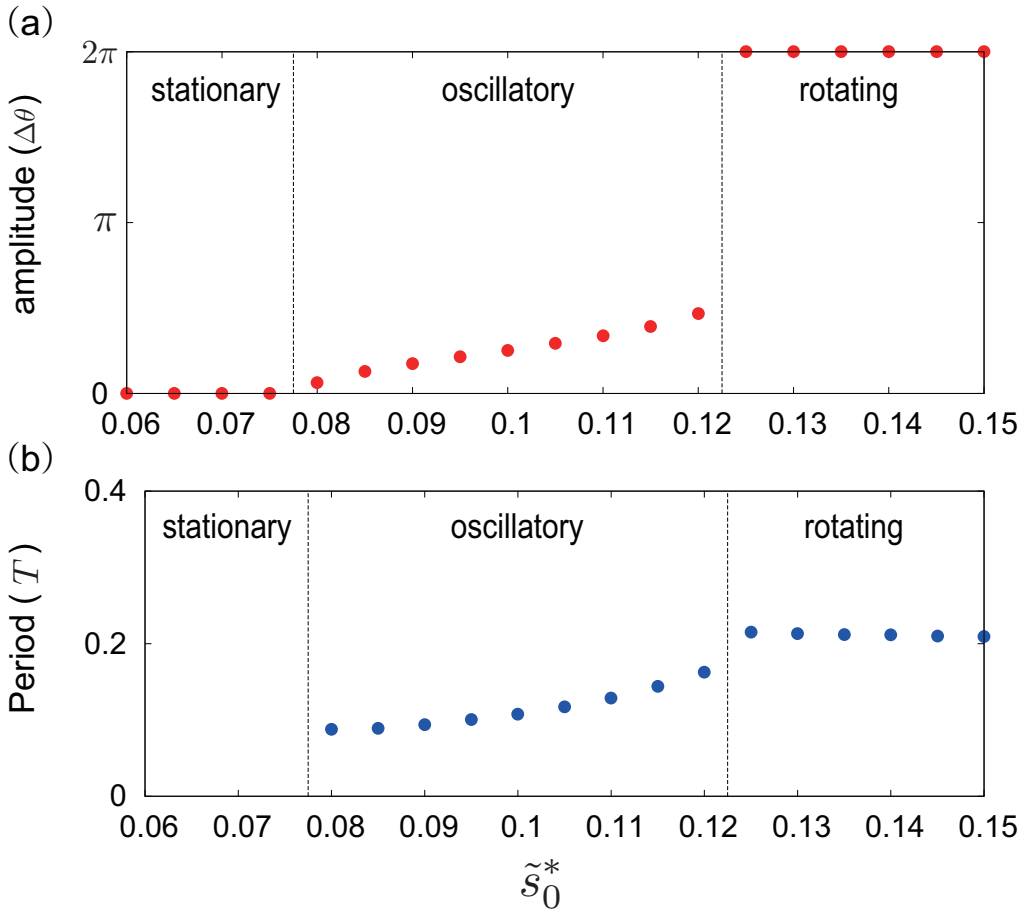

Figure 4.1: Three distinct states of a single droplet observed by changing the initial SDS concentration $\tilde{s}_0^*$, under the open cover condition. (a) The vertical axis represents the amplitude of motion measured in terms of azimuth: in the oscillating motion, it is defined by the distance covered by one oscillation multiplied by $2\pi/\tilde{L}_x^*$. The amplitude is 2π for the rotating motion. (b) The oscillation period depending on $\tilde{s}_0^*$.

interface, and in the air, increases: the SDS concentration slightly decreases. Since the motion change of the one-dimensional and two-dimensional model is different, the changes in the concentration profiles are also differently shown. The ES concentration both in the air and on the air/water interface increases slowly, but simultaneously, the droplet's amplitude starts to decrease unnoticed. When these ES concentrations increase by one-third, the amplitude of droplet conspicuously decrease. Finally, the ES concentration immaculately maintains the symmetric profile when the droplet reaches the stationary state. As ever in the case of a closed cover, we consider the last data of a closed cover as the initial data of a removed cover condition. Under a removed cover condition, the droplet recovers the activity and keeps the regular oscillatory motion,

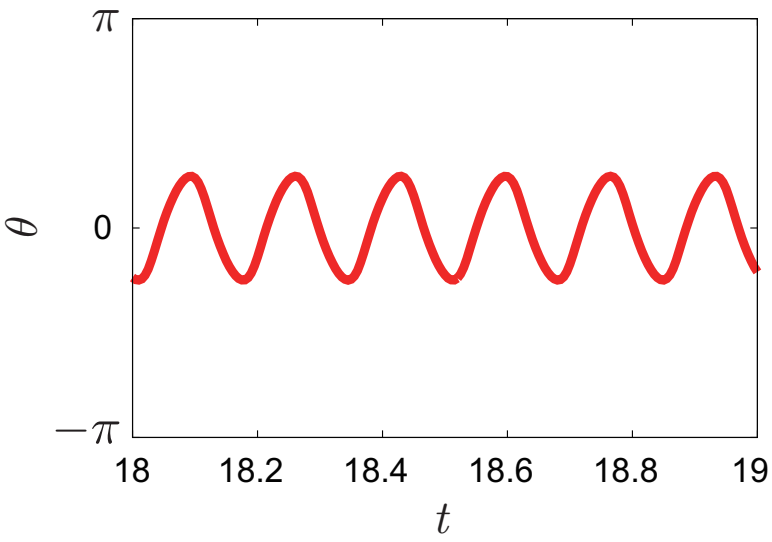

Figure 4.2: Trajectory of a single droplet when an open cover, $\tilde{k}_w^* = 1.0 \times 10^4$. The droplet oscillates repeatedly.

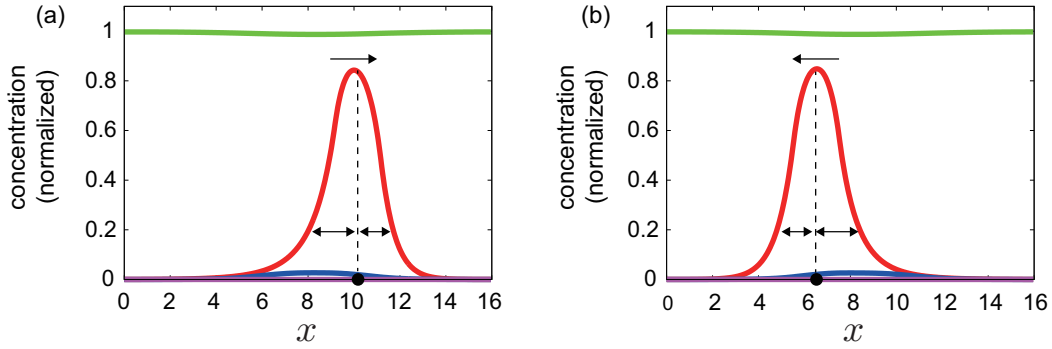

Figure 4.3: Concentration profiles of a single droplet under an open cover condition. The asymmetric profile of the ES concentration. (a) Move toward the right side. (b) Move toward the left side.

shown in Fig. 4.6.

Figure 4.7 shows the concentration profiles for $\tilde{u}^*$, $\tilde{s}^*$, $\tilde{c}^*$, and $\tilde{w}^*$ according to droplet position, $\tilde{x}_c^*$ under a removed cover.

The ES concentration at the surface and in the air is decreased. As the SDS concentration increases, conversely, the complex concentration decreases. In addition, a symmetric ES concentration is converted into the asymmetric profile when the droplet restarts to move. In the same way as the two-dimensional model, time $\tilde{t}^*$ is reset to zero after each change of the cover state. This transition of the droplet motion considerably coincides with the experimental result (Fig. 2.2). As ever the explanation of oscillatory motion for a two-dimensional model, in paragraph 3.5.1.3, we found the symmetric

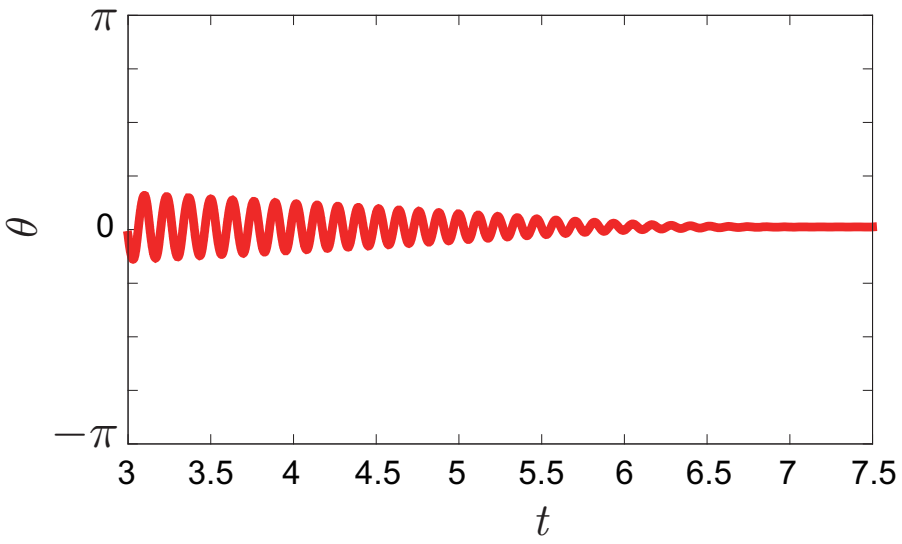

Figure 4.4: Trajectory for a single droplet when a closed cover, $\tilde{k}_w^* = 0$. The state of transition from an oscillatory state to a stationary state. As initial data, the last data of $\tilde{u}^*$, $\tilde{s}^*$, $\tilde{c}^*$, and $\tilde{w}^*$, and droplet position $\tilde{x}_c^*$ for the case of a closed cover are taken advantage of.

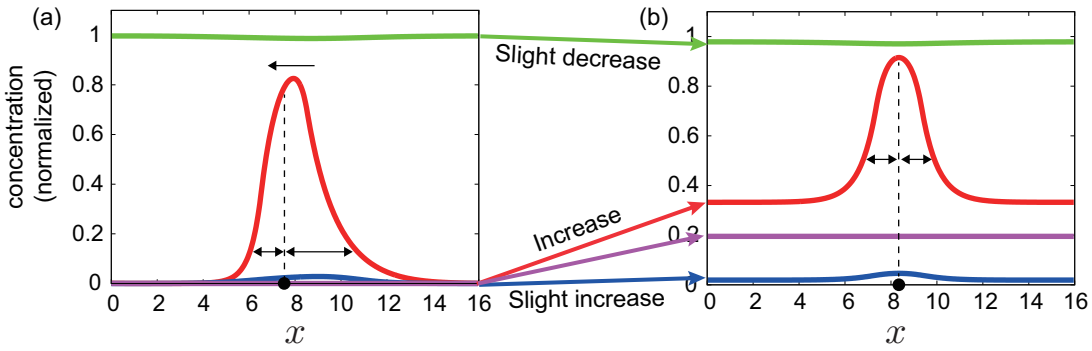

Figure 4.5: Concentration profiles of a single droplet under a closed cover. The asymmetric profile of the ES concentration is converted into the symmetric profiles. (a) Move toward the left side. (b) Reach the stationary state.

or asymmetric profiles of ES concentration in the results of a one-dimensional model. These results provide confidence that a one-dimensional model can successfully describe the motions of a single droplet.

4.4.2 Multiple droplets

We confirmed that the one-dimensional model is also able to qualitatively regenerate the transient motion of a single droplet. In this section, we reproduce the clustering dynamics of twenty droplets to verify the possibility of qualitative regeneration based on the one-dimensional model.

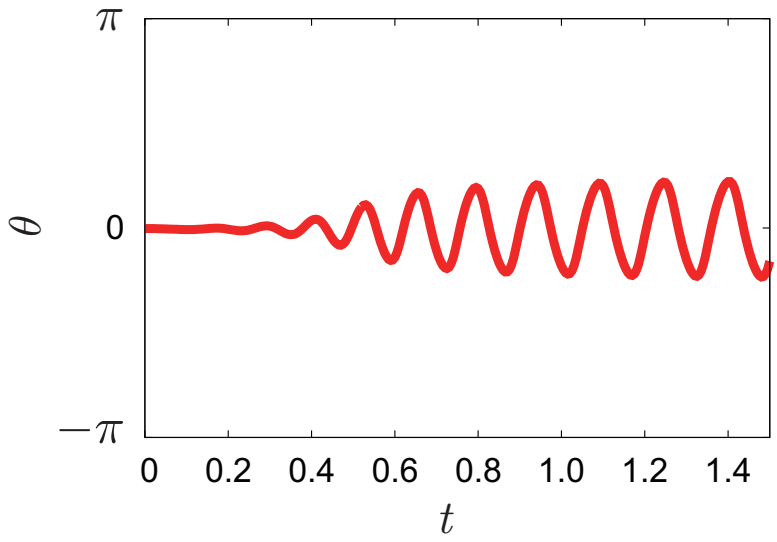

Figure 4.6: Trajectory of a single droplet when a removed cover, $\tilde{k}_w^* = 1 \times 10^4$. The recovery of the droplet and the regular oscillation. As initial data, the last data of $\tilde{u}^*$, $\tilde{s}^*$, $\tilde{c}^*$, and $\tilde{w}^*$, and droplet position, $\tilde{x}_c^*$ in the a closed cover are applied.

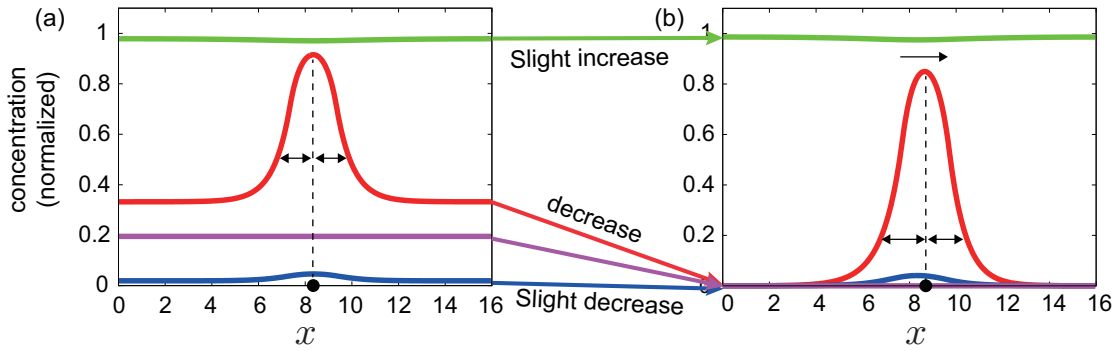

Figure 4.7: Concentration profiles of a single droplet when a removed cover. The conversion of the ES concentration from the symmetry to asymmetry. (a) The stationary state. (b) Move toward the right side.

4.4.2.1 Twenty droplets

For the simulation of twenty droplets, we set $\tilde{L}_x^* = 120$. At first, we take into account the case of a closed cover. Then, likewise the two-dimensional model, we ascertained that the clustering dynamics could also be explained by the one-dimensional model. We found the following clustering process: In the early stage, all droplets enthusiastically oscillate for a while, and the amplitudes of their oscillations are gradually decreased, similar to the single droplet under a closed cover (Fig. 4.8). After stopping the oscillation of the droplets, the nearby droplets approach each other to form four clusters

(depicted as P_1 in Fig. 4.9). The smallest cluster is absorbed into the larger one within a relatively short time (depicted as P_2 in Fig. 4.9). Then, the relatively small two clusters merge into one cluster after sufficient time, and finally, the two clusters keep the stationary state continuously (depicted as P_3 in Fig. 4.10). This clustering process of the one-dimensional model is partially the same as the experimentally observed one for twenty droplets, as shown in Fig. 2.4.

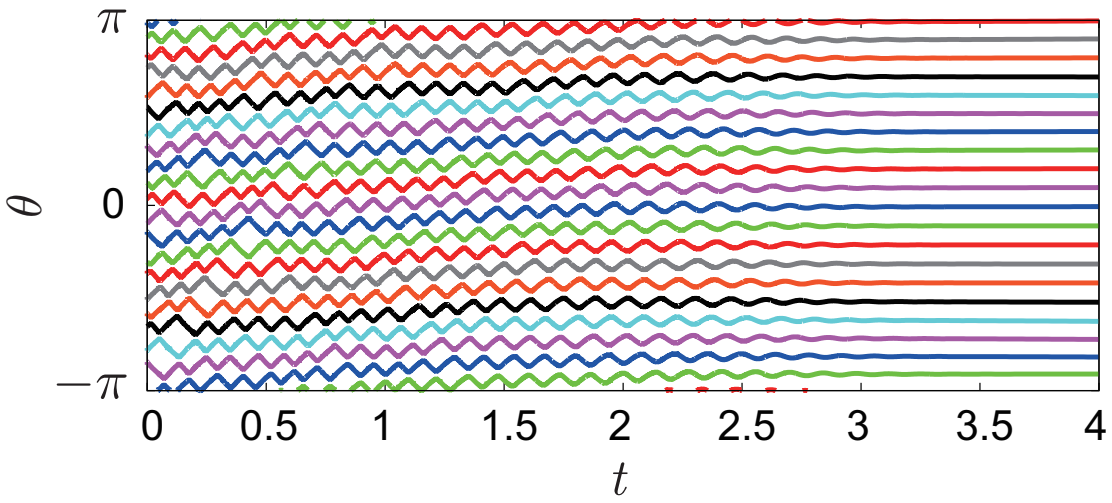

Figure 4.8: Trajectories of twenty droplets under a closed cover in the beginning. All droplets oscillates, and stops the oscillatory motion.

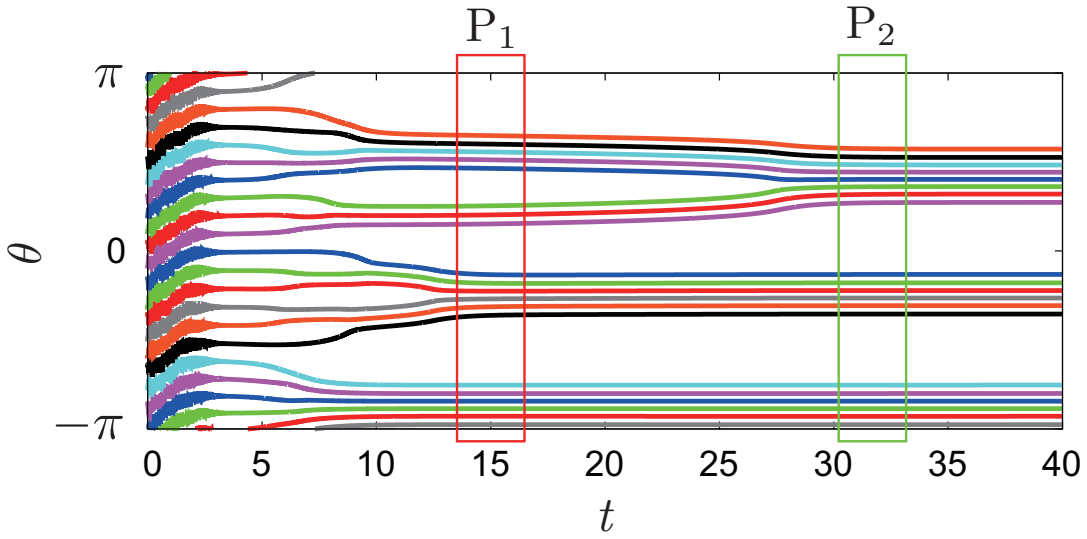

Figure 4.9: Trajectories of twenty droplets under a closed cover in the middle. Two distinct stages of clustering process are depicted as P_1 (four clusters) and P_2 (three clusters).

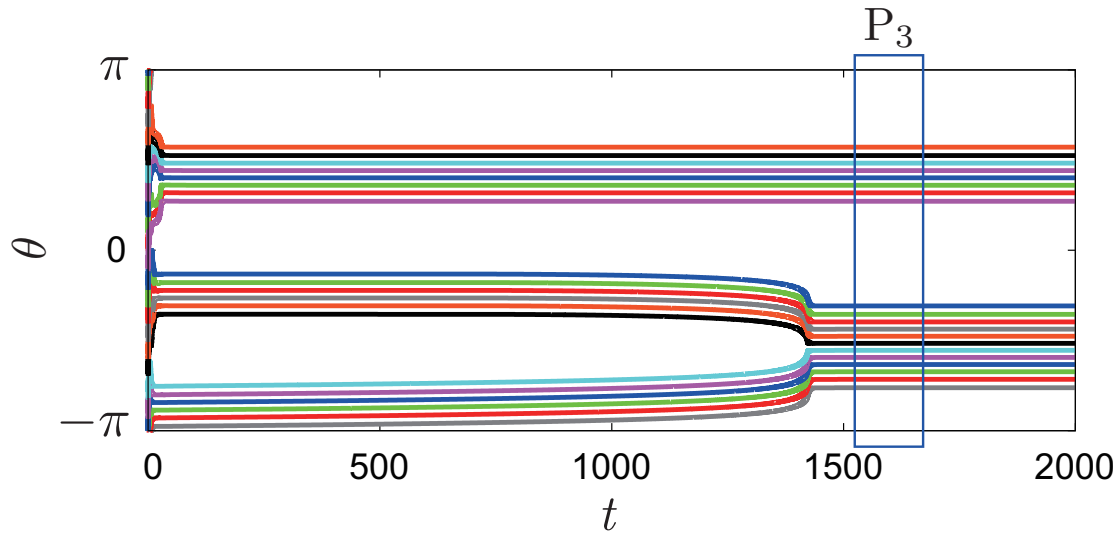

Figure 4.10: Trajectories of twenty droplets under a closed cover in the end. The merging stage of the relatively small clusters is depicted as P_3.

As ever the two-dimensional model, the profile of SDS concentration well shows the clustering process. To investigate the mechanisms for P_1, P_2, and P_3, we take into account the each concentration of $\tilde{u}^*$, $\tilde{s}^*$, $\tilde{c}^*$, and $\tilde{w}^*$. Points on the horizontal axis indicate twenty droplets. The four clusters, which are moving to form the clustering motion among the four clusters are labeled as c_1, c_2, and c_3.

Figure 4.11(a) magnify the trajectories that form the four clusters in the beginning, depicted as P_1 in Fig. 4.9. As ever the results of a single droplet under a closed cover, the concentrations of $\tilde{u}^*$, $\tilde{w}^*$ increase, and the concentrations of $\tilde{c}^*$ slightly increased. In the case of cluster formation, in the beginning, the spatial profile of SDS concentration well shows that the droplets inside the largest cluster, c_1, among denoted the clusters approach each other because of the peak, τ_4. The other two clusters are merged into a low-concentration regions of $\tilde{s}^*$, separated by three peaks, τ_1, τ_2, and τ_3. The three peak heights between clusters induce the surface tension difference, as shown in Fig. 4.11(b). Since the effect of the SDS concentration through the explanation of clustering dynamics for a two-dimensional model, in paragraph 3.5.2.2, the transition from one stage to the next can be explained by the SDS concentration difference, which approximately corresponds to the peak height difference. $\tau_2 > \tau_1$ means that the surface tension is smaller on the right side of cluster c_2 than on the left side, so that c_2 moves toward the right. Analogously, $\tau_3 > \tau_1$ implies that the cluster, c_3, moves leftward. Because of $\tau_2 - \tau_1 < \tau_3 - \tau_1$, c_2 moves faster than c_3, resulting in c_2 absorbed into c_3; and since SDS molecules are consumed due to the complex formation mostly near

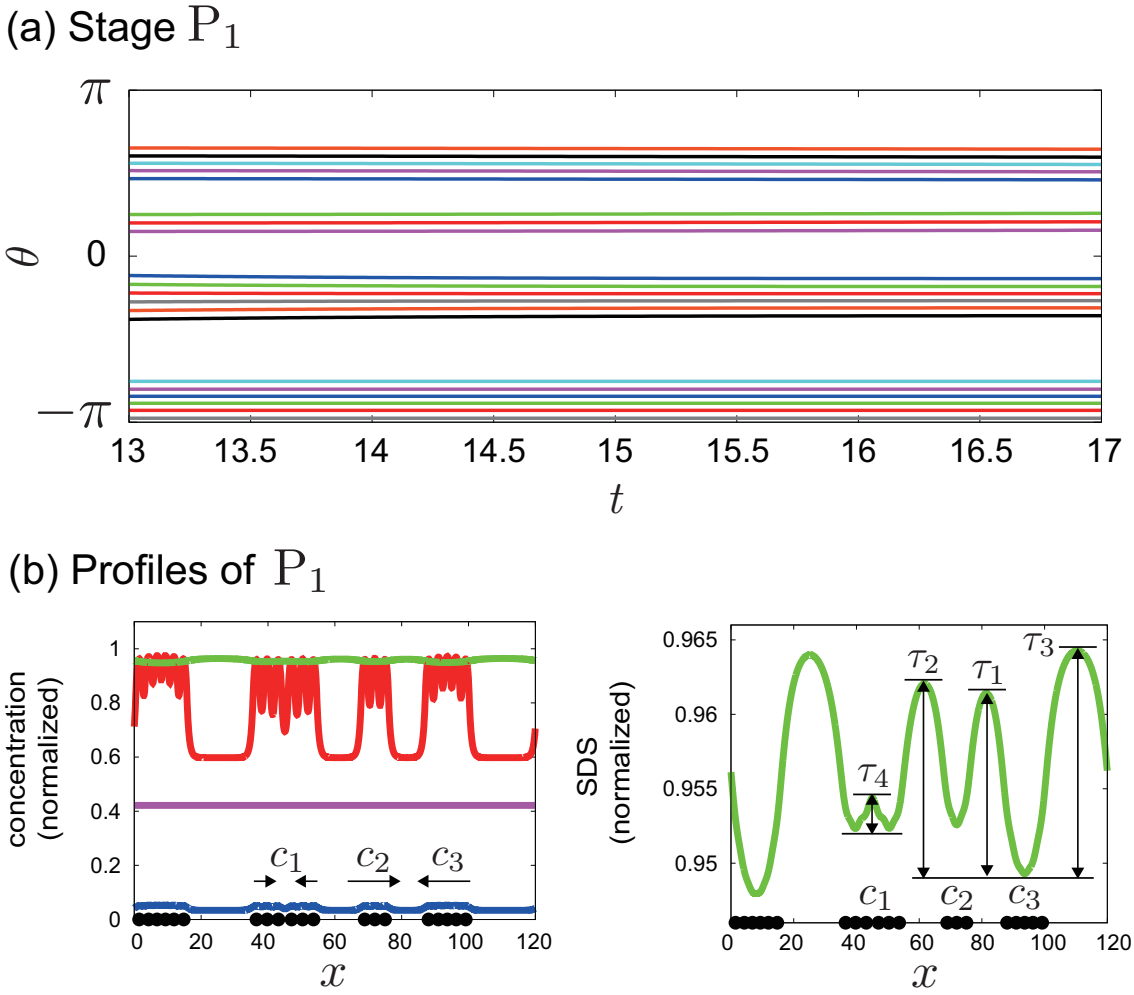

Figure 4.11: (a) The magnification for trajectories of the four clusters, depicted as P_1. (b) Profiles of $\tilde{u}^*$, $\tilde{s}^*$, $\tilde{c}^*$, and $\tilde{w}^*$ for droplets during the clustering process P_1 in Fig. **??**. The right side shows the magnification of the profile of $\tilde{s}^*/\tilde{s}_0^*$. The peak height of $\tilde{s}^*/\tilde{s}_0^*$ from the minimum is denoted by τ_1, τ_2, τ_3, and τ_4.

the droplet regions, the peak, τ_1 that had separated two clusters disappears when they merge. Our intuition that clustering dynamics is caused by SDS concentration from simulation results of the two-dimensional model has also been confirmed in simulation results of the one-dimensional model.

Figure 4.12(a) enlarge the trajectories that form the three clusters in the middle, depicted as P_2 in Fig. 4.9. The concentrations of $\tilde{u}^*$, $\tilde{w}^*$ were prominently increased higher than P_1 stage but, the concentrations of $\tilde{c}^*$, $\tilde{s}^*$ change to the point where they are not noticeable. Especially, $\tilde{u}^*$ reached almost the ES saturation on the surface. As the two clusters, c_2, c_3 have merged, one of the peak heights, τ_1 has vanished, and the combined cluster maintains the symmetry, concurrently, the motion of droplets in the

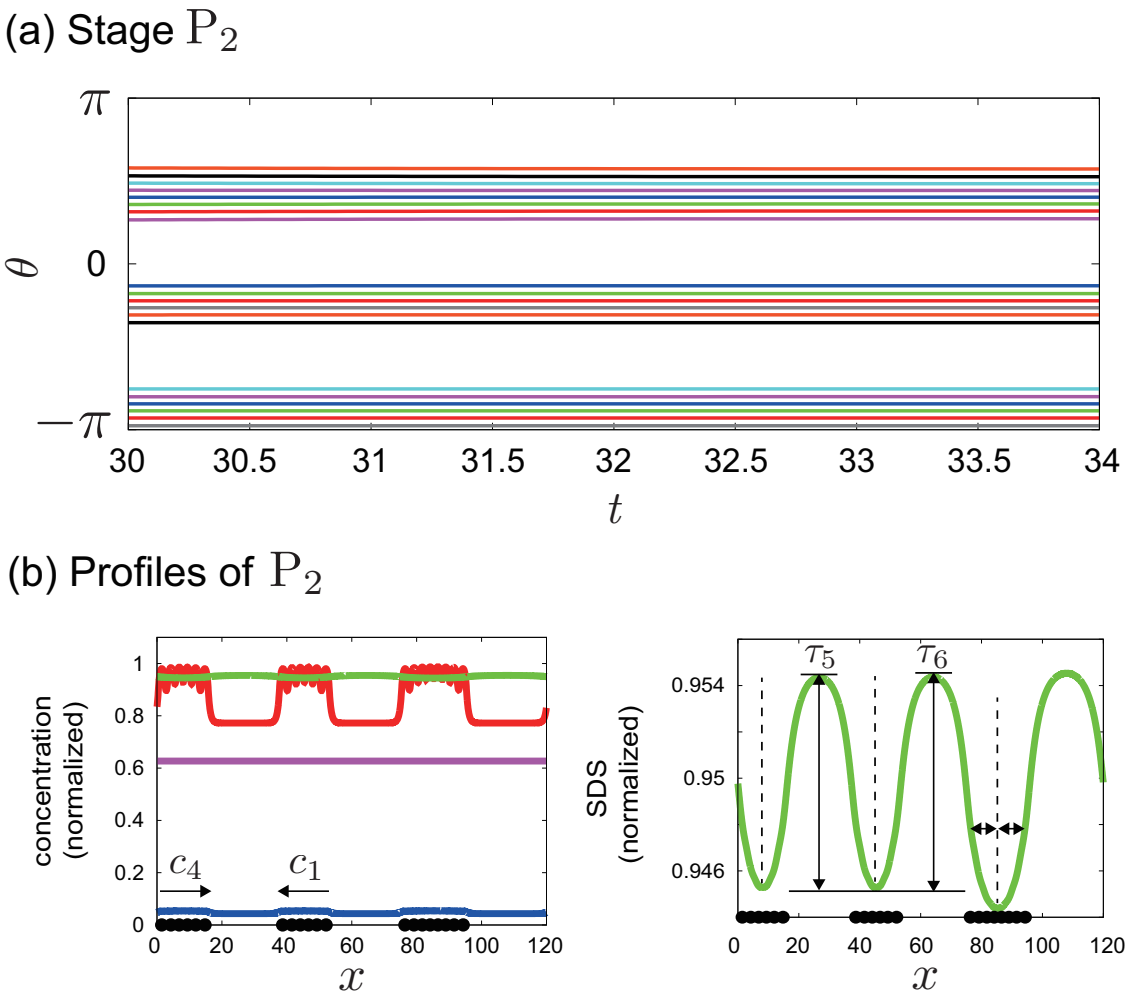

Figure 4.12: (a) The magnification for trajectories of the three clusters, depicted as P_2. (b) Profiles of $\tilde{u}^*$, $\tilde{s}^*$, $\tilde{c}^*$, and $\tilde{w}^*$ for droplets during the clustering process P_2 in Fig. **??**. The right side shows the magnification of the profile of $\tilde{s}^*/\tilde{s}_0^*$. The peak height of $\tilde{s}^*/\tilde{s}_0^*$ from the minimum is denoted by τ_5, τ_6.

combined cluster reaches the stationary state. Also, the peak, τ_4 have disappeared after the droplets in the cluster, c_1, gather. Then, the SDS concentration around the cluster is a smooth one, as well as symmetry. In the spatial profile of SDS concentration, the three clusters are separated by three peaks but, solely, the relatively small two clusters, c_1, c_4, sluggishly attract each other because the two peak, τ_5, τ_6, nearly equal, as shown in Fig. 4.12(b). Likewise, $\tau_6 > \tau_5$ means that the surface tension difference occurs on both sides, but due to the minute surface tension difference, it takes a long time to merge into the larger cluster.

Figure 4.13(a) is the magnification of the trajectories that form the larger two clusters in the end, depicted as P_3 in Fig. 4.10. As the height of the peak, τ_5, decreases,

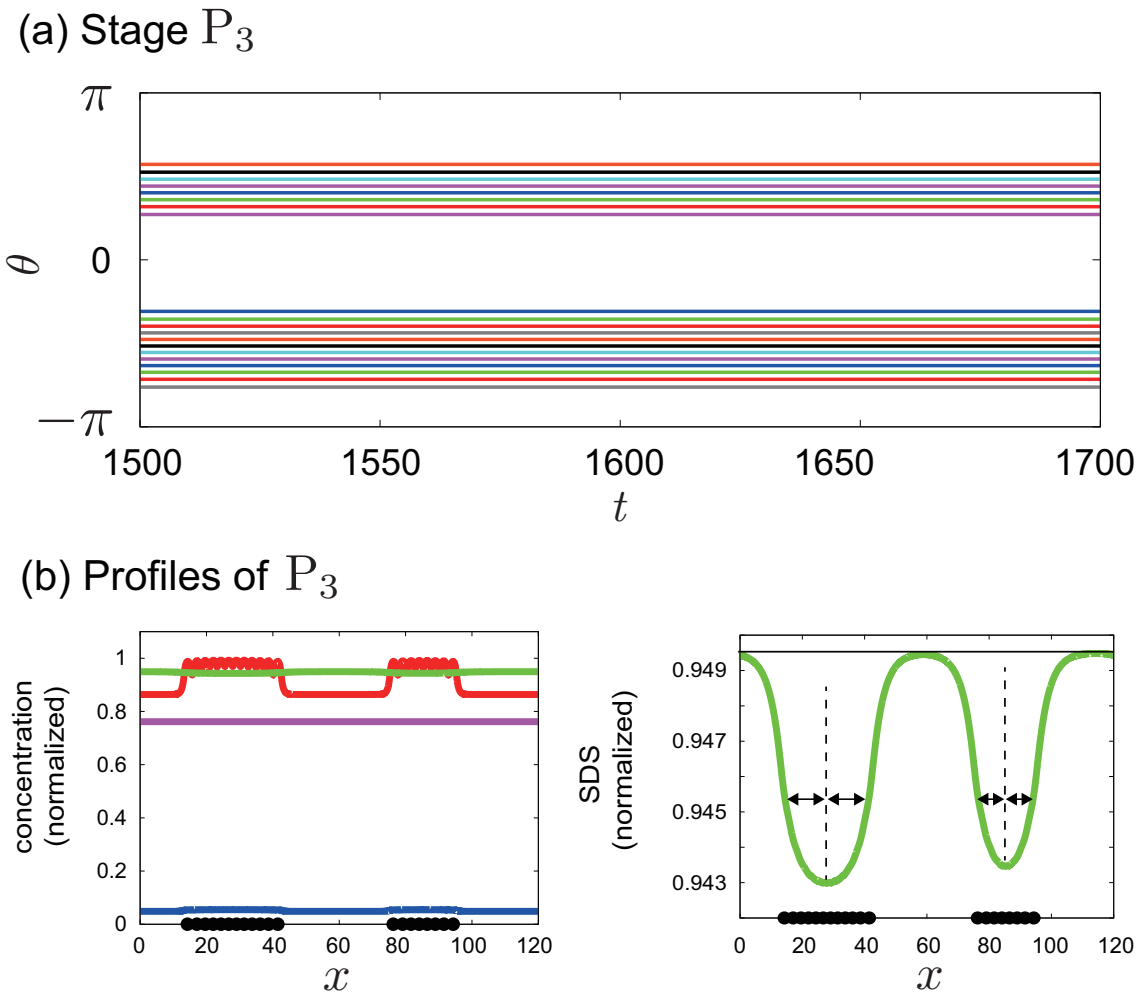

Figure 4.13: (a) The magnification for trajectories of the one cluster depicted as P_3. (b) Profiles of $\tilde{u}^*$, $\tilde{s}^*$, $\tilde{c}^*$, and $\tilde{w}^*$ for droplets during the clustering process P_3 in Fig. 4.10. The right side shows the magnification of the profile of $\tilde{s}^*/\tilde{s}_0^*$. The $\tilde{s}^*/\tilde{s}_0^*$ between the two clusters is almost equivalent.

the two relatively small clusters neared. In the spatial profile of SDS concentration, the larger two clusters are confined within the valley of the two-hump profile of $\tilde{s}^*$. Because the SDS concentration between the two clusters is nearly equivalent, no difference in the surface tension, two clusters keep the stationary state. Since SDS molecules are consumed due to the complex formation mostly near the droplet regions, the peak, τ_5, which is between two clusters, c_1, c_4, disappears when they are merged. However, an SDS concentration difference still exists between the two clusters but, the two clusters consistently maintain an exact distance since those of their outside keeps consistent. We confirm that the force induced by the surface tension difference causes the clustering, and, in particular, the clusters are merged faster as the SDS concentration difference

inside and outside of the clusters increases.

4.4.2.2 The effect of the cover on multiple droplets behavior

We also show the simulation results of twenty droplets for the one-dimensional model when the cover is removed after the droplets reach the stationary state in the clusters. As ever shown in Fig. 4.14, both ends droplets of each cluster widely expand, and the other droplets in the clusters start to oscillate little by little. After then, the both ends droplets of each cluster return to each cluster after a collision (P_4 in Fig. 4.14). The each droplet oscillates continuously in each cluster (P_5 in Fig. 4.14), and this result implies that the simulation result partially is consistent with the experimental result (Fig. 2.6).

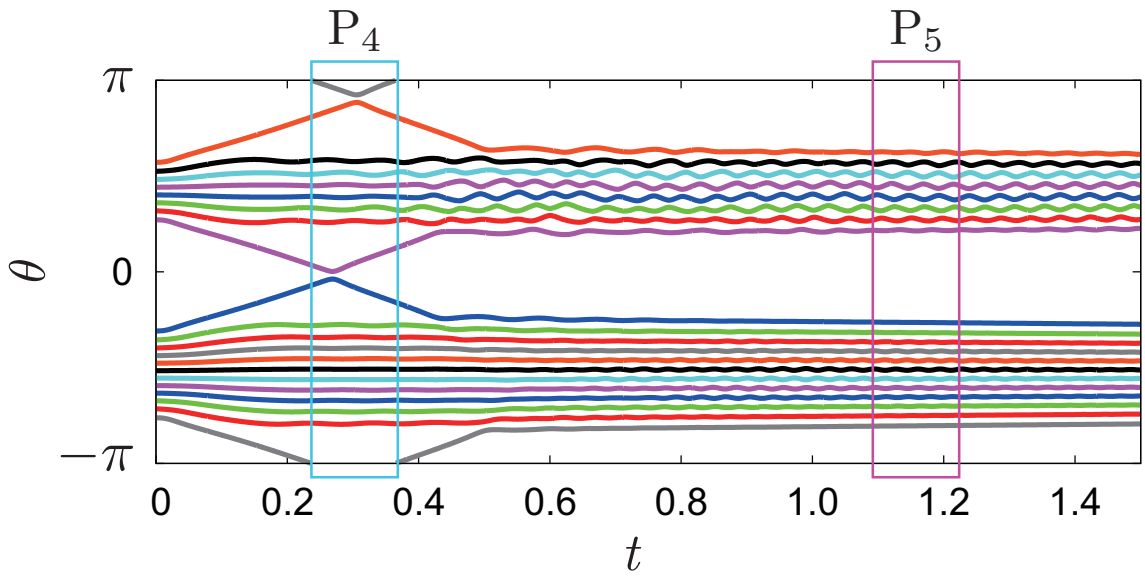

Figure 4.14: The trajectory of twenty droplets when the cover is removed applying the initial data as the last data of the case a removed cover (Fig. 4.10).

This behavior can be interpreted by the concentration profiles. In the same manner with a cover, the concentrations of $\tilde{u}^*$, $\tilde{s}^*$, $\tilde{c}^*$, and $\tilde{w}^*$ are used to inquiry into the mechanisms for P_4 and P_5.

Figure 4.15(a) shows a magnification of the trajectories that both ends droplets of the two clusters move faster than the inside droplets in the opposite direction in the beginning, and the direction of the droplets is changed as opposite after bumping into another droplet. Likewise, the results of a single droplet with a cover, the concentrations of both $\tilde{u}^*$, $\tilde{w}^*$ have converged zero, and the concentrations of $\tilde{c}^*$ is also decreased. In contrast, the SDS concentration slowly returns to $\tilde{s}_0^*$. For the same reason as the

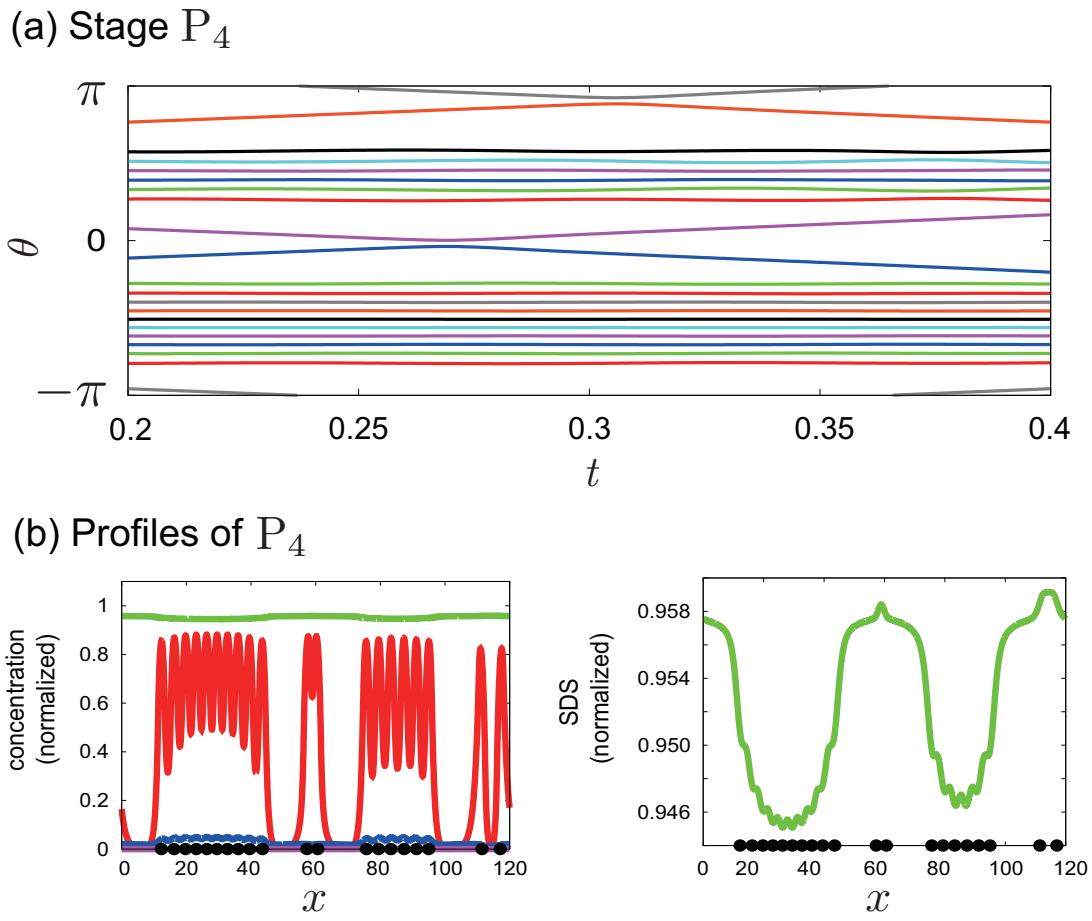

Figure 4.15: (a) The magnification for trajectories of the one cluster depicted as P_4 in Fig. 4.14. (b) Profiles of $\tilde{u}^*$, $\tilde{s}^*$, $\tilde{c}^*$, and $\tilde{w}^*$ for droplets during the clustering process in P_4. The right side shows the enlargement of the profile for $\tilde{s}^*/\tilde{s}_0^*$. The smooth shape of the SDS concentration on the two clusters is converted into the bumpy shape.

results of a two-dimensional model under a closed cover, the surface tension difference due to $\tilde{u}^*$ recovers, and the droplet motion resumes. In the separation of both ends of the cluster initiative, the spatial profile of SDS concentration well shows the process. Namely, the smooth shape of the profile for SDS concentration is slightly converted into a bumpy shape. Also, since the other peaks, which are higher than outside of bumping droplets, occur when the droplets bump, shown in Fig. 4.15(b).

Figure 4.16(a) shows an enlargement of the trajectories which are the oscillatory motion for droplets in the two clusters, shown in P_5 in Fig. 4.14. After returning to each cluster, both ends droplets of each cluster are not rebounded repeatedly and oscillate with the other inside droplets. In the spatial profile of SDS concentration, the distance between two clusters keeps without a break because of the peak between two

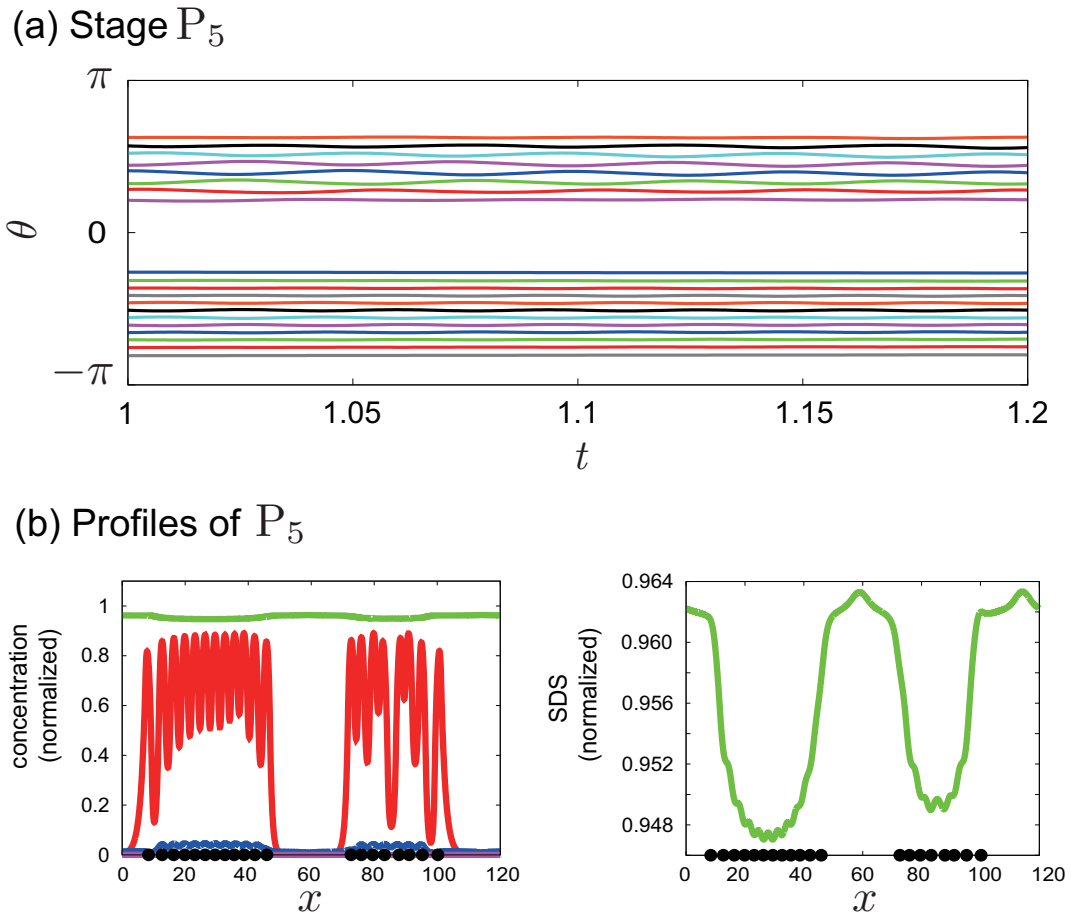

Figure 4.16: (a) The magnified trajectories of the oscillatory motion for the droplets depicted as P_5 in Fig. 4.14. (b) Profiles of $\tilde{u}^*$, $\tilde{s}^*$, $\tilde{c}^*$, and $\tilde{w}^*$ for droplets on during the clustering process in P_5. The right side shows the magnification of the profile for $\tilde{s}^*/\tilde{s}_0^*$. The certain distance between the clusters is maintained because of the peak of SDS concentration between two clusters.

clusters. The droplets placed inside the cluster are oscillated continuously, as shown in Fig. 4.16(b).

4.4.3 Comparison with experimental results

As in the case of the two-dimensional model we compares with the results of both the experiment and simulation. Since we already know the droplet diameter (2.5 mm) and the typical velocity (500 mm/h), we compare the timescale for a cluster formation in the simulation of the one-dimensional model. The droplet diameter is $2\tilde{r}^* = 2$ in the simulation. Therefore, 1 unit length in the simulation corresponds to 1.25 mm. In the simulation the typical velocity is estimated 40 unit length/unit time from Fig. 4.2.

The length is compared as $\tilde{L}_x^* = 16$ unit length $= 20$ mm, equating the two velocities from the experiment and the simulation yields 1 unit time $= 0.1$ h. Using this, we can estimate the timescale for the cluster formation. In the simulation, figure 4.10 shows that the cluster is formed approximately at $t = 1450$ unit time $= 145$ h. Note that the clustering of droplets depends on the system size $\tilde{L}_x^*$.

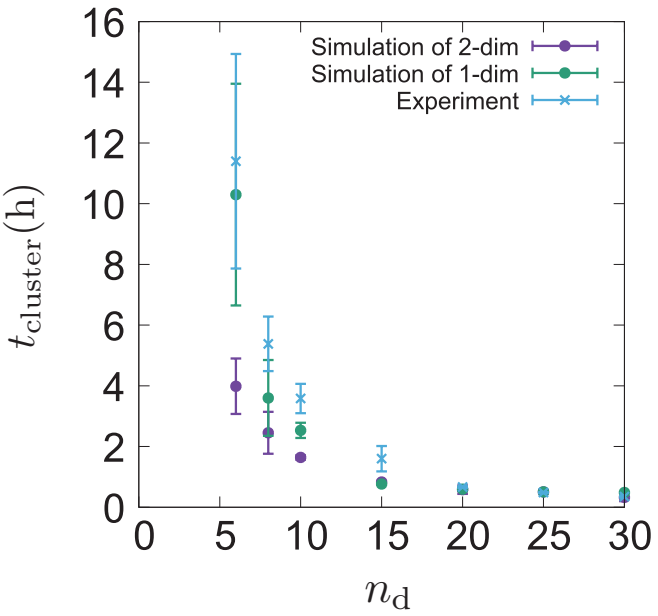

Figure 4.17: The first clustering time t_{cluster} as a function of the number of droplets n_{d} in simulations and experiment. For each n_{d}, Points are the average over three measurements. The error bars are the standard deviation. In the experiment and the one-dimensional model, no clusters were observed for $n_{\mathrm{d}} = 5$.

We also compared the first clustering time t_{cluster}, defined as the time to form a sub-cluster (mostly a two-droplet cluster) starting from an initial configuration for a given number of droplets n_{d}. We performed experiments for n_{d} =5, 6, 8, 10, 15, 20, 25, and 30. For each n_{d}, we repeated the experiment three times and measured the average and the standard deviation of t_{cluster}. Then we performed the corresponding numerical simulations for different n_{d} with three different initial random configurations of the droplets with $L_x = 200$, which is approximately equal to the experimental system size. The result is shown in Fig. 4.17. Likewise the two-dimensional model, the similar tendency that t_{cluster} is a decreasing function of n_{d} has been observed. Simulation of the one-dimensional model was more consistent with experimental results than the simulation of the two-dimensional model. In particular, for $n_{\mathrm{d}} = 5$, we observed cluster formation of the two-dimensional model, but as in the experiment, no cluster formation of the one-dimensional model has been produced.

5 Conclusion

This thesis has experimentally shown spontaneous oscillatory dynamics and clustering of ethyl salicylate (ES) droplets on the sodium dodecyl sulfate (SDS) surfactant solution in a narrow channel. To account for the experimental results, we have developed a two-dimensional mathematical model consisting of the chemical reaction based on the chemical properties, such as the formation of the complex of the ES and the SDS molecule, the low solubility of the ES molecules, the dissolution of the complex, as well as the experimental setup structure such as the depth of SDS surfactant solution. In particular, we considered the evaporation from on the air/water interface to in the air phase and the condensation from in the air phase to on the air/water interface according to the cover. Our intuition was that when the cover is closed, the ES concentration of the air/water interface increases as the ES concentration in the air phase decreases the evaporation of the ES molecules from the air/water interface. In contrast, when the cover is removed, the evaporation of the ES molecules from the air/water interface actively occurs because of the spread of the ES molecules out of the air in the air phase. Therefore, the effect of the cover has also been taken into account, which significantly affects the droplet dynamics. Based on the two-dimensional mathematical model, we have derived the one-dimensional mathematical model under the condition that the depth of SDS surfactant solution is sufficiently small. Our two mathematical models successfully reproduce oscillatory dynamics for the single droplet and clustering behaviors for the twenty droplets when the cover is closed and the recovery of their movement when the cover is removed. Furthermore, numerical simulations show that the concentration of ES than the concentration of SDS affects oscillatory dynamics, and the concentration of SDS than the concentration of ES affects clustering behaviors.

For oscillatory dynamics, through the computer-aided analysis, we have found that the surface tension generated from the ES concentration gradient acts in the opposite direction to the advancing direction of the droplet and reverses the droplet. It was also clearly revealed that the transition of oscillatory dynamics according to the cover occurs since the surface tension decreases because the ES concentration on the air/water interface is reached almost the saturation by the increase of the ES concentration in the air phase. That is to say, the ES concentration both on the surface and in the air phase played a significant role in the stationary state and oscillating motion of droplets.

For clustering behaviors, we have also found that the primary cause is the asymmetric distribution of SDS concentration on the air/water interface. Due to the occurrence of the surface tension difference at both ends of the droplets or the clusters under

the asymmetric distribution, the clustering of the droplets occurs. In contrast, the droplets or the clusters under the symmetric distribution no longer move because the difference in surface tension has disappeared. To put it another way, the global profile of the SDS concentration suffices for causing droplets and sub-clusters to approach each other, which is required for the formation of larger and larger clusters. Furthermore, we have made out that the cluster's velocity depends on the number of droplets contained in the cluster. The numerical simulation results show that the droplet approaches faster than the cluster when the droplet and the cluster are combined, and the small cluster moves faster than the large cluster when the small cluster and the large cluster are merged. To investigate clustering formation without attractive interactions between the droplets, we have reinterpreted the lateral capillary force by controlling the capillary length. Therefore, a critical implication of our result is that clustering can be explained without considering attracting interactions due to the lateral capillary force.

Finally, let us comment on the discrepancy between experiment and simulation. Our two mathematical models comprehensively coincided with the experimental fact for the single droplet dynamics and the twenty droplets clustering behaviors, but two parts partially needed the supplementation. First, in the numerical simulation of the single droplet, the two-dimensional model has yet to explain the experimental fact that droplets can oscillate for a long time before coming to the stationary state after the cover is closed one-dimensional model can precisely explain the experimental fact. Another is that in numerical simulation of the twenty droplets, the one-dimensional model clearly dose not show the experimental result that droplets can form the most significant cluster under a closed cover. However, the two-dimensional model is to explain the experimental result precisely . Therefore, additional work will be required to describe droplet dynamics more quantitatively.

6 Appendix

6.1 Surface tension $\gamma(u, s)$

We theoretically consider a decreasing function since the surface tension decreases as ES and SDS concentration increases, refer to assumption 4. Therefore, the surface tension, $\gamma(u, s)$, is defined depending on the ES concentration, as well as the SDS concentration as follows:

$$\gamma(u, s) = \frac{1}{2}\left(\frac{a^2}{a^2 + u^2} + \frac{b}{b + s}\right)(\gamma_0 - \gamma_1) + \gamma_1, \tag{6.1}$$

The a and b are a positive constant, and γ_0 and γ_1 are the maximum and minimum values of the surface tension. Furthermore, Fig. (6.1) can be separated with $g(u)$, $h(s)$. The surface tension monotonically decreases as u and s increases, and converges to zero when both u and s sufficiently high, as shown in Fig. 6.1.

$$\gamma(u, s) = g(u) + h(s) + \gamma_1,$$

$$g(u) = \frac{1}{2}\left(\frac{a^2}{a^2 + u^2}\right)(\gamma_0 - \gamma_1), \quad h(s) = \frac{1}{2}\left(\frac{b}{b + s}\right)(\gamma_0 - \gamma_1).$$

Figure 6.1 shows that both the $g(u)$ and $h(s)$ converge to zero as increasing u, s, that is, the surface tension, $\gamma(u, s)$ converges to γ_1. Therefore, γ_1 are the minimum value of the surface tension.

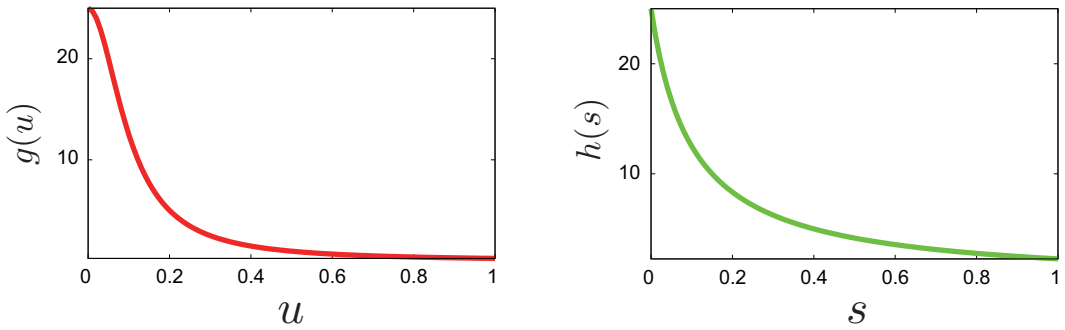

(a) Surface tension of ES concentration

(b) Surface tension of SDS concentration

Figure 6.1: (a) The surface tension depending on u, (b) The surface tension depending on s. $g(u)$, $h(s)$ converge to γ_1 as u and s increase.

6.2 Michaelis-Menten Type $f(s)$

The reaction velocity (V_{max}), defined as the mole concentration of the reactant consumed in unit time per unit volume, fast or slow depending on the type of chemical reaction. To consider the difference in the formation process of the complex in the vicinity of the droplet, we apply $f(s)$ function, which is called Michaelis-Menten type, as the dependence of the complex formation on the SDS concentration like as:

$$f(s) = \frac{\alpha s}{\beta + s},$$

where α and β mean the maximum velocity and the Michaelis constant, respectively.

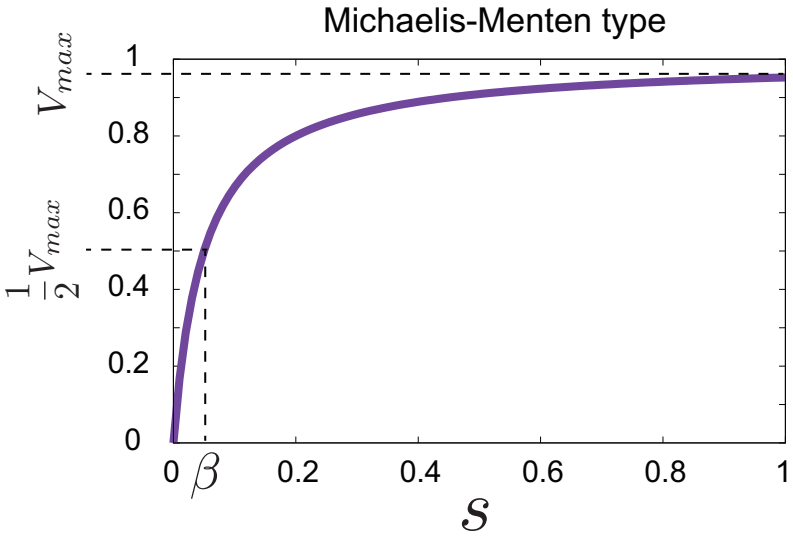

Figure 6.2: Michaelis-Menten type according to s. The parameters are $\alpha = 1.0$ and $\beta = 0.05$. When s equals to β, the reaction velocity reaches to half of maximum, and it is constant after sufficient increase of s.

Figure 6.2 means the reaction velocity of the Michaelis-Menten type according to s under the set parameters. When s is lower than β, the velocity proportionally increases, and it reaches $\frac{1}{2}V_{max}$ if s equals to β. Also, the reaction velocity is constant if s increases sufficiently. Based on these properties, to take into account the difference of the formation of the complex both the center and the around of droplet, we applied the Michaelis-Menten type to the formation of the complex. It means that the formation of the complex occurs faster in the vicinity than the center of the droplet.

References

[1] N. Abaid and M. Porfiri, *Collective behavior of fish shoals in one-dimensional annular domains*, in Proceedings of the 2010 American Control Conference, 63-68 (2010).

[2] M. Ballerini, N. Cabibbo,R. Candelier, A. Cavagna, E. Cisbani, I. Giardina et al. , *Interaction ruling animal collective behavior depends on topological rather than metric distance: evidence from a field study*, PNAS, 105, 1232-1237 (2008).

[3] S. Bazazi, K. S. Pfenning, N. O. Handegard and I. D. Couzin, *Vortex formation and foraging in polyphenic spadefoot toad tadpoles*, Behav. Ecol. Sociobiol. 66, 879-889 (2012).

[4] E. Bormashenko, Y. Bormashenko, R. Grynyov, H. Aharoni, G. Whyman and B. P. Binks, *Self-propulsion of liquid marbles: Leidenfrost-like levitation driven by marangoni flow*, J. Phys. Chem. C 119 (18), 9910-9915 (2015).

[5] J. Čejková, M. Novák, F. Štěpánek and M. M. Hanczyc, *Dynamics of Chemotactic Droplets in Salt Concentration Gradients*, Langmuir, 39 (4), 11937-11944 (2014).

[6] J. Čejková, T. Ikegami and F. Štěpánek, *Life-like swarm behavior of multiple chemotactic droplets*, in Proceedings of the 14th European conference in Artificial Life 2017, 14, 91-95 (2017).

[7] M. K. Chaudhury and G. M. Whitesides, *How to make water run uphill*, Science, 256, 1539 (1992).

[8] N. J. Cira, A. Benusiglio and M. Prakash, *Vapour-mediated sensing and motility in two-component droplets*, Nature, 519 (7544), 446-450 (2015) .

[9] S. Curiotto, F. Leroy, F. Cheynis and P. Müller, *Surface-dependent scenarios for dissolution-driven motion of growing droplets*, Sci. Rep. 7 (1), 1-11 (2017).

[10] A. Dussutour, M. Beekman, S. C. Nicolis and B. Meyer, *Noise improves collective decision-making by ants in dynamic environments*, Proc. R. Soc. B 276, 1677, 4353-4361 (2009).

[11] Y. Hayashima, M. Nagayama and S. Nakata, *A camphor oscillates while breaking symmetry*, J. Phys. Chem. B 105 (22), 5353-5357 (2001).

[12] E. Heisler, N. J. Suematsu, A. Awazu and H. Nishimori, *Swarming of self-propelled camphor boats*, Phys. Rev. E 85, 055201 (2012).

[13] Y. Hirose, Y. Yasugahira, M. Okamoto, Y. Koyano, H. Kitahata, M. Nagayama and Y. Sumino, *Two floating camphor particles interacting through the lateral capillary force*, J. Phys. Soc. Jpn. 89, 074004 (2020).

[14] Y. S. Ikura, E. Heisler, A. Awazu, H. Nishimori and S. Nakata, *Collective motion of symmetric camphor papers in an annular water channel*, Phys. Rev. E 88, 012911 (2013).

[15] P. Illien, C. de Blois, Y. Liu, M. N. van der Linden and O. Dauchot, *Speed-dispersion-induced alignment: A one-dimensional model inspired by swimming droplets experiments*, Phys. Rev. E 101 (4), 040602 (2020).

[16] Z. Izri, M. N. Van Der Linden, S. Michelin and O. Dauchot, *Self-propulsion of pure water droplets by spontaneous marangoni-stress-driven motion*, Phys. Rev. Lett. 113 (24), 248302 (2014) .

[17] H. -R. Jiang, N. Yoshinaga and M. Sano, *Active Motion of a Janus Particle by Self-Thermophoresis in a Defocused Laser Beam*, Phys. Rev. Lett. 105, 268302 (2010).

[18] H. S. Kim, K. Muller, O. Shardt, S. Afkhami and H. A. Stone, *Solutal Marangoni flows of miscible liquids drive transport without surface contamination* Nat. Phys. 13, 1105-1111 (2017).

[19] H. Kitahata, N. Yoshinaga, K. H. Nagai and Y. Sumino, *Spontaneous motion of a droplet coupled with a chemical wave*, Phys. Rev. E 84, 015101(R) (2011).

[20] M. I. Kohira, Y. Hayashima, M. Nagayama and S. Nagata *Synchronized self-motion of two camphor boats*, Langmuir, 17, 7124-7129 (2001).

[21] Y. Koyano, N. J. Suematsu, and H. Kitahata, *Rotational motion of a camphor disk in a circular region*, Phys. Rev. E 99, 022211 (2019).

[22] P. A. Kralchevsky and K. Nagayama, *capillary interactions between particles bound to interfaces, liquid films and biomembranes*, Adv. Colloid Interface Sci. 85, 145-192 (2000).

[23] P. A. Kralchevsky and N. D. Denkov, *Capillary forces and structuring in layers of colloid particles*, Curr. Opin. Colloid Interface Sci. 6, 383-401 (2001).

[24] I. Lagzi, S. Soh, P. J. Wesson, K. P. Browne and B. A. Grzybowski, *Maze solving by chemotactic droplets*, J. Am. Chem. Soc. 132, 1198-1199 (2010).

[25] S. W. Lee, D. Y. Kwok and P. E. Laibinis, *Chemical influences on adsorption-mediated self-propelled drop movement*, Phys. Rev. E 65, 051602 (2002).

[26] Y. Matsuda, N. J. Suematsu, H. Kitahata, Y. S. Ikura and S. Nakata, *Acceleration or deceleration of self-motion by the Marangoni effect*, Chem. Phys. lett. 654, 92-96 (2016).

[27] S. Michelin, E. Lauga and D. Bartolo, *Spontaneous autophoretic motion of isotropic particles*, Phys. Fluids 25 (6), 061701 (2013).

[28] A. S. Mikhailov and V. Calenbuhr, *From Cells to Societies*, (Springer, Berlin, 2002).

[29] K. Nagai, Y. Sumino, H. Kitahata and K. Yoshikawa, *Mode selection in the spontaneous motion of an alcohol droplet*, Phys. Rev. E 71, 065301(R) (2005).

[30] K. Nagai, K. Tachibana, Y. Tobe, M. Kazama, H. Kitahata, S. Omata and M. Nagayama, *Mathematical model for self-propelled droplets driven by interfacial tension*, J. Chem. Phys. 144, 114707 (2016).

[31] M. Nagayama, S. Nakata, Y. Doi and Y. Hayashima, *A theoretical and experimental study on the unidirectional motion of a camphor disk*, Physica D, 194, 151-165 (2004).

[32] S. Nakata, Y. Iguchi, S. Ose, M. Kuboyama,T. Ishii and K. Yoshikawa, *Self-Rotation of a Camphor Scraping on Water; New Insight into the Old Problem*, Langmuir, 13, 4454 (1997).

[33] S. Nakata and Y. Hayashima, *Spontaneous dancing of a camphor scraping*, J. Chem. Soc. Faraday Trans. 94, 3655-3658 (1998).

[34] S. Nakata, Y. Iguchi, S. Ose and T. Ishii, *pH-Sensitive Self-Motion of a Solid Scraping on an Aqueous Phase*, J. Phys. Chem. 102, 7425-7427 (1998).

[35] S. Nakata, T. Hayashima and H. Komoto, *Spontaneous switching of camphor motion between two chambers*, Phys. Chem. Chem. Phys 2, 2395-2399 (2000).

[36] K. Nishi, T. Ueda, M. Yoshii, Y. S. Ikura, H. Nishimori, S. Nakata and M. Nagayama, *Bifurcation phenomena of two self-propelled camphor disks on an annular field depending on system length*, Phys. Rev. E 92, 022910 (2015).

[37] H. Nishimori, N. J. Suematsu and S. Nakata, Collective behavior of camphor floats migrating on the water surface, J. Phys. Soc. Jpn. 86, 101012 (2017).

[38] A. Ordemann, G. Balazsi and F. Moss, *Pattern formation and stochastic motion of the zooplankton Daphnia in a light field*, Physica A, 325, 260-266 (2003).

[39] L. -A. Poissonnier, S. Motsch, J. Gautrais, J. Buhl, A. Dussutour, *Experimental investigation of ant traffic under crowded conditions*, eLife 8 (2019) e48945.

[40] M. Poujade, E. Grasland-Mongrain, A.. Hertzog, J. Jouanneau, P. Chavrier and B. Ladoux et al, *Collective migration of an epithelial monolayer in response to a model wound*, Proc. Natl. Acad. Sci. 104, 15988-15993 (2007).

[41] V. Pradines, R. Tadmouri, D. Lavabre, J.-C. Micheau and V. Pimienta, *Association, partition, and surface activity in biphasic systems displaying relaxation oscillations*, Langmuir, 23, 11664-11672 (2007).

[42] S. Ramaswamy, *The Mechanics and Statistics of Active Matter*, Annual. Rev. Condensed Matter Phys. 1, 323-346 (2010).

[43] Y. Satoh, Y. Sogabe, K. Kayahara, S. Tanaka, M. Nagayama and S. Nakata, *Self-inverted reciprocation of an oil droplet on a surfactant solution*, Soft Matter, 13, 3422-3430 (2017).

[44] J. A. Shapiro, *Thinking about bacterial population as multicellular organisms*, Annu. Rev. Microbiol. 52, 81-104 (1998).

[45] J. Sharma, I. Tiwari, D. Das, P. Parmananda and V. Pimienta, *Rotational synchronization of camphor ribbons in different geometries*, Phys. Rev. E 101, 052202 (2020).

[46] S. Soh, K. J. M. Bishop and B. A. Grzybowski *Dynamic self-assembly in ensembles of camphor boats*, J. Phys. Chem. B 112 (35), 10848-10853 (2008).

[47] S. Soh, M. Branicki and B. A. Grzybowski, *Swarming in shallow waters*, J. Phys. Chem. Lett. 2, 770-774 (2011).

[48] Y. Sumino, N. Magome, T. Hamada and K. Yoshikawa, *Self-Running Droplet: Emergence of Regular Motion from Nonequilibrium Noise*, Phys. Rev. Lett. 94, 068301 (2005).

[49] Y. Sumino, H. Kitahata, H. Seto, S. Nakata and K. Yoshikawa, *Spontaneous deformation of an oil droplet Induced by the cooperative transport of cationic and anionic surfactants through the interface*, J. Phys. Chem. B 113, 48, 15709-15714 (2009).

[50] S. Tanaka, Y. Sogabe and S. Nakata, *Spontaneous change in trajectory patterns of a self-propelled oil droplet at the air-surfactant solution interface*, Phys. Rev. E 91, 032406 (2015).

[51] S. Tanaka, S. Nakata and T. Kano, *Dynamic ordering in a swarm of floating droplets driven by solutal Marangoni effect*, J. Phys. Soc. Jpn. 86, 101004 (2017).

[52] S. Tanaka, S. Nakata and M. Nagayama, *A surfactant reaction model for the reciprocating motion of a self-propelled droplet*, Soft Matter, 17, 388-396 (2021).

[53] U. Thiele, K. John and M. Bar, *Dynamical model for chemically driven running droplets*, Phys. Rev. Lett. 93, 027802 (2004).

[54] T. Toyota, N. Maru, M. M. Hanczyc, T. Ikegami and T. Sugawara, *Self-propelled oil droplets consuming "fuel" surfactant*, J. Am. Chem. Soc. 131, 5012-5013 (2009).

[55] V. Vandadi, S. J. Kang and H. Masoud, *Reverse marangoni surfing*, J. Fluid Mechanics, 811, 612-621 (2017) .

[56] O. V. Velev, B. G. Prevo and K. H. Bhatt, *On-chip manipulation of free droplets*, Nature, 426, 515-516 (2003) .

[57] T. Vicsek, A. Czirok, E. Ben-Jacob, I. Cohen and O. Shochet, *Novel type of phase transition in a system of self-driven particles*, Phys. Rev. Lett. 75, 1226-1229 (1995).

[58] T. Vicsek and A. Zafeiris, *Collective motion*, Phys. Rep. 517, 71-140 (2012).

[59] F. Wodlei, J. Sebilleau, J. Magnaudet and V. Pimienta, *Marangoni-driven flower-like patterning of an evaporating drop spreading on a liquid substrate*, Nat. Commun. 9 (1), 1-12 (2018).

[60] L. Zhang, J. J. Abbott, L. Dong, B. E. Kratochvil, D. Bell and B. J. Nelson, *Artificial bacterial flagella: Fabrication and magnetic control*, Appl. Phys. Lett. 94, 064107 (2009).

[61] H. P. Zhang, A. Be'er, E.-L. Florin and H. L. Swinney, *Collective motion and density fluctuations in bacterial colonies*, PNAS, 107, 13626-13630 (2010).

[62] G. Zhao and M. Pumera, *Marangoni self-propelled capsules in a maze: pollutants 'sense and act' in complex channel environments*, Lab on a Chip, 14, 2818-2823 (2014).